

AD \_\_\_\_\_

Award Number: **W81XWH-11-1-0129**

**TITLE: In Vivo Clotting Breast Cancer Stem Cells and Platelets: A New Endogenous Precursor of Metastasis Progression.**

**PRINCIPAL INVESTIGATOR: Ekaterina Galanzha**

**CONTRACTING ORGANIZATION: University of Arkansas**

**Little Rock AR 72205-7101**

**REPORT DATE: April 2013**

**TYPE OF REPORT: Final**

**PREPARED FOR: U.S. Army Medical Research and Materiel Command  
Fort Detrick, Maryland 21702-5012**

**DISTRIBUTION STATEMENT: Approved for Public Release;  
Distribution Unlimited**

The views, opinions and/or findings contained in this report are those of the author(s) and should not be construed as an official Department of the Army position, policy or decision unless so designated by other documentation.

# REPORT DOCUMENTATION PAGE

*Form Approved  
OMB No. 0704-0188*

Public reporting burden for this collection of information is estimated to average 1 hour per response, including the time for reviewing instructions, searching existing data sources, gathering and maintaining the data needed, and completing and reviewing this collection of information. Send comments regarding this burden estimate or any other aspect of this collection of information, including suggestions for reducing this burden to Department of Defense, Washington Headquarters Services, Directorate for Information Operations and Reports (0704-0188), 1215 Jefferson Davis Highway, Suite 1204, Arlington, VA 22202-4302. Respondents should be aware that notwithstanding any other provision of law, no person shall be subject to any penalty for failing to comply with a collection of information if it does not display a currently valid OMB control number. **PLEASE DO NOT RETURN YOUR FORM TO THE ABOVE ADDRESS.**

1. REPORT DATE A UMr2013			2. REPORT TYPE Final		3. DATES COVERED 1 May 2011 - 30 April 2013	
4. TITLE AND SUBTITLE  In Vivo Clotting Breast Cancer Stem Cells and Platelets: A New Endogenous Precursor of Metastasis Progression.			5a. CONTRACT NUMBER W81XWH-11-1-0129			
			5b. GRANT NUMBER W81XWH-11-1-0129			
			5c. PROGRAM ELEMENT NUMBER			
6. AUTHOR(S) Dr. Ekaterina I. Galanzha  E-Mail: EGalanzha@uams.edu			5d. PROJECT NUMBER			
			5e. TASK NUMBER			
			5f. WORK UNIT NUMBER			
7. PERFORMING ORGANIZATION NAME(S) AND ADDRESS(ES)  University of Arkansas Little Rock, Arkansas 72205-7101			8. PERFORMING ORGANIZATION REPORT NUMBER			
9. SPONSORING / MONITORING AGENCY NAME(S) AND ADDRESS(ES) U.S. Army Medical Research and Materiel Command Fort Detrick, Maryland 21702-5012			10. SPONSOR/MONITOR'S ACRONYM(S)			
			11. SPONSOR/MONITOR'S REPORT NUMBER(S)			
12. DISTRIBUTION / AVAILABILITY STATEMENT Approved for Public Release; Distribution Unlimited						
13. SUPPLEMENTARY NOTES						
14. ABSTRACT Most cancer-related deaths arise from metastasis produced by circulating tumor cells (CTCs). A new concept of this research is that circulating cancer stem cell (CSC)-platelet aggregates (CSCPA) represent the most aggressive subset of CTCs responsible for breast cancer metastasis. <u>The goal</u> of this proposal is to identify and count CSCPAs <i>in vivo</i> in preclinical models of metastatic breast cancer, and to define the correlation of CSCPA amount with metastasis development. We developed a novel, <i>in vivo</i> multicolor photoacoustic (PA) flow cytometry (PAFC) platform for the detection of CSCPAs using the principle of flow cytometry, negative and positive PA contrasts, multispectral high-pulse-repetition-rate lasers, bioconjugated nanoparticles and a mouse model of human breast cancer. Using this approach, we provided a proof-of-concept for highly sensitive detection of CSCPAs and individual CSCs in real biological environments in a whole body <i>in vivo</i> . For the first time, we demonstrated the ability of CSCs to form aggregates with platelets (CSCPAs) in blood circulation of tumor-bearing mice. Furthermore we showed that the number of CSCPAs increased during development of metastatic disease. Obtained preclinical results can advance general understanding of cancer stem cell biology and metastasis progression as well as will be used as the basis for initiating highly innovative clinical research in cancer patients.						
15. SUBJECT TERMS Circulating aggregates of cancer stem cells and platelets, <i>in vivo</i> multicolor flow cytometry, nanoparticles, molecular targeting						
16. SECURITY CLASSIFICATION OF:			17. LIMITATION OF ABSTRACT UU	18. NUMBER OF PAGES 64	19a. NAME OF RESPONSIBLE PERSON USAMRMC	
a. REPORT U	b. ABSTRACT U	c. THIS PAGE U			19b. TELEPHONE NUMBER (include area code)	

**THE TITLE:** In Vivo Clotting Breast Cancer Stem Cells and Platelets: A New Endogenous Precursor of Metastasis Progression.

## TABLE OF CONTENTS

	<u>Page</u>
<b>Introduction.....</b>	<b>2</b>
<b>Body.....</b>	<b>2</b>
<b>Key Research Accomplishments.....</b>	<b>12</b>
<b>Reportable Outcomes.....</b>	<b>13</b>
<b>Conclusion.....</b>	<b>14</b>
<b>References.....</b>	<b>15</b>
<b>Figures.....</b>	<b>16</b>
<b>Appendices.....</b>	<b>27</b>

## INTRODUCTION

Controlling metastatic disease is one of the challenges in cancer research because most cancer deaths arise from metastases. Despite many improvements in diagnosis of metastasis through assessment of CTCs in blood samples, the treatment of metastasis based on current diagnosis is still notoriously poorly effective. Therefore, great efforts should be undertaken in developing earlier, more sensitive markers of metastasis, making well-timed therapy more effective. Experimental and clinical observations established that only rare CTCs produce metastasis. Although the putative candidate for metastasis-initiating cells is cancer stem cells (CSCs), the suggested proportion of CSCs (up to 35% for breast cancer) are higher than the percentage of cells resulting in metastasis (< 0.1%). Many CSCs are most likely killed under strong mechanical and immunological stresses of blood flow while the survival of others may be related to CSC-platelet aggregates (CSCPAs) that protect tumor cells and promote their extravasation in tissues. Thus, CSCPAs are potential crucial target for breast cancer diagnosis and therapy. However, CSCPAs have never been studied before due to technical limitations. The major obstacle of *in vitro/ex vivo* methods is limited volume of blood sample, and therefore, low sensitivity to identify very rare CSCs among a small population of CTCs disseminated in a large background of different blood cells in flow. A significant increase in the tested blood volume could be achieved by an *in vivo* approach. *In vivo* study may also exclude possible alterations of cells during extraction from their natural environment and manipulations under *in vitro* conditions. Among various *in vivo* diagnostic techniques (e.g., MRI, PET, CT and optical assays), *in vivo* flow cytometry (photoacoustic, photothermal and fluorescent) provides detection of fast moving single cells and their aggregates.<sup>1-3</sup> Furthermore, photoacoustic (PA) flow cytometry (PAFC) is a clinically relevant method based on the conversion of absorbed energy in acoustic waves in low-toxic nanoparticles (NPs) which provides higher sensitivity and resolution in deeper tissue (up to 5-7 cm) compared to most optical modalities.<sup>1</sup> However, *in vivo* PA detection of CSCPAs has not yet been proposed.

The goal of this proposal is to identify and count CSCPAs *in vivo* in preclinical models of metastatic breast cancer, and to define the correlation of CSCPA amount with metastasis development. The main hypothesis is that some breast CSCs interact with platelets, forming CSCPAs, and their quantity is positively correlates with metastasis development.

To achieve this goal, we pursued the following Objectives/Tasks: (1) Define the optimal parameters of nanotechnology-based multi-color PAFC for detection of CSCPAs in blood vessels using *in vitro* phantom of blood circulation; (2) *In vivo* study using xenograft orthotopic mouse model of breast cancer.

## BODY

### **Task 1: Define the optimal parameters of nanotechnology-based four-color PAFC for detection of CSCPAs in blood vessels using *in vitro* phantom of blood circulation**

To resolve our working hypothesis we used the technical platform of *in vivo* FC. Using support from this grant, the support from other sources, as well as the additional equipment available in our laboratories, we developed *in vivo* detection of CSCPAs using the principle of negative (i.e., a signal from targeted cell/aggregate is below blood background) and positive PA contrasts (i.e., a signal from targeted cell/aggregate is above blood background), time-resolved PA spectroscopy, multispectral high-pulse-repetition-rate lasers, nanoparticles (NPs) as PA high-contrast low-toxic agents, multiplex molecular targeting, PA spectral analysis, a mouse model of human breast cancer, and integration of PA, PT and fluorescent methods. Specifically, laser irradiation of blood vessels in normal vessels creates a constant PA background determined by the absorption of RBCs randomly distributed in the irradiated volume. Depending on the size of the vessels, hematocrit (Ht), and PAFC spatial resolution, the number of RBCs in the detected volume can vary from one or a few RBCs in the capillary to thousands in larger vessels. When a clot with high-absorbing NPs (absorption of NPs at the appropriate wavelength >> absorption of blood) passes through the irradiated blood volume, a transient increase in the local absorption from NPs results in a sharp positive PA peak. When a weakly-absorbing, platelet rich white clot passes through the laser-irradiated vessel volume, a transient decrease in the local absorption results in a sharp

negative PA signal. A clot with NP-labeled cells (e.g., CSCs) and platelets (i.e., low-absorbing) local zones will produce a pattern of positive and negative PA signals. This platform (**Fig. 1**) includes a multi-channel, inverted microscope, Olympus IX81 (Olympus America, Inc.), with an automated precise (positioning accuracy, 50 nm) scanning 3-D translation stage (H117 ProScan II, Prior Scientific, Inc., USA), a spectrally tunable optical parametric oscillator (OPO: 420–2300 nm, 1 mJ, 5 nsec, and 100 Hz; Opotek Inc.). The setup was equipped with four high-pulse-repetition-rate nanosecond lasers with the following parameters: 1) wavelength, 532 nm; maximum pulse energy, 116 µJ; pulse width, 5.3 ns; and repetitions rate, up to 100 kHz (model: LUCE 532, Bright Solutions, Cura Carpignano, Italy); 2) 671 nm, 36 µJ, 25 ns, and 20 kHz (model: QL671-500, CrystaLaser, Reno, NV); 3) 820, 76 µJ, 8 ns, and 30 kHz (model: LUCE 820, Bright Solutions); and 4) 1,064 nm, 80 µJ, 10 ns, and 750 kHz (model: MOPA-M-10, Multiwave Photonics, Porto, Portugal). The integration of *in vivo* PAFC with fluorescent flow cytometry (FFC) termed as PAFFC was also available for completion of this research.<sup>3</sup> PAFFC used both pulsed and continuous wave (CW) lasers (e.g., 488 nm, 50 mW, IQ1C45(488-60) G26, Power Tech., Alexander, AR and 532 nm; 7 mW, GLC-007-L, CrystaLaser LC, Reno, NV) as traditional sources for the generation of PA and fluorescent signals, respectively. For example, we incorporated a CW diode laser 488 nm, 45 mW to ensure detection of bulk CTCs with green fluorescent protein (GFP). Laser beams were shaped using cylindrical lenses ( $f = 250$  mm) to be focused across the blood vessel with focal spot dimensions of  $5 \times 80$  µm. All the laser beams were propagating in parallel with the main axis of the microscope. Laser beams were focused into different parts of the blood vessels by lateral displacement of the beams from the main axis of the microscope. Laser beams did not fill full NA of the objective, so 50 µm lateral beam waist displacement in the object plane of the microscope was possible without beam shape distortion.

In the selected study we used a PT microscope (PTM) that is available in our laboratory for estimation of labeling efficacy of cells by conjugated NPs: the labeled cells reveals significant increase in PT signal amplitude compared to control cells with no NPs. The PTM was built on the technical platform of an inverted Olympus IX81 microscope-spectrometer with a tunable OPO (420-2500 nm) with PT thermal lens module.

PA signals were detected by an ultrasound transducer (unfocused: model V323-SM, 2.25 MHz, or focused: model V316-SM, 20 MHz, both from Panametrics-NDT, Olympus) oriented towards the detection zone and coupled with ultrasound gel. PA signals were then amplified (model 5662, 5 MHz, 54 dB; or model 5678, 40 MHz, 60 dB, both from Panametrics-NDT, Olympus). Laser energies, were adjusted by sets of natural density filters and controlled by photodetectors and an energy meter (PE10-SH, Ophir Optronics, Jerusalem, Israel).

Laser beams were navigated on selected blood vessels with an X-Y motorized stage with a controller (STG4400ML, Conix Research, Inc., Springfield, OR) under imaging guidance with high-resolution (~300 nm) optical microscopy. Light emitting diode with 630 nm wavelength (M625L3 Thorlabs Inc, Newton, NJ) was used as a light source for CCD camera. The microscope was equipped with two CCD and one CMOS cameras: 1) a high resolution, color, cooled DP42, Olympus; 2) color PC135C-4G (Supercircuits, Inc., USA) used for the navigation of laser beams; and 3) a high speed CMOS camera, model MV-D1024-160-CL8, Photonfocus, Switzerland.

The schematic of advanced integrated setup is presented in **Figure 1**. However, during the testing of this technical platform with multicolor beads and, then, with labeled cells we were faced with interference (overlapping) of signals.

To overcome this technical challenge we developed novel signal acquisition algorithm.

### Signal acquisition

Data acquisition was performed by two high speed digitizers installed in separate workstations (Precision T7500, Dell, Round Rock, TX). PA signals were acquired by custom AD484 (14-bit, 125 mega-samples per second, 4DSP Inc., Reno, NV). FL signals from the PMTs were acquired by GaGe CS1442 (14-bit, 200 mega-samples per second, DynamicSignals, Lockport, IL). Pulsed lasers and digitizers were triggered and synchronized by a digital delay/pulse generator (DG645, Stanford Research Systems, Sunnyvale, CA).

*In vivo* FC (e.g., PAFC) produces a signal trace representing amplitudes of the corresponding signals as function of time. The appearance of an object of interest in the detection volume is usually represented by a transient change in amplitude in signal, i.e. appearance of a narrow peak in the trace. The width of this peak is determined by the time it takes a CTC or CSCPA to cross laser beam. Both increase and decrease of the signal can be considered as a peak revealing either positive or negative contrast of the circulating object compared to the blood background. Both, PAFC and FFC produce similar signal traces. However the PAFC has specific features. In PAFC the sample is irradiated only during a very short laser pulse. Absorption of light generates acoustic waves that reach the detector after a few  $\mu$ s delay. The PA waves are detected using ultrasound transducer that converts energy of acoustic oscillations into an electrical signal. Frequency spectrum of ultrasound waves requires fast analog-to-digital converter (ADC) sampling rates of over 100 MHz. For each laser pulse, ADC samples transducer voltage and analyzes the record to measure the amplitude of the acoustic oscillation. In the case of PA cytometry, pulse repetition rate (PRR) of the laser determines the time resolution of PA trace, not the sampling rate.

PA phenomenon in the sample generates a pressure wave having a bipolar shape that is transformed into a pulse train of a certain frequency by the resonant piezo-crystal in ultrasound transducer. Hence, to improve the detection sensitivity we selected frequency analysis for each PA wave to reveal presence of oscillations in a certain small frequency band. These oscillations were directly correlated with the intensity of PA signal. This data acquisition scheme allowed us a significant reduction in the data amount right after data acquisition before applying any averaging to the waveforms. Thus, a continuous recording of raw data was possible for all the triggered events for later reprocessing and selection of the optimal parameters (averaging, spectral region). This also made it possible to avoid the loss of temporal details.

Details of the data acquisition and signal-processing procedures are presented in **Figure 2**. PA signals were collected through one transducer and then digitized by ADC. The digitizer performs Fast Fourier Transform (FFT) on each triggered event, using its custom field-programmable gate array (FPGA) firmware. A user can define several parameters for this operation: sampling frequency, ( $f_s$ ; 80 or 120 MHz), FFT length (1,024 or 512 points), wait time before acquisition after a trigger (0–10  $\mu$ s), and the frequency region of interest (fROI) (1–1,024 points) to be returned to the host program for further real-time and post-processing routines. The digitizer was controlled with software custom-written in C++ for fast acquisition and recording of the raw spectral data. All other real-time and post-processing operations were implemented in MATLAB (MathWorks, Natick, MA).

The delay between a laser pulse and the resulting PA signal depends on the distance between the laser focal point and the transducer. Setting a wait time for acquisition is essentially a time-resolved gating that allows accurate selection of PA signals and removal of any noise between the trigger and the start of the PA signal, such as the electromagnetic noise originating from the laser hardware.

Fourier coefficients in the specified frequency band (fROI) were calculated from the gated time signals. Selection of fROI plays two roles in this scheme: 1) data compression (~50 $\times$ ) by discarding of the irrelevant frequency components and 2) SNR improvement by focusing on the most significant frequencies discriminating PA signals from noise.

In multicolor PAFC, PA signals were generated by several pulsed lasers having different wavelengths. To separate these events a time delay was used between laser pulses, so each one arrived independently (**Fig. 3**). Thus, subsequently fired four pulsed lasers created four PA signals, which were acquired by the same transducer. To reliably correlate acquired PA signal with the laser wavelength, we used a “laser flag” parameter for each trigger event. The laser flag was extracted from the second channel on the digitizer, which was essentially the trigger signal for one of the four lasers. For each trigger event (i.e., laser pulse), complex Fourier coefficients were combined with the laser flag and a trigger counter, constituting a frame. The frames were then returned to the workstation and saved to hard-disk drive. For the typical settings of  $f_s = 80$  MHz, FFT length = 1,024 points, fROI = 1.6–3.28 MHz (20<sup>th</sup> to 41<sup>st</sup> coefficients), and  $4 \times PRR = 40$  kHz, the data rate was 440 MB/min.

During post-processing, the series of frames were separated into virtual channels and associated with their laser sources. Within each channel, coherent spectral averaging was applied to N frames in order to reduce variance and increase SNR by a factor of  $\sqrt{N}$ . N consecutive frames can be selected with 50% or no overlapping. As a result, the number of frames was reduced by a factor of  $N/2$  or  $N$ , respectively. At this point, two types of PAFC traces were created: 1) by calculating the total spectral power in each frame (PA spectral power trace) and 2) by taking the inverse FFT of each frame and finding the maximum peak-to-peak voltage in the reconstructed time-domain signal (PA amplitude trace). Hence, each triggered event was translated into a number and traced similarly to conventional fluorescence cytometry, in which each point in the trace represents the direct reading of fluorescence intensity. Peaks in this trace correspond to PA events (**Fig. 4**).

The digitizer and software can sustain recording up to a 75-kHz and a 150-kHz PRR for 1,024- and 512-point FFT, respectively. The performance of the software depends on the selected parameters. For a typical case with four lasers operating at  $4 \times \text{PRR} = 40$  kHz, the software is capable to display all the traces in real-time after averaging  $\geq 10$  frames. However, since the digitizer records the raw data for all the trigger events, PA traces with different averaging parameters may be recalculated in post-processing. FFC signals were collected from four different PMTs which are connected to four different channels in the digitizer. FFC signals were continuously sampled at 100 kHz rate and then downsampled to 10 kHz rate with an average of 10 points. Each FFC wavelength is assigned a separate acquisition channel. Since PAFC and FFC signals were recorded via separate hardware stations and software, there is an inevitable time offset between these traces. In order to accurately measure this offset, all laser beams (pulsed and CW) are blocked at the same time for a few seconds, at least once for each measurement. This results in dips with sharp edges in the background signals of both PAFC and FFC traces. The offset is measured as the time difference between the appearances of an edge in two different types of traces.

The data were then combined and analyzed in post-processing. PA signals are collected through one transducer, i.e., one channel on the digitizer. Although the lasers are synchronized by periodic triggering, the synchronization may easily be lost if the digitizer fails to record one of the events. This risk is averted by supplying the second channel of the digitizer by the signal that triggers 1064 nm laser. The firmware samples this channel only once per each trigger. Ideal signal in this channel constitutes a repeating [0 0 0 1] pattern. If any trigger is missed and this pattern is corrupted, neighboring triggers are dropped until the next ideal pattern is found. Trigger counter is not affected by this compensation of missed triggers. PA traces are then plotted against time which is extracted from trigger counter. Any discarded trigger would result in a gap in the trace.

Recorded traces were analyzed in post-processing to identify events and perform statistical analysis of the data. Any object entering or leaving the detection volume transiently changes amplitude of the signal, i.e., appears as a narrow peak in FC traces. It is a challenge to detect these peaks in a noisy trace. This is especially true for in vivo experiments, where the background signals are relatively strong (autofluorescence, etc.) and fluctuating (physiological effects, etc.).

Our custom-developed peak analyzer performed the following steps for peak detection in each trace:

- High-pass filtering ( $f_c=10$  Hz) was applied to eliminate any changes in background level.
- The filtered trace was then split into short segments. In each segment;
  - Average value ( $m$ ) and standard deviation ( $s$ ) were calculated.
  - Peak threshold,  $th = m + c \times s$ , was determined; where  $c$  is a coefficient determined as the largest value that does not produce any false positive signals in control experiments.
  - All peaks that were above the threshold were found.
  - Edges of the peaks were determined as the zero-crossing points closest to the peak. At this step, a peak was a part of the trace that consists of at least three points.
  - Any overlapping peaks were aggregated and represented as a single peak.
- The measured time offset between channels was applied to corresponding peak parameters.

Final stage of the data post-processing included the analysis of signal coincidence across all the channels of the setup to reveal all the signals originating from the same object in circulation.

Various artifacts were expected to be present in multi-channel data. First, the amplitudes of the PA signals reflect the absorption spectra, assuming the fluence is equal for all the lasers. Even the fine-tuned GNRs (used in this research) have spectral overlap resulting in appearance of low amplitude signals in the neighboring channels. A secondary artifact is caused by the reflection of strong PA waves in the sample. Although PA channels are all separated in time, it is still possible that one sound wave created in channel A is reflected from the transducer or sample walls, and as an echo it may appear in channel B, C, etc. In this case, the original signal is always the largest, and the following tails gets smaller as the time delay increases (in the order of  $\mu$ s). Such echo effects (acoustic tail) may significantly hinder distinguishing and/or separation of the real PA signals from the artifacts in PAFC. To avoid it, we implemented a two component strategy: spatial and temporal separation of the laser beams. First, if laser beams are spatially separated and only one laser beam hits the object any echo artifacts in other channels should be ignored or corrected for. Second, for longer intervals between laser pulses echo amplitude is dramatically reduced. Thus, we provide spatial and temporal separation in the following manner: lasers 1 and 3 are focused into the same spot, while lasers 2 and 4 are focused  $\sim 40 \mu\text{m}$  down the blood flow. Given the order of laser firing from 1 to 4, it minimizes acoustic tail effect and allows detection of multiple independent events occurring at the same time (e.g., matching 532 and 820 peaks, but no tail in 671 or 1064). Genuine signals appear with time delays (in the order of ms) relating to the distance between laser beams. This information can be used to directly extract cell velocity information as the distance between laser beams is known. In FFC cytometry, spectral overlap is a well-known problem. Fluorescent markers have rather wide emission spectra which cause appearance of FFC signals of different amplitude across multiple channels. Thus, for all labels excited by laser, all the signals would appear at the same time, and their amplitude would be proportional to the extent of the spectral overlap. Here, we also implemented a spatial separation strategy, when 480 and 532 nm laser sources are separated in space. However, it is not universally applicable, as many labels (for example multicolor quantum-dots) should be excited using only one laser.

In order to account for cross-channel spectral overlap between labels, we measured ratio between peak amplitudes as it is done in conventional FC. In *in vivo* research the analysis accuracy is slightly decreased compared to *in vitro* FC, as very small overlap may be lost in the background fluctuations of the blood flow. Thus, we also use multiple control injections of cells with a single type of the label. In this case a ratio of concurrent peak amplitudes may be recorded under *in vivo* experiment conditions providing valuable information for post-processing analysis. Subtraction of a certain multiple of largest peak from the smaller matching peaks provides spectral overlap correction. If the resulting trace still has a significant peak after this subtraction, it is considered as a sign of dual labeling event (presence of a different marker).

After acquisition, FC traces were analyzed to identify individual events and to separate events from channels to reveal coincidence between these events and, thus, identify CSCPAs, CSCs and bulk CTCs.

Task 1a. Determine the most reliable molecular markers for labeling breast cancer stem cells.

According to data from literature, the most promising candidate profiles for specific labeling of breast cancer stem cells are CD44+/CD24 $^+$ , EpCam+/CD44+/CD24 $^+$  and EpCam+/CD24 $^+$ . Using conventional FC (available as core facility), the cells with these putative stem-molecular profiles were sorted from bulk breast cancer cells (MDA-MB-231 cell line). In the scope of another proposal we determined that the using of MDA-MB-231 cells expressing GFP and luciferase (MDA-MB-231-luc2-GFP) is more promising for dynamic *in vivo* studies of metastatic disease than the use of cells non-expressing GFP and luciferase (original MDA-MB-231 cells) because GFP can provide (1) high-quality fluorescent imaging cancer cells in blood, and (2) detection of 99.8% of bulk CTCs in blood circulation by FFC. Luciferase can be used as a well-known advanced marker to identify metastasis in a whole-body imaging. Conventional flow cytometry of the original MDA-MB-231 cells (ATCC) and MDA-MB-231-luc2-GFP Bioware® Ultra Green cell line (Caliper) did not reveal significant differences in the molecular profiles related to stem cells. For example, when both cell lines were analyzed by conventional FC for CD44, they showed 94% and 91% CD44+ cells, respectively ( $p>0.1$ ). Therefore, we used MDA-MB-

231-luc2-GFP cells in our research.

First, the stem features of MDA-MB-231 breast cancer cells were estimated with well established spheroid-forming assay. To determine the capacity of breast cancer cells to form spheroids in the absence of attachment using super-low adherence 96-well plates (Corning, Lowell, MA), three aliquots of cells were tested and sorted by conventional flow cytometry into two groups: sorted for CD44+/CD24-, EpCam+/CD44+/CD24- and EpCam+/CD24- cells and unsorted cells. Every three days the spheres were counted and pictures were taken (**Fig. 5a**). As expected, over 2 to 3 weeks, the frequency of a spheroid formation was 25%, 17% and 15% for CD44+/CD24-, EpCam+/CD44+/CD24- and EpCam+/CD24- cells, respectively. The ability to form spheroids in all three unsorted cell populations was much lower (0-1%).

Although all three profiles demonstrated tumorigenic potential, CD44+/CD24- cells were not appropriate for the particular cell line almost all MDA-MB-231 cells exhibited expression of CD44 (**Fig.5b**). Conventional FC demonstrated  $93\pm3\%$  CD44+/CD24- cells within bulk MDA-MB-231 cell line while the percentage EpCam+/CD24- cells ( $7.5\pm2.2\%$ ) looked like more realistic to characterize stem cells (**Fig.5c**). Thus, we selected EpCam+/CD24- profile for *in vivo* detection of CSCs in blood circulation of tumor-bearing mice.

**Task 1b.** Conjugate the gold nanorods (GNRs) with maximum absorption near 650-670 nm, 820 and 1024 nm (Nanopartz, Inc.) with antibodies (Abs) specific to markers of breast cancer stem cells (EpCAM and CD24) and activated platelets (P-selectin [CD62P]).

The GNRs with different maximum absorptions (e.g., GNR670, GNR820, and GNR1064) and required bioconjugations were produced by a commercial company (Nanopartz, Inc.). To increase the number of simultaneously detected markers, we also used integrated PAFFC. This integrated approach allowed us to use quantum dots (QDs; Ocean NanoTech, LLC, Springdale, AR) and genetically encoding fluorescent proteins (GFP) as contrast agents for FFC. The low toxicity of PEGylated GNRs was guaranteed by the company.

**Multifunctional contrast agents.** *In vivo* FC can use a wide range of contrast agents including intrinsic chromophores (e.g., melanin and hemoglobin), genetically encoded fluorescent proteins (e.g., green fluorescent protein [GFP]), and bioconjugated fluorescent dyes, quantum dots (QDs) or absorbing NPs (e.g., GNRs). This allows choosing the contrast agent set suitable for a particular biological task. For example, the detection of bulk CTCs can be achieved by genetic labeling (e.g., GFP) while CSCs and CSCPAs can be recognized by their specific molecular profiles after labeling with bioconjugated contrast agents (e.g., NPs). Among various contrast agents, the use of gold-based NPs (e.g., GNRs) is most promising for clinical use due to their low toxicity. Gold has been used in humans for over 50 years (e.g., dental prosthetics, implants, treatment of arthritis), and, recently, gold NPs were approved for pilot cancer-related clinical studies. To the best of our knowledge, we were the first to suggest using gold NPs with a pulse laser for single-cancer-cell diagnosis and therapy in 2000 (U.S. Patent #7230708; priority date December 28, 2000). In particular, in the framework of a DOD award in 2002–2003 (DAMD17-03-01-0579: “Nano-Photothermalysis of Breast Tumor”), we demonstrated PT therapy of breast cancer cells, as well as leukemic cells, targeted by functionalized gold NPs. Thus, we intended to apply integrated FC with multifunctional contrast agents to bridge gaps in our knowledge of CSCPAs and their responsibility for metastasis progression with focus on breast cancer.

**Task 1c and 1d.** (1c) Estimate targeting efficacy of breast cancer stem cells (CSCs) and platelets from donor mice with bioconjugated GNRs and explore the capability of nanoparticles (NPs) as contrast agents for *in vivo* flow cytometry. (1d) Optimize the concentration of NPs to provide clear PA signals from GNRs bound with targeted cells.

Human breast cancer cells (MDA-MB-231, American Type Culture Collection [ATCC] and MDA-MB-231-luc2-GFP Bioware® Ultra Green cell line, Caliper) were cultured according to the vendor’s specifications. Viable cells were resuspended in phosphate buffered saline (PBS) or in a sample of mouse blood. The cell samples were labeled with bioconjugated GNRs (e.g., GNR670 bioconjugated with Abs to EpCam [EpCam-

GNR670]; GNR 1064 with Abs to CD24 [CD24-GNR1064]) at different concentrations separately and in combination (30 min, 37°C, double washing). The GNRs with different maximum absorptions (e.g., GNR670 with maximum absorption at 670 nm and GNR1064 at maximum absorption at 1060 nm) were provided by a commercial company (Nanopartz, Inc.). The low toxicity of PEGylated GNRs was guaranteed by the company.

Labeling specificity was provided through bioconjugation of GNR670 with molecular markers (e.g., EpCam) against the surface receptors (e.g., EpCam and folic receptors) which are highly expressed in breast cancer cells, but almost absent in normal blood cells (mainly, leukocytes). In selected experiments we also used quantum dots (quantum dots with maximum emission at 620 nm [QD620]) that allowed us to increase the number of colors and specificity of detection (e.g., to distinguish CTCs from leukocytes that may non-specifically uptake GNRs). After double washing of each aliquot, cells were placed in a well (120 μm thickness) for testing. The labeling efficiency was assessed with PT and PA cytometry, conventional *in vitro* flow cytometry and fluorescent microscopy (by use specific tags) (**Fig. 6**). Specifically, PT microscopy was used because PA and PT methods are very similar in basic physical processes, and supplement each other in applications with a sensitivity advantage of PT techniques (up to 10–50-fold) *in vitro* at a sub-cellular level, while PA methods allow detection of individual cells *in vivo* in deep tissue.<sup>1,2</sup>

We compared different laser energies in PA and PT cytometry to adjust the parameters providing the absence of signals from cells alone (control sample). Notably, for both, PA and PT, detection of labeled breast cancer cells we used laser energies that were several times below the detection threshold for label-free breast cancer cells. We obtained that GNRs attached to cancer cells (the optical and PT imaging verified this attachment<sup>2</sup>) provided a 10–50-fold higher PT signal amplitude than the unbound GNRs. It can be explained by nanoparticle clustering around naturally densely packed cell markers leading to nonlinear signal amplification due to more effective laser-induced formation of a nanobubble (as a signal amplifier) around overheated nanoparticle clusters with enhanced local absorption.<sup>1</sup> These phenomena may serve as indicators of successful molecular targeting of cells. The non-specific binding was estimated as a percentage of PA and PT signals from cells incubated with non-conjugated NPs.

We also explored the dependence of labeling efficiency from nanoparticle concentration.<sup>2</sup> Breast cancer cells were labeled by GNR670-Folate (>95% MDA-MB-231 cells expressed Folate) expressed at the concentrations ranging from 500 to 50,000 nanoparticles per a cell. Surprisingly, even 500 GNR670-Folate per a cell was enough for effective PT detection of 30-40 % cells. At the ~5,000 NPs per a cell, the most cells (~92%) provided PT signals. The obtained results represented a good agreement with data from conventional flow cytometry (90-95% for folate). Increasing the number of GNRs to ~50,000 per a cell at even, decreasing laser energy led to a non-significant increased percentage of detected Folate+ cells to 97.5%. However, we observed simultaneously, false signals from the surrounding solution due to the likely presence of not perfectly washed NPs. Thus, the concentration of ~5,000 GNRs per cell was selected as the optimal for labeling breast cancer cells, and was used in experiments *in vivo*.

**Tasks 1e and 1f.** (1e) Evaluate the optimal diameter of vessels to provide ensure negative signal from CSCPAs in blood at 532 nm (near strong absorption band of blood) and prevent false-positive negative contrast from single cancer cells. (1f) Explore the capability of PAFC to detect circulating breast CSCs and CSCPAs *in vitro* using blood samples from donor mice spiking with breast cancer cells.

First, to verify target specificity *in vitro*, mouse blood samples were spiked with a controlled number of cancer cells (~1% of RBC numbers) and treated with unconjugated and conjugated NPs either alone or in various combinations. The incubation time was 30 minutes at 37°C. Fluorescent imaging was used for the navigation of the laser beam on a cancer cell. Expression of GFP by the bulk cancer cells was used for navigation of the laser beam by fluorescent microscopy (**Fig. 7a**). The conventional FC of the same blood samples was used for verification of PT and PA results. For example, PA and PT scanning cytometry and conventional FC demonstrated the similar percentage of EpCam+ cancer cells in blood samples: 53±7% of green cells provided high amplitude signals associated with EpCam+ cancer cells by PT and PA cytometry; and 61% of EpCam+

cancer cells were found by conventional FC.

Our results also indicated the possibility of non-specific uptake of GNRs by leukocytes (white blood cells [WBCs]) due to their well-known phagocytic activity. Therefore, to increase accuracy of CSC detection in blood and minimize false signals we added GNR bioconjugated with Abs to CD45 which is a common marker of WBCs typically used to distinguish CTCs (CD45-) from WBCs (CD45+).

For *in vitro* modeling of blood circulation, mouse blood was spiked with breast cancer cells. A flow module based on a syringe pump–driven system (KD Scientific, Inc.) with an adjustable flow speed (0–10 cm/sec) was used with glass tubes of different diameters. Testing glass tubes with different diameters similar to those of mouse ear blood vessels demonstrated the optimal diameter of vessels to provide ensure negative signal from low-absorbing aggregates (e.g., CSCPAs) in blood at 532 nm was ranged from 30 to 50- $\mu$ m.<sup>4</sup>

To estimate the ability of our technical platform to detect moving cells, cocktail of various bioconjugated labels (e.g., GNRs) was added in the system for labeling tumor cells and platelets. The small sample (~3-5  $\mu$ L) was withdrawn from circulating blood at different times (e.g., 5, 10, 20 and 30 minutes) after adding labels. The samples were placed on a slide for *ex vivo* analysis of labeling efficacy by PA and PT scanning cytometry and fluorescent microscopy. The velocity of cells was measured by frame-by-frame video-recording and by PAFC in time-of flight mode<sup>1</sup> as we recently developed. The effective labeling (e.g., >90% cancer cells after adding GNRs conjugated with folate) was observed in 5 minutes under flow condition at a velocity of 1-5 cm/s and in 10 min at a velocity of 0.2-1 mm/s. As expected, the targeting >90% CTCs in the same sample under static condition was achieved in 30 minutes (**Fig. 7b**).

Our modeling of blood circulation *in vitro* also revealed a quick (5±1.5 min) formation of platelet and cancer cell aggregates varying in size (**Fig. 8**). Unexpectedly, 20–30% of clots contained markers associated with the CSCs.

### **Task 2. In vivo study using xenograft orthotopic mouse model of breast cancer**

The *in vivo* study included: (1) calibration of *in vivo* PAFFC on healthy mice (control group); (2) labeling CSCs and platelets *in vitro* followed by their intravenous injection in the mice circulation; (3) labeling injected cells *in vivo* through a second intravenous injection of GNRs; (4) targeting real CSCPAs using well-established xenograft orthotopic model of breast cancer in nude mice.

At different stages of cancer development, CSCPAs, circulating CSCs and bulk CTCs were noninvasively tested by FC *in vivo*. At the end of *in vivo* measurements, mice were sacrificed to estimate metastasis by conventional assays (e.g., histology, flow cytometry).

**Control measurements on healthy mice.** Calibration of the FC signals from ear blood vessels of mice without any interventions (e.g., injections or inoculations) and after adding conjugated NPs with optimized parameters revealed no signals above blood background. With CW lasers (at 488-nm and 540-nm, 1-2 mW) variations of background autofluorescence from blood from sample to sample were not significant for vessels of the same diameter. A signal-amplitude threshold in each channel was determined as the mean and an increment of the standard deviation (typically 5 SDs) of the background signal. Signals having a higher amplitude than this threshold were associated with CTCs.

**Task 2a and 2b.** (2a) Label CSCs and platelets *in vitro* and inject them in tail vein of the mice followed by PAFC's detection of CSCPAs and single CSCs in mouse circulation. (2b) Label prior injected cells *in vivo* through a second intravenous injection of GNRs followed by PAFC's detection of single CSCs in mouse circulation.

We used both, *in vitro* and *in vivo* labeling. Specifically, MDA-MB-231-luc2-GFP breast cancer cells (~1×10<sup>5</sup> cells per injection) labeled *in vitro* with the EpCam GNR671and CD24-GNR1064, platelets from donor mice

labeled by CD62P-QD and the WBCs from donor mice labeled with the CD45-GNR820 (incubation time - 30 min at 37°C), were injected into the mouse circulation. Multicolor FC was used for monitoring clearance rates of mimic CTCs, platelets and WBCs. Both FC modules, PAFC and FFC, detected CTCs with a signal-to-background-noise ratio (SNR) ranging from 2 to 30. Negative contrast PAFC at the wavelength of 532 was used to detect low absorbing aggregates. Because the number of labeled, injected cells was controlled, the efficacy of *in vivo* PAFC was estimated by comparison of the rate of dynamic PA signals at the appropriate wavelength. For example, high amplitude dynamic signals at 671-nm-PA channel combined with absence of PA signals at 1024-nm-PA channel and 820-nm-PA channel were associated with individual EpCam+/CD24-/CD45- CSCs; high amplitude dynamic signals at orange-FFC channel combined with the absence of PA signals at all PA channels were associated with individual CD62P+ platelets while high amplitude dynamic signals at 671-nm-PA channel and at orange-FFC channel combined with negative dynamic signal at 532-nm-PA channel and with absence of PA signals at 1024-nm-PA channel and 820-nm-PA channel were associated with circulating CSCPAs. **Figure 9** showed typical patterns of PA signals: 1) with negative contrast at 532 nm associated with platelet-rich clots only (pattern I); 2) simultaneously with negative contrast at 532 nm and positive contrast at 671 nm, which indicates on CSCPAs (pattern II) in agreement with *in vitro* data; and 3) with positive contrast at 671 nm associated with CSCs only (pattern III).

This experiment was also used to estimate FC's sensitivity. Although the maximal number of CTCs per a minute varied from mouse to mouse because of individual injection conditions and distribution of cells in the body, we could detect an average of up to 9 CTCs/min in vessels with a mean diameter of  $52 \pm 5 \mu\text{m}$ . This was close to the theoretical estimation of up to 12 CTCs/min in a 50-μm-diameter vessel at a velocity of 2 mm/s after the introduction of  $1 \times 10^5$  cells.

In a second set of experiments, we determined whether CSCs and platelets are selectively labeled *in vivo* with the same NPs. In particular, we injected cancer cells ( $10^5/\text{mL}$ , 50 μL) into the mice. After that, the “cocktail” of NPs were administered in the circulation to label the EpCam+/CD24-/CD45- CSCs and CD62P+ platelets. The algorithm of the experiments was the same as the previous set of tests. PA signals obtained from intact vessels before cell injection served as a control background. The readable transient PA signals were observed with different patterns of negative, positive, and combined contrasts associated with CSCPAs, circulating single CSCs, bulk CTCs and aggregates of bulk CTCs and platelets, respectively, compared to no signals in normal control mice.

The labeling *in vivo* took ~5–12 min which demonstrated good agreement with our *in vitro* results (see above). High labeling efficiency was associated with frequent NP–CTC collisions in partly turbulent blood flow. In accordance with our modeling, injection of  $10^{10}$  NPs into the mouse's blood circulation with a volume of ~2 mL provided, on average,  $\sim 10^3$  NP–CTC collisions per min with expected differences in the velocities of NPs and CTCs 61 mm/s, while their absolute velocities may be 5–10 mm/s. This allowed the capture of antibodies by cell surface markers, and the capturing efficiency did not decrease at relative differences in the velocities of NPs and cells at 61–1.5 mm/s and the shear stress 60.5 dyn/cm<sup>2</sup>. The PA signals from targeted cells with a typical NP number, ranging from 500–5000 NPs per CTC was much higher than the PA background from RBCs, unbound NPs with typical numbers of 1–10 in the detected volume, or from NPs nonspecifically bound to normal blood cells (e.g., macrophages). NP clustering around naturally densely packed cancer markers led to significant enhancement in PA signals (at least 5–10-fold), and a red-shift effect in the absorption of coupled NPs in clusters, both of which served as indicators of successful cell targeting. We optimized the amount of injected NPs which range from  $10^9$ – $10^{10}$  NPs per mouse. These NPs did not produce notable signals immediately after injection, but a latter gradual increase in the PA signal amplitude and rate indicated a successful labeling process. Occasionally, strong PA signals would be observed immediately after intravenous injection of NPs over the period of few minutes. This was associated with NP aggregates which then are quickly (typically within few minutes) cleared from the circulation. To minimize this effect, before the injection, NP clusters were disaggregated by ultrasound and then filtered. Nevertheless, if short lasting signals from NP alone occurred immediately after injection, these signals were differentiated from signals related to cell targeting *in vivo* because the latter appeared typically after a time delay.<sup>1</sup>

Tasks 2c, 2d and 2e: (2c) Inoculate breast cancer cells in a mammary fat pad of mice to establish primary tumor. Tumor formation will be assessment by conventional methods at least once a week. (2d) Examine mice by PAFC at early and late stages of tumor development to detect and count CSCPAs and single CSCs. (2e) Estimate correlation between rate of CSCPAs and metastasis development.

The next step was *in vivo* study of CTCs, which shed from the primary tumor and naturally aggregate with platelets in blood circulation to form CSCPAs. We used the xenograft orthotopic mouse model of breast cancer. To establish primary tumors, MDA-MB-231-luc2-GFP breast cancer cells were inoculated into a mouse mammary pad. Mice with inoculated tumor were divided into two groups: one group was examined with PAFFC at two weeks, the second group was investigated by PAFFC at eight weeks after tumor inoculation. To permit ensure labeling of CSCs and platelets, all mice were injected by cocktail of molecular labels (e.g.,  $\sim 10^{11}$  NPs of each type per a mouse) 15-20 minutes before PAFFC. The intravital monitoring of the primary tumor and metastasis progression were conducted weekly with a well-established Xenogen IVIS system providing whole-body imaging. At the end of weeks 2 and 8, mice were euthanized. The samples of blood and tissues (e.g., brain, liver, lymph nodes, and lungs) were extracted for ex vivo transmission and fluorescent (a 530/30 nm filter for GFP) optical imaging with different magnifications (objective lenses of  $\times 10$ ,  $\times 20$ ,  $\times 40$  and  $\times 100$ ). To verify metastatic disease, multiple organs were also used for histological examination with hematoxylin and eosin (H&E) staining.

The analysis of the original FC traces demonstrated that the developed approach is able to successfully detect EpCam+/CD24 CSCs, CD62P+ platelets and their aggregates (CSCPAs) in tumor-bearing mice through temporal coincidence of CSC-related peaks and platelet-related peaks. Obtained data supports the hypothesis of platelets aggregating around CTCs. Simultaneously, we distinguished bulk CTCs as GFP+ cells and aggregates of bulk CTCs with platelets as GFP+/CD62P+. For example, **Figure 10** illustrates the detection of the bulk CTC (GFP+ on **Fig. 10a**), CSCPAs (EpCam+/CD24-/CD62P+ on **Fig. 10b**) and circulating CSC (EpCam+/CD24-/CD62P- on **Fig. 10c**) in the mouse with advanced metastatic disease.

Then using new FC's signal acquisition algorithm we quantified the obtained results. In the majority ( $>90\%$ ) of mice, the signals associated with bulk CTCs were appeared on FC's traces starting from week 1 of tumor development. The early appearance of CTCs can be related to the model of parallel progression of primary tumor and metastasis. As demonstrated **Figure 11**, the highest CTC rate was revealed at the stage of actively growing metastases (8 wks after tumor inoculation). In both week 2 and week 8 after tumor inoculation, the bulk CTCs contained the significant proportion CSCs (20-60%), which increased with the tumor development (**Fig. 11a**). Furthermore, both, bulk CTCs and CSCs, formed aggregates with platelets. However the dynamic and proportion of these aggregates changes during disease progress. In week 2, PAFFC detected rare CSCPAs; only  $\sim 2\%$  of circulating CSCs aggregated with platelets. However, in week 8, more than 7% CSCs formed CSCPAs that led to a 6.7-fold increase of their rate in circulating blood ( $p < 0.02$ , **Fig. 11b**). Notably, the rate of bulk CTCs and CSCs revealed only 1.9-fold and 4.1-fold increase (**Fig. 11a**). Unexpectedly, we found that the number FC's signals associated with aggregates of platelets and bulk CTCs was reduced in almost 3 times from week 2 to week 8.

The progress of metastatic disease was confirmed by imaging that, as expected, demonstrated the earliest metastasis in the sentinel lymph node (SLN; the first metastatic site). Then metastatic disease involved lungs and bones. As demonstrated histological and microscopic results, in week 2 after tumor inoculation, the metastatic lesions affected 60% mice, mainly, in SLNs. Some mice ( $\sim 30\%$ ) exhibited also micrometastases in lungs. In week 8, the metastatic disease was progressed, which was characterized by development of distant metastases (e.g., lungs, bones) in 88.9% of tumor-bearing mice.

The number of CSCPAs did not correlate with size of primary tumor but correlate with development of metastatic disease.

Despite very interesting and promising results, our detailed analysis demonstrated that not all mice exhibited strong correlation between amount of CSCPAs and progress of metastasis. To clarify this issue, the future

studies should be focused on using (1) various molecular profiles characterizing aggressive CTCs (e.g., CTCs expressed mesenchymal markers as result of epithelial-mesenchymal transition [EMT]); or/and (2) more point of observation during progress of metastatic diseases.

Furthermore the assessment of individualized dynamic of CSCPAs, CTCs and CSCs revealed the biological challenge related to the high heterogeneity of all circulating events from mouse to mouse. To understand the significance of this heterogeneity, the extended studies with increased number of mice per group are needed.

Task 2d. Prepare the final report.

The final report was prepared.

## KEY RESEARCH ACCOMPLISHMENTS

We developed a novel approach for detection aggregates of breast cancer stem cells and platelets (CSCPAs) in circulating blood *in vivo* using the principle of flow cytometry with multispectral high-pulse-repetition-rate lasers and bioconjugated NPs as high-contrast molecular contrast agents. For the first time, the functionalized NPs (e.g., GNRs) were proposed to use for advanced *in vivo* molecular detection of CSCPAs. *In vitro* and *in vivo* verifications allowed us to estimate significant targeting efficacy of cells of interest with these contrast agents. We established optimal laser and NP's parameters as well as preferable range of vessel's diameters for detection of individual cells and their aggregates labeled by bioconjugated NPs against a background of blood using positive and negative contrasts. The advanced NPs such as GNRs demonstrated good bioconjugation capability with different Abs and were able to selectively target cells (aggregates) of interest (e.g., EpCam+/CD24- CSCs) in blood. Our tests showed that the EpCam+/CD24- phenotype is the most relevant to breast MDA-MB-231 CSCs. As a result, we developed the protocol for *in vitro/ex vivo* (e.g., ~5,000 GNRs per a cell, 30-min incubation at 37°C) and *in vivo* (e.g., ~10<sup>11</sup> GNRs per a mouse injected 5-12 minutes before using of PAFFC) molecular detection and counting of circulating breast CSCPAs and CSCs in blood with bioconjugated NPs.

We demonstrated the *in vivo* feasibility of our approach (1) to provide simultaneous real-time counting EpCam+/CD24- CSCs, CD62P activated platelets and their aggregates (CSCPAs) in breast cancer bearing mice and (2) to estimate relationships of CSCPAs with progress of metastatic diseases. Obtained *in vivo* results were verified *in vitro* with a multifunctional PT microscopy-cytometry integrated with fluorescent and transmission modules as well as with well-established methods including conventional flow cytometry and histology.

In general, this study provided a proof-of-concept for highly sensitive PA detection of circulating CSCPAs and individual CSCs in real biological environments in a whole body *in vivo*.

For extended year we overcame the technical challenge related to the signal acquisition. Using new algorithm, we identified and counted CSCs traveling separately or together with platelets (CSCPAs) through temporal coincidence of CSC-related and platelet-related peaks. The advance of this acquisition is simultaneous real-time quantitative detection of CSCPAs, circulating CSCs, bulk CTCs and aggregates of platelets with bulk CTCs in their natural vascular environment *in vivo* during progress of metastatic disease. As a result, we performed advanced re-estimation of all FC's original data received from tumor-bearing mice. This allowed us to quantify the number of CSCPAs in dynamic of breast cancer development and evaluate relationships of CSCPAs and single circulating CSCs as well as bulk CTCs. We discovered that CSCPAs represented a relatively small proportion of circulating CSCs (e.g., ~2% at early stage of tumor development without overt metastasis) which was significantly increased (6.7 times in average) in disease progression.

Since May 2012, we have also published three manuscripts. Furthermore, two invited, one hot topic invited, two oral and two poster presentations have been resulted from this research during extended period. One manuscript directly related this project is currently under preparation for high-level journal (Nature Medicine).

In general, the obtained quantitative interrelationships between CSCPAs, circulating CSCs, bulk CTCs and

aggregates of platelets with bulk CTCs and metastases (micrometastases) will help to delineate new steps in the metastatic cascade. We established, for the first time, that CTCs with CSC molecular profile are able to form aggregates with platelets in blood circulation of breast-cancer-bearing mice *in vivo*, and the number of CSCPAs positively correlated with disease development.

In future, testing CSCPAs might be used to improve patient outcome as an ultra-sensitive prognostic marker of early metastasis progression/recurrence, therapy efficacy, and as candidate of targeted therapy. Taking into account the safety of the PA technology, our method may potentially be feasible in humans.

## REPORTABLE OUTCOME

- Seven manuscripts
- Twelve oral and poster presentations on the national and international workshop and conferences including the hot topic talk, invited talk and invited lecture.

### Published peer-reviewed papers:

1. Galanzha EI, Sarimollaoglu M, Nedosekin DA, Keyrouz SG, Mehta JL, Zharov VP. In vivo flow cytometry of circulating clots using negative photothermal and photoacoustic contrasts. *Cytometry A*. 2011 Oct;79(10):814-24. (this original manuscript introduced the principle of photoacoustic dynamic negative contrast in biomedical research)
2. Galanzha EI, Zharov VP. Photoacoustic flow cytometry. *Methods*. 2012;57(3):280-96.
3. Kim JW, Galanzha EI, Zaharoff DA, Griffin RJ, Zharov VP. Nanotheranostics of circulating tumor cells, infections and other pathological features *in vivo*. *Mol Pharm*. 2013;10:813-30.
4. Nedosekin DA, Sarimollaoglu M, Galanzha EI, Sawant R, Torchilin VP, Verkhusha VV, Ma J, Frank MH, Biris AS, Zharov VP. Synergy of photoacoustic and fluorescence flow cytometry of circulating cells with negative and positive contrasts. *J Biophotonics*. 2013;6:425-34.
5. Mazen A. Juratli, Mustafa Sarimollaoglu, Eric Siegel, Dmitry A. Nedosekin, Ekaterina Galanzha, James Y. Suen, Vladimir P. Zharov. Real-time monitoring of circulating tumor-cell release during tumor manipulation using *in vivo* photoacoustic and fluorescent flow cytometry. *Head and Neck*. (in press).
6. Nedosekin DA, Juratli MA, Sarimollaoglu M, Moore CL, Rusch NJ, Smeltzer MS, Zharov VP, Galanzha EI. Photoacoustic and photothermal detection of circulating tumor cells, bacteria and nanoparticles in cerebrospinal fluid *in vivo* and *ex vivo*. *J Biophotonics*. 2013;6:523-33.

### Proceedings of the conference:

1. Mazen A. Juratli M.D., Ekaterina I. Galanzha, Mustafa Sarimollaoglu, Dmitry A. Nedosekin, James Y. Suen M.D., Vladimir P. Zharov. Photoacoustic monitoring of clot formation during surgery and tumor surgery. SPIE Proc.: Photons Plus Ultrasound: Imaging and Sensing 8581, 2013.

### Oral and poster presentations on the national and international workshop and conferences including the Hot topic talk, invited talk and invited lecture:

1. Galanzha EI (Invited lecture), Negative contrast photoacoustic and photothermal imaging, spectroscopy and cytometry; International school of quantum electronics on “Photoacoustic and Photothermal Phenomena. Focus on Biomedical and Nanoscale Imaging and NDE”, *Erice-Sicily*, Italy: 19 – 26 April 2012
2. Galanzha EI (Invited oral presentation), Recent advances of *in vivo* flow cytometry. SPIE Photonics Europe Symposium, 2012, Brussel, Belgium: 16-29 April 2012

3. Galanzha EI (Oral presentation), In vivo blood flow and lymphatic examination for early diagnosis and therapy of tumor metastasis, The 8th Joint National Medical & Scientific Conference (RAMA, RADA, RASA), Las Vegas, NV: 13-16 October, 2011
4. Zharov VP. (Invited oral presentation) Gold, Diamonds, and Glass: New Frontiers in Oncologic Imaging and Treatment with Nanotechnology. Radiological Society of North America (RSNA), 26-27, November 2012, Chicago, IL.
5. Zharov VP. (Invited oral presentation) Nanotechnology-based diagnosis and treatment of cancer metastasis. Nanotechnology Conference Nanotechnology for Medicine and Dentistry. October 31 to 3 November 2012, Cancun, Mexico.
6. Zharov VP. (Invited oral presentation) Advanced Platform for Real-Time Monitoring of Circulating Tumor Cells Beyond the Detection Limits. Oral presentation. February 2013, San Francisco, CA. Molecular Med Tri-Con: Circulating Tumor Cells
7. Mazen A. Juratli M.D., Ekaterina I. Galanzha, Mustafa Sarimollaoglu, Dmitry A. Nedosekin, James Y. Suen M.D., Vladimir P. Zharov. (Poster presentation) Photoacoustic monitoring of clot formation during surgery and tumor surgery. SPIE Photonics West 2013, February 2013, San Francisco, CA.
8. Mazen A. Juratli M.D., Ekaterina I. Galanzha, Mustafa Sarimollaoglu, Dmitry A. Nedosekin, James Y. Suen M.D., Vladimir P. Zharov. (Poster presentation). In vivo detection of circulating tumor cells during tumor manipulation. SPIE Photonics West 2013, February 2013, San Francisco, CA.
9. Mustafa Sarimollaoglu, Dmitry Nedosekin, Ekaterina Galanzha (Oral presentation). Identification of rolling circulating tumor cells using photoacoustic time-of-flight method. SPIE Photonics West 2013, February 2013, San Francisco, USA.
10. Zharov VP. (Hot Topic Oral Presentation) Photoacoustic Flow Cytometry: Journey in the Blood. SPIE Photonics West 2013, February 2013, San Francisco, CA.
11. Galanzha EI. (Invited oral presentation) in vivo universal flow cytometry for detection of circulating tumor cells in blood, lymph, and cerebrospinal fluid. SPIE Photonics West 2013, February 2013, San Francisco, CA.
12. Galanzha EI. (Oral presentation). Negative dynamic photoacoustic contrast: principle and application. SPIE Photonics West 2013, February 2013, San Francisco, CA.

### Paper in preparation:

Mazen A. Juratli, Mustafa Sarimollaoglu, Dmitry Nedosekin, Vladimir P. Zharov, Ekaterina I. Galanzha. In vivo clotting of circulating cancer stem cells and platelets in metastasis progression. Nature medicine.

### CONCLUSION

We successfully demonstrated for the first time molecular identification of CSCPAs *in vivo*, that can advance general understanding of cancer stem cell biology. We completed all studies related to this project. Specifically, a novel approach using the principle of flow cytometry with multispectral high-pulse-repetition-rate lasers and bioconjugated NPs as high-contrast molecular contrast agents was developed for highly-sensitive detection and enumeration rare CSCPAs in blood circulation *in vivo*. The feasibility of this approach was demonstrated to molecularly detect CSCPAs and single CSCs during development of metastatic disease in mouse model of human breast cancer.

*In vitro* and *in vivo* verifications allowed us to estimate significant targeting efficacy of cells of interest with the molecular contrast agents. We established optimal laser and NP's parameters for labeling single cells in blood circulation and for their *in vivo* FC's detection against a background of blood.

The preliminary analysis of the obtained results from multichannel FC revealed that the software that we used was non optimal, provided some false signals (e.g., due to overlapping signals from two and three channels). This led to the biological challenges to interpret obtained results.

During one year extension, we successfully optimized software, developed advanced signal acquisition, re-analyzed all PA data and published some results. Based on obtained data we are also preparing a manuscript to the Nature-publishing group journal.

In addition, our research revealed several challenges must be overcome before *in vivo* CSCPAs reach their full clinical potential including detailed assessment of individual dynamic of CSCPAs and various molecular profiles characterizing aggressive CTCs (e.g., CTCs expressed mesenchymal markers as result of EMT).

Summarized outcomes that have resulted from this research we outline strategies to overcome existing challenges and facilitate further development. For example, with future DOD Breast cancer research Programs (e.g., Breakthrough Award) funding, the research program will focus on (1) development of new generations of *in vivo* PA flow cytometers with negative and positive contrast to increase the number of parameters identified and improve specificity; (2) using this approach to decipher *in vivo* kinetics of CSCPAs as well as other aggregates of CTCs (e.g., CSCs with WBCs or CTCs expressed mesenchymal markers with platelets) produced after inoculating cancer cells obtained from tissue samples of cancer patients; and (3) translation of this research to the development of a portable flow cytometer with parameters that are safe for human use for clinically relevant earlier diagnosis, prevention, and effective individualized treatment of cancer.

## REFERENCES

1. Galanzha EI, Zharov VP. Photoacoustic flow cytometry. Methods. 2012 Jul;57(3):280-96.
2. Nedosekin DA, Juratli MA, Sarimollaoglu M, Moore CL, Rusch NJ, Smeltzer MS, Zharov VP, Galanzha EI. Photoacoustic and photothermal detection of circulating tumor cells, bacteria and nanoparticles in cerebrospinal fluid *in vivo* and *ex vivo*. J Biophotonics. 2013;6:523-33.
3. Nedosekin DA, Sarimollaoglu M, Galanzha EI, Sawant R, Torchilin VP, Verkhusha VV, Ma J, Frank MH, Biris AS, Zharov VP. Synergy of photoacoustic and fluorescence flow cytometry of circulating cells with negative and positive contrasts. J Biophotonics. 2013;6:425-34.
4. Galanzha EI, Sarimollaoglu M, Nedosekin DA, Keyrouz SG, Mehta JL, Zharov VP. In vivo flow cytometry of circulating clots using negative photothermal and photoacoustic contrasts. Cytometry A. 2011 Oct;79(10):814-24. (this original manuscript introduced the principle of photoacoustic dynamic negative contrast in biomedical research)
5. Kim JW, Galanzha EI, Zaharoff DA, Griffin RJ, Zharov VP. Nanotheranostics of circulating tumor cells, infections and other pathological features *in vivo*. Mol Pharm. 2013;10:813-30.
6. Mazen A. Juratli M.D., Ekaterina I. Galanzha, Mustafa Sarimollaoglu, Dmitry A. Nedosekin, James Y. Suen M.D., Vladimir P. Zharov. Photoacoustic monitoring of clot formation during surgery and tumor surgery. SPIE Proc.: Photons Plus Ultrasound: Imaging and Sensing 8581, 2013.

## LIST OF THE PERSONNEL RECEIVING PAY FROM THE RESEARCH EFFORT.

- Ekaterina Galanzha, the PI
- Vladimir P.Zharov, Co-Investigator
- Dmitry A. Nedosekin
- Stephen Foster

## FIGURES

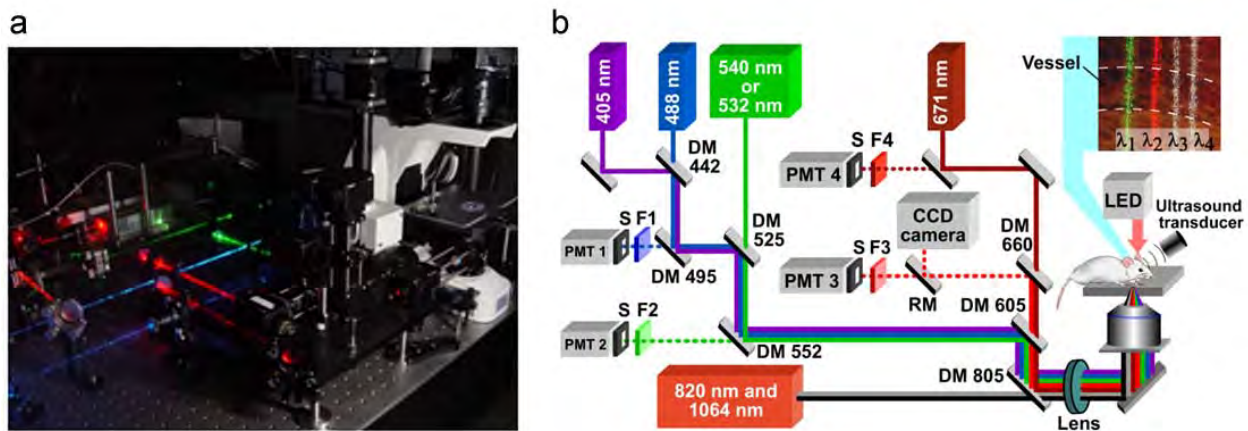


**Figure 1.** *In vivo* multicolor flow cytometry. (a) External view. (b) General schematic.

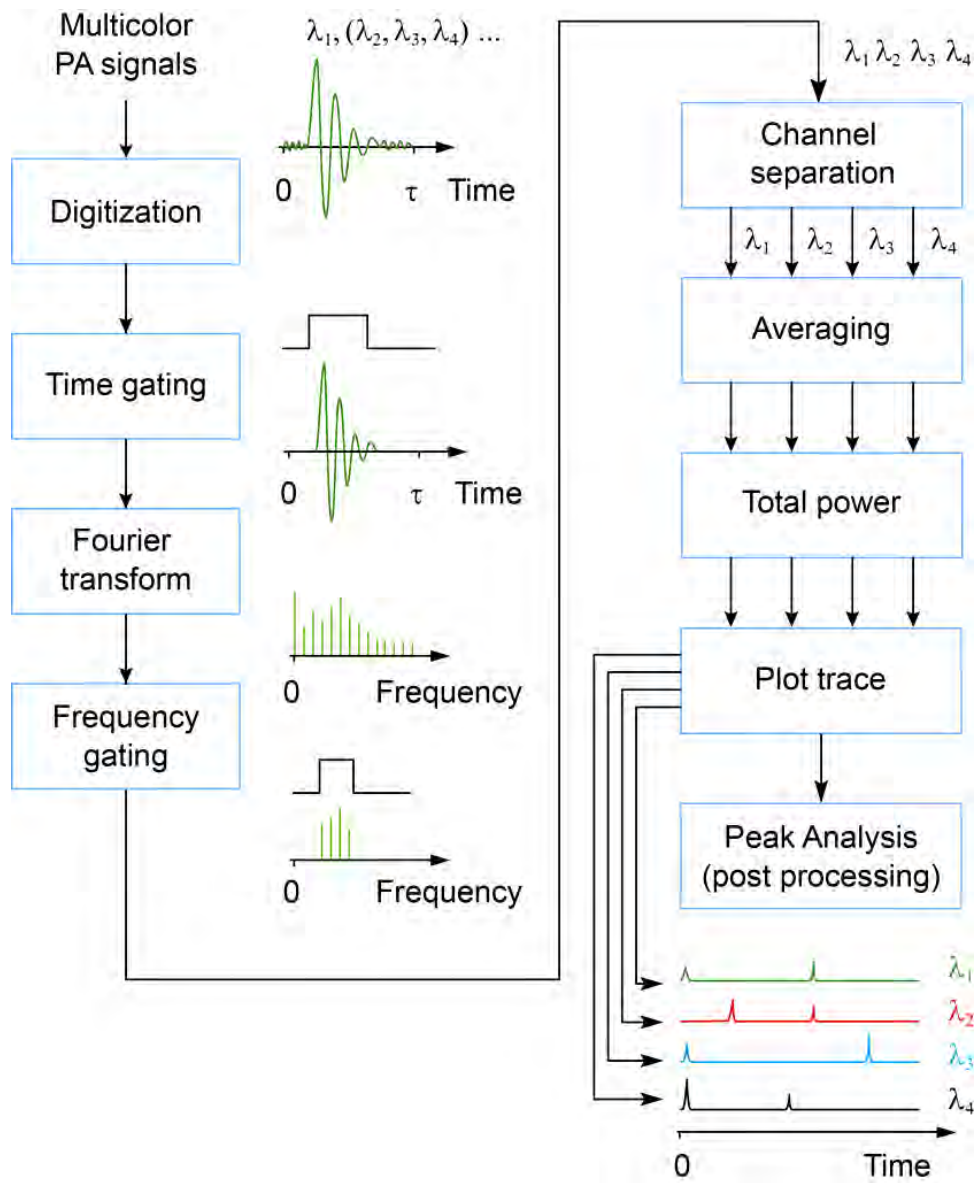


**Figure 2.** PAFC signal acquisition

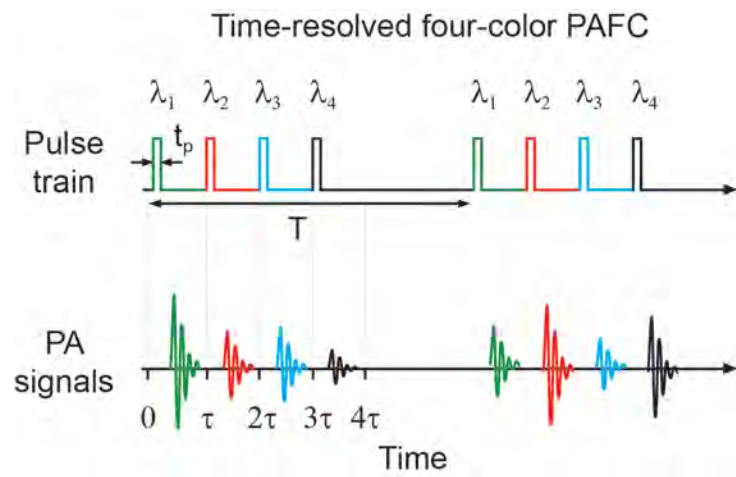


**Figure 3.** Temporal separation of lasers for PAFC.

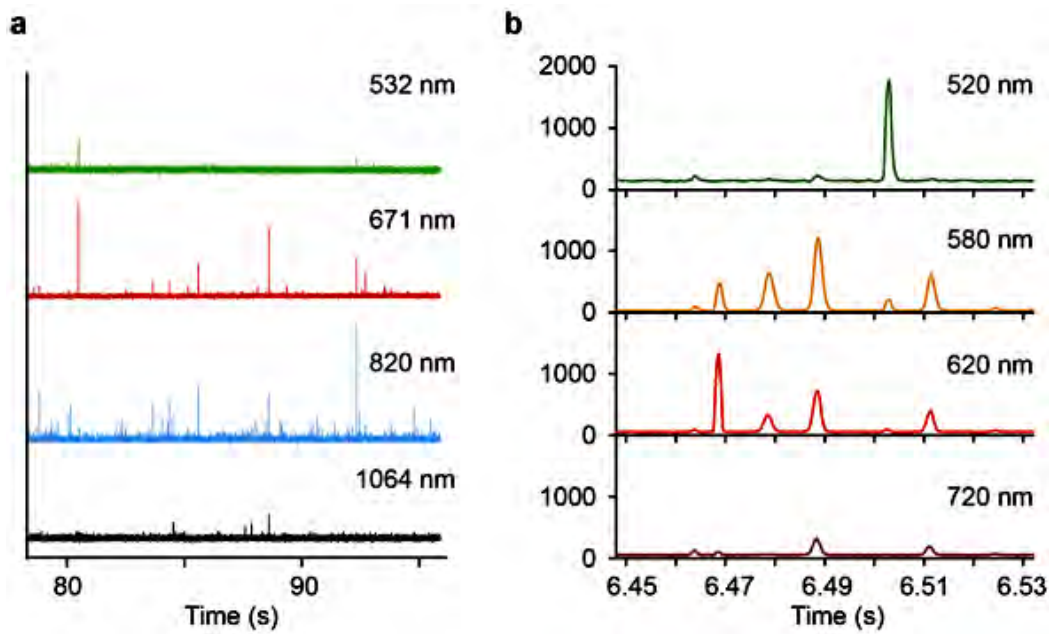


**Figure 4.** Examples of FC's traces. (a) PAFC's trace. (b) FFC's trace.

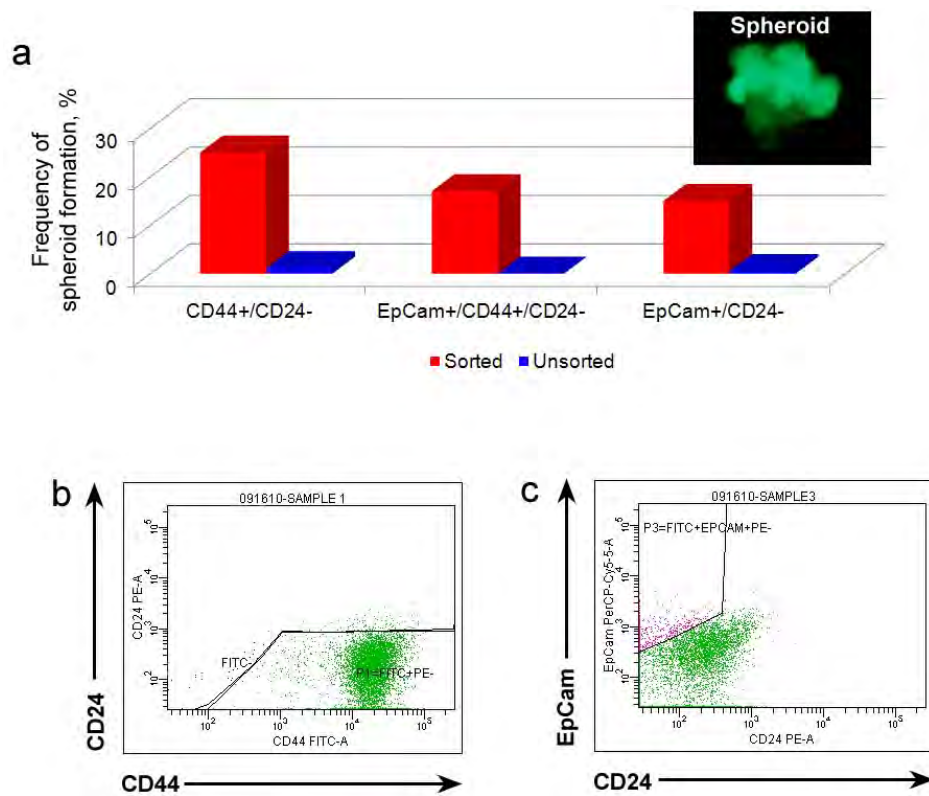


**Figure 5.** Cancer stem cell properties and molecular characterization of MDA-MB-231 breast cancer cells. **(a)** Percentage of spheroid formation for sorted stem-like populations and unsorted breast cancer cells; inset: CSC growing as spheroid. **(b)** Conventional FC dot plots of CD44 and CD24 expression (green dots). **(c)** Conventional FC dot plots of EpCam and CD24 expression (purple dots).

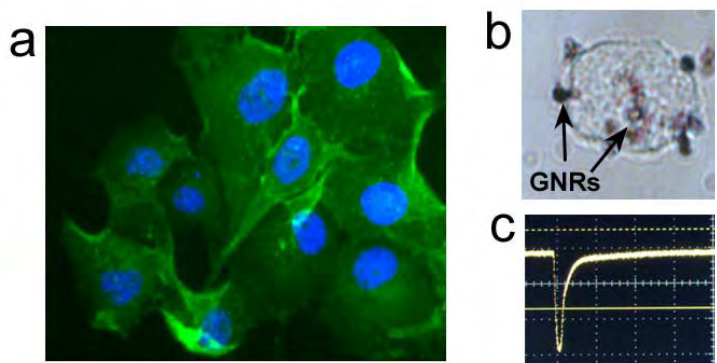


**Figure 6.** (a) Immunohistochemistry of breast cancer cells expressing GFP and labeled with DAPI. (b) High resolution optical image of the breast cancer cell labeled with GNR670 (dark spots are large GNR clusters); (c) PT signal from the labeled breast cancer. Laser parameters: wavelength, 650 nm; fluence,  $80 \text{ mJ/cm}^2$ .

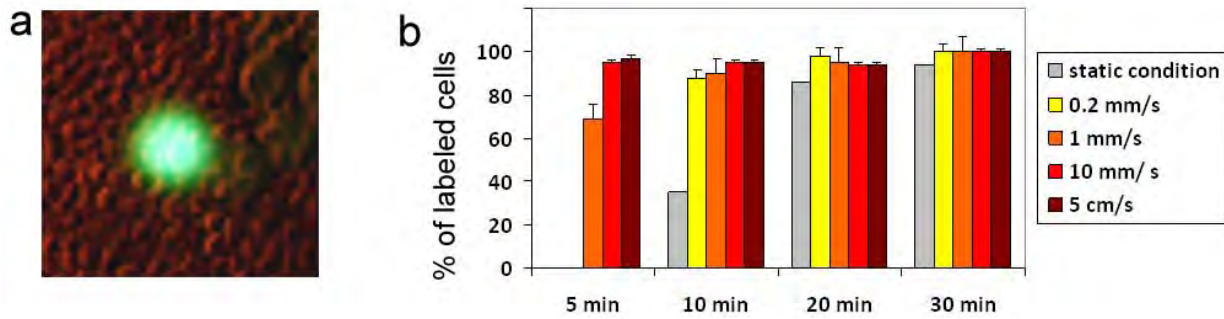


**Figure 7.** (a) Integrated fluorescent and transmission images of blood sample spiked with breast cancer cells (green). (b) Labeling efficiency of breast cancer cells spiked with blood in flow *in vitro*.

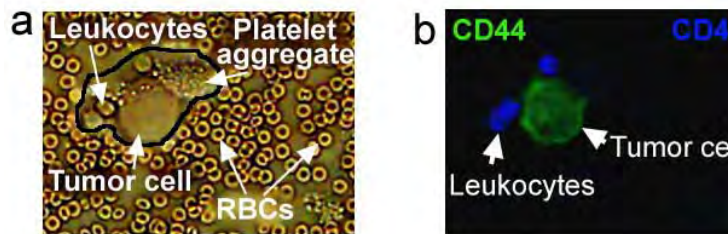


**Figure 8.** Formation CSCPA in the blood sample circulating *in vitro*: **(a)** transmission and **(b)** fluorescent images of aggregates consisting of platelets, CD44+/CD24-/CD45- breast tumor cells, and CD45+ leukocytes that were formed in blood flow in glass tubes at the velocity of 1 mm/s. Cells in the aggregate can be identified by their sizes (tumor cells>leukocyte>platelet) in optical images; molecular profile was identified by labeling cancer cells with CD44 (FITC-conjugated antibodies) and CD24 (PE-conjugated antibodies) and leukocytes for CD45 (V450-conjugated antibodies).

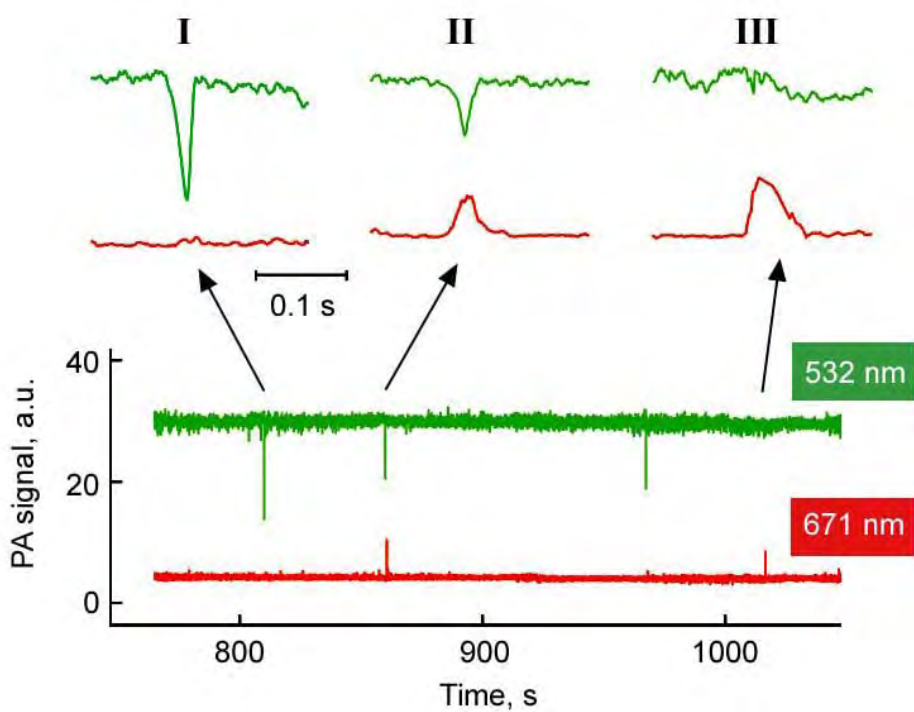


**Figure 9.** Detection of circulating CSCPAs, CSCs and platelet aggregates in blood *in vivo* with PAFC.

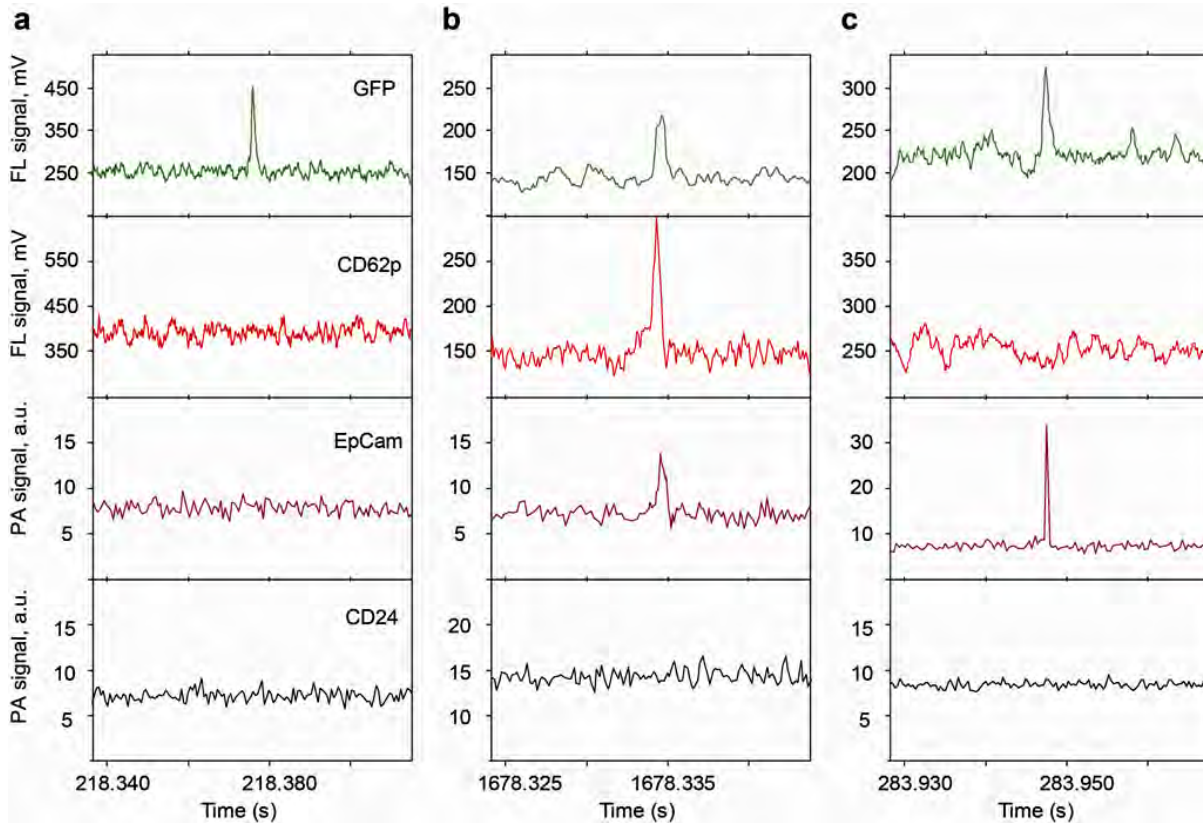


**Figure 10.** *In vivo* PAFFC of the tumor-bearing mouse at week 8 of tumor development. **(a)** High-amplitude signal in the GFP-related FC's channel and no signals in other channels represent single bulk CTC with profile GFP+/EpCam-/CD24-/CD62P-. **(b)** High-amplitude coincident signals in the GFP-related, EpCam-related and CD62P-related channels and the absence of signals in CD24-related channel represent CSCPA with profile GFP+/EpCam+/CD24-/CD62P+. **(c)** High-amplitude coincident signals in the GFP-related and EpCam-related channels and the absence of signals in CD24-related and CD62P-related channels represent single CSC with profile GFP+/EpCam+/CD24-/CD62P-.

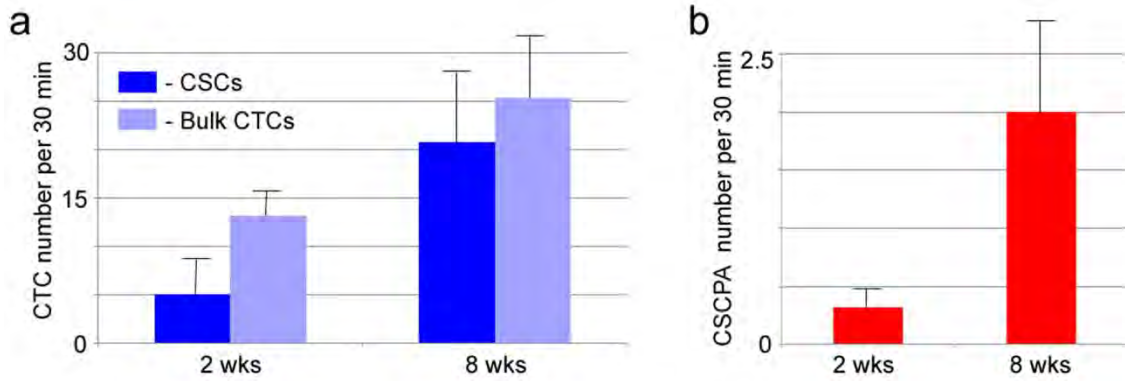


**Figure 11.** Dynamic of single CTCs (a) and CSCPAs (b) in breast-cancer-bearing mice.

## **APPENDICES**

1. Galanzha EI, Zharov VP. Photoacoustic flow cytometry. Methods. 2012;57:280-296.
2. Kim JW, Galanzha EI, Zaharoff DA, Griffin RJ, Zharov VP. Nanotheranostics of circulating tumor cells, infections and other pathological features in vivo. Mol Pharm. 2013;10:813-830.



## Methods

journal homepage: [www.elsevier.com/locate/ymeth](http://www.elsevier.com/locate/ymeth)

### Review Article

## Photoacoustic flow cytometry

Ekaterina I. Galanzha<sup>a</sup>, Vladimir P. Zharov<sup>a,b,\*</sup><sup>a</sup> Phillips Classic Laser and Nanomedicine Laboratories, University of Arkansas for Medical Sciences, Little Rock, Arkansas 72205, USA<sup>b</sup> Arkansas Nanomedicine Center, University of Arkansas for Medical Sciences, Little Rock, Arkansas 72205, USA

### ARTICLE INFO

#### Article history:

Available online 26 June 2012

#### Keywords:

*In vivo* flow cytometry  
Photoacoustic spectroscopy  
Negative contrasts  
Blood and lymph flow  
Cerebrospinal fluids  
Circulating tumor cells  
Clots  
Sickle cells  
Red blood cell aggregation  
Ultrasharp plasmonic resonances

### ABSTRACT

Conventional flow cytometry using scattering and fluorescent detection methods has been a fundamental tool of biological discoveries for many years. Invasive extraction of cells from a living organism, however, may lead to changes in cell properties and prevents the long-term study of cells in their native environment. Here, we summarize recent advances of new generation flow cytometry for *in vivo* noninvasive label-free or targeted detection of cells in blood, lymph, bone, cerebral and plant vasculatures using photoacoustic (PA) detection techniques, multispectral high-pulse-repetition-rate lasers, tunable ultra-sharp (up to 0.8 nm) rainbow plasmonic nanopropes, positive and negative PA contrasts, *in vivo* magnetic enrichment, time-of-flight cell velocity measurement, PA spectral analysis, and integration of PA, photo-thermal (PT), fluorescent, and Raman methods. Unique applications of this tool are reviewed with a focus on ultrasensitive detection of normal blood cells at different functional states (e.g., apoptotic and necrotic) and rare abnormal cells including circulating tumor cells (CTCs), cancer stem cells, pathogens, clots, sickle cells as well as pharmokinetics of nanoparticles, dyes, microbubbles and drug nanocarriers. Using this tool we discovered that palpation, biopsy, or surgery can enhance CTC release from primary tumors, increasing the risk of metastasis. The novel fluctuation flow cytometry provided the opportunity for the dynamic study of blood rheology including red blood cell aggregation and clot formation in different medical conditions (e.g., blood disorders, cancer, or surgery). Theranostics, as a combination of PA diagnosis and PT nanobubble-amplified multiplex therapy, was used for eradication of CTCs, purging of infected blood, and thrombolysis of clots using PA guidance to control therapy efficiency. *In vivo* flow cytometry using a portable fiber-based devices can provide a breakthrough platform for early diagnosis of cancer, infection and cardiovascular disorders with a potential to inhibit, if not prevent, metastasis, sepsis, and strokes or heart attack by well-timed personalized therapy.

© 2012 Elsevier Inc. All rights reserved.

### 1. Introduction

Flow cytometry is a well-established powerful analytical tool that has led to many revolutionary discoveries in cell biology and molecular disease diagnosis [1–2]. In conventional flow cytometry, cells are introduced into a high speed (up to few m/s) laminar artificial flow. After focusing the cells into a single file, laser-induced fluorescence, and/or forward and sideways scattered lights emitted from the cells are detected using photodetector arrays with spectral filters. This highly accurate technology provides fast (a few million cells in a minute), multiparameter quantification of the biological properties of individual cells at subcellular and molecular levels, including their functional states, morphology, composition, proliferation, and protein expression.

Nevertheless, invasive extraction of cells from a living system may alter cell properties (e.g., morphology or marker expression)

and prevent the long-term study of cells (e.g., cell-to-cell interactions, aggregation or rolling) in their natural biological environment. Other limitations include low sensitivity for detection of rare circulating tumor cells (CTCs), bacteria, sickle cells and clots due to a small blood sample volume, and the discontinuity of sampling with limited, discrete time points. These shortcomings can be solved by the development of *in vivo* flow cytometry which allows noninvasive, continuous assessment of the large blood volume circulating in the blood vessels. However, the adaptation of flow cytometry principles from *in vitro* application with cells flowing in a well-controlled single file, to *in vivo* studies using the blood and lymph vessels as natural tubes with native cell flow faces many challenges. These include: (1) poor optical conditions such as absorption, scattering, and autofluorescent background from the vessel wall, surrounding tissue and bulk blood cells; (2) multiple-file cell flow in vessel cross-sections; (3) difficulties of accessing deep vessels; (4) problems with the use of a transillumination (forward) or sideways optical schemes; and (5) instability of blood, and especially, lymph-flow parameters (e.g., fluctuation of cell velocity and the positions of cells in vessel cross-sections). These

\* Corresponding author at: Phillips Classic Laser and Nanomedicine Laboratories, University of Arkansas for Medical Sciences, Little Rock, Arkansas 72205, USA.

E-mail address: [zharovvladimir@uams.edu](mailto:zharovvladimir@uams.edu) (V.P. Zharov).

limitations require some precautions in the choices of a vessel location, detection system, and proper animal models as a first step toward transitioning this technique to human applications.

A brief history, features and challenges of this new generation of flow cytometry using photothermal (PT), photoacoustic (PA), fluorescence, transmission, and Raman detection methods were recently reviewed with focus on previous work in this field before 2009 [3]. In particular, the first pioneer's efforts resulting in the development of *in vivo* flow cytometry with PT, PA, and scattering detection techniques [4–23], were summarized in book chapters [24–26]. It included real-time detection of circulating red and white blood cells (RBCs and WBCs respectively) in different functional states (e.g., normal and apoptotic), CTCs (squamous carcinoma), bacteria (*Escherichia coli* and *Staphylococcus aureus*), nanoparticles (NPs) (e.g., gold nanorods [GNRs], carbon nanotubes [CNTs], and magnetic NPs [MNPs]), dyes (e.g., Lymphazurin, Evans blue, and Indocyanine Green [ICG]), the use of lymph valves as natural nozzles to focus cells into a single file *in vivo*, minimally invasive flow cytometry with fiber inside vessels [30], and *in vitro* PA flow cytometry (PAFC) [30,33] for verification of PA data *in vivo*.

Here, we summarize recent advances of PAFC platform and its new applications [27–42]. The technical PAFC's improvements include high-pulse repetition-rate lasers, fast signal acquisition algorithms, time-of-flight measurement of cell velocities, focused ultrasound transducers for the assessment of deep vessels, ultra-sharp rainbow NPs as high-contrast molecular PA and PT theranostic nanoprobes with super-narrow tunable spectral PA and PT resonances (up to 0.8 nm), *in vivo* high speed image flow cytometry of cells of interest at velocities up to 2 m/s, *in vivo* fluctuation flow cytometry, integration of PAFC and fluorescent cytometry with positive and negative contrast modes, and the combination of PA diagnosis and PT therapy (PA-PT nano-theranostics). The new applications include: (1) label-free monitoring of melanoma CTCs released during palpation, biopsy, and conventional and laser surgery; (2) multiplex targeting, magnetic enrichment, and detection of breast bulk and stem CTCs; (3) PA detection of CTCs (called also disseminated tumor cells) in lymphatics as the earliest prognostic marker of metastasis compared to sentinel lymph node and blood assessment; (4) targeted detection of pathogens within the bloodstream at a single bacteria level; (5) PA blood rheology including real-time monitoring of RBC aggregation; (6) identification of sickle cells; (7) study of cell death in blood circulation; (8) study of pharmacokinetics of NPs, liposomes, dyes and other contrast agents including their dynamic interaction with blood cells; (9) cell and NP identification based on their different velocities in blood flow; (10) theranostics as real-time, PAFC-guided, PT elimination of CTCs and bacteria from circulation [30], and (11) a minimally-invasive delivery of laser radiation to deep vessels inside the body using a fiber in a tiny needle or catheter.

## 2. Principle of *in vivo* flow cytometry with positive and negative contrasts

### 2.1. General schematics

The underlying principle of *in vivo* flow cytometry with a PA detection schematic (referred to as PAFC) is based on the irradiation of selected vessels using short laser pulses followed by time-resolved detection of laser-induced acoustic waves (referred to as PA signals) with an ultrasound transducer gently held against the skin (Fig. 1A, right). The physical mechanism of PAFC is based upon the PA effect associated with fast (picosecond scale) nonradiative relaxation of absorbed laser energy into heat and then the thermo-elastic generation of acoustic waves [43–49]. PAFC as a combination of laser and ultrasound techniques has a high sensitivity and

spectral specificity of optical methods and a high spatial resolution and depth penetration of ultrasound methods. Fig. 1B illustrates a typical PA signal trace that occurred during label-free detection of melanoma CTCs (B16F10) on the tumor-bearing mouse model. Each individual peak in this trace obtained by averaging many PA signals (20–100) is associated with individual single or aggregated CTCs.

Most studies were performed on well-distinguished, 30–70- $\mu$ m diameter blood vessels located approximately 40–100  $\mu$ m deep in the thin ear (~250  $\mu$ m) of the nude mouse model, and on 200–300- $\mu$ m diameter blood vessels in the abdominal area of the nude mouse at a depth of 0.3–0.5 mm, or on the aorta (0.9–1 mm) at a depth of 2–4 mm [30]. The mice were anesthetized using a standardized procedure and placed on a heated microscope stage with the ear spread flat over a glass slide. The ultrasound transducer was acoustically connected to the mouse's ear using warm water, or conventional ultrasound gel, topically applied on the biotissue. In particular, the transducer can be placed in a small cylindrical water tank with a flexible transparent membrane attached to skin.

Laser radiation can be delivered to biotissue either by using a microscope schematic with a customized condenser to create the desired linear beam shapes (e.g., from 5 × 50 to 25 × 150  $\mu$ m), or a fiber with a miniature tip and cylindrical optics. PAFC offers the highest absorption sensitivity at the single-cell level which allows noninvasive (a temperature elevation  $\leq 0.1$  °C) detection and imaging of individual cells. PAFC molecular specificity is provided either by label-free intrinsic absorption spectroscopic contrast (e.g., from hemoglobin [Hb], melanin or cytochromes [Cyt]), or by strongly absorbing, low-toxicity, functionalized NPs. The spatial resolution at the level of 5–10  $\mu$ m in superficial 30–70  $\mu$ m in diameter vessels at a depth of 0.1–0.5 mm is determined by optical focal parameters, while in deeper tissue with strong light scattering, the resolution depends upon ultrasonic focal parameters (e.g., 100–20  $\mu$ m at a frequency of 10–50 MHz, respectively). The focused cylindrical ultrasound transducer provides a minimal detected volume due to high lateral resolution with simultaneous assessment the entire cross section of a vessel. The attenuation of ultrasound waves at typical frequencies of 5–30 MHz is almost negligible (~0.6 dB cm<sup>-1</sup> MHz<sup>-1</sup>) for depths of 1–5 mm [46,47]. Indeed, the PA technique demonstrated an advantage in assessing deep vessels *in vivo* at typical levels of 0.5–1 cm with a few studies at 5–7 cm, compared to other optical modalities [46].

### 2.2. Lasers, transducers and signal acquisition algorithm

To expose each fast moving cell, the laser pulse rate,  $f$ , should be  $f \geq 1/t_L$ , where  $t_L = (D + d)/V_F$  is the lifetime of the moving cell in the detection volume,  $D$  is the cell diameter,  $d$  is the width of the linear laser beam, and  $V_F$  is the velocity of the cell [15]. For  $D \approx d \approx 10$   $\mu$ m, in vessels with diameters of 50  $\mu$ m, 2 mm (e.g., hand vein), and 1 cm (e.g., carotid artery) having different velocities pulse rates will be  $f \geq 500$  Hz, 2 kHz, and 50 kHz, respectively. To improve signal-to-noise ratios (SNRs) by averaging PA signals from each exposed cell without temporal overlapping of thermal effects,  $f$  can be increased until  $f \leq 1/\tau_T$ , where  $\tau_T = D^2/28 k$  is the thermal relaxation time (for a spherical target with diameter of  $D$ ), and  $k$  the thermal diffusion [39]. For  $D = 10$   $\mu$ m and  $k = 1.4 \times 10^{-7}$  m<sup>2</sup>/s (for water),  $f \leq 25$  kHz. The number of PA signals from one cell,  $N$ , can be estimated from the equation  $N = f \times t_L$  (e.g.,  $N = 40$  for  $V_F = 5$  mm/s and  $f = 10$  kHz). The effective generation of PA signals requires acoustic confinement for a laser pulse duration  $t_p \leq D/c_s$  [44–46], where  $c_s$  is the speed of sound. For a typical cell size of 10–15  $\mu$ m and  $c_s = 1.5 \times 10^5$  cm/s (for water),  $t_p \leq 10$  ns. For smaller targets, such as single melanin or plasmonic NPs with sizes of 30–100 nm  $t_p \leq 50$ –500 ps.

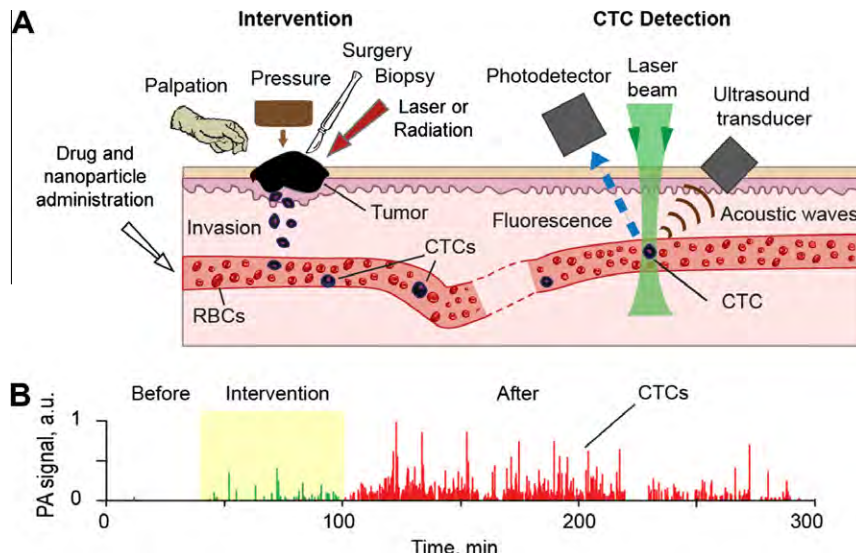


**Fig. 1.** *In vivo* integrated PA and fluorescence flow cytometry. (A) Schematic for simultaneous detection of circulating cells (e.g., CTCs) with both absorption and fluorescence properties (right) during diagnostic and therapeutic interventions (left). (B) Example of a PA signal trace produced by melanoma CTCs (B16F10-GFP) in microvessels of the mouse ear before, during, and after pressure (120 g) applied on ~5 mm skin tumor. This figure is from a paper Mazen et al. [72].

Our setup was equipped with five high-pulse-repetition-rate nanosecond lasers with the following parameters: (1) wavelength, 532 nm; pulse energy, 100  $\mu$ J; pulse width, 5 ns; and repetitions rate, up to 100 kHz (model: LUCE 532, Bright Solutions, Italy); (2) 671 nm, 35  $\mu$ J, 25 ns, and 100 kHz (model: QL671-500, CrystaLaser, USA); (3) adjustable spectral range, 720–890 nm (820 nm used in most studies); 75  $\mu$ J, 8 ns, and 30 kHz (model: LUCE 820, Bright Solutions); (4) 904 nm, 5  $\mu$ J, 15 ns, 10 kHz (diode laser, model 905-FD1S3J08S, Frankfurt Laser Company); and (5) 1064 nm, 100  $\mu$ J, 10 ns, and 1–750 kHz (model: MOPA-M-10, Multiwave Photonics, Portugal). The laser beams were navigated on selected blood vessels with an X-Y motorized stage using a controller (STG4400ML, Conix Research, Inc., Springfield, OR) under the optical imaging guidance. In most applications, the pulse-repetition rate for these lasers was 10 kHz and in selected studies, up to 500 kHz [33]. Laser pulses were triggered by a digital delay/pulse generator (DG645, Stanford Research Systems, USA). The selected contrast agents (e.g., NPs, or dyes) displayed peaks in the absorption spectra coinciding with the laser wavelength used (e.g., 532, 671, 820, 904, and 1064 nm).

The PA signals had a bipolar shape with a typical duration of 0.1–1  $\mu$ s. They were usually transformed into a short pulse train (Fig. 2A, top right) because of the reflection and resonance effects in the transducer holder. PA signals were detected by ultrasound transducers (e.g., unfocused: model 6528101, 3.5 MHz, 5.5 mm in diameter, Imasonic Inc., Besançon, France; and focused: model V316-SM, 20 MHz, focal length 12.5 mm, Panametrics) and then amplified (amplifier models: 5662, bandwidth 50 kHz–5 MHz, gain 54 dB; and 5678, 40 MHz, gain 60 dB, both from Panametrics-NDT, Olympus). To collect PA signals, the PAFC setups were equipped with a high-speed, analog-to-digital converter boards (e.g., National Instruments Corp.). In analogy to conventional flow cytometry, final PA data were presented as PA signal traces (Fig. 1B) which were analyzed using customized software. A real-time and post-processing operations were performed using MATLAB. The customized peak analyzer identifies the baseline in the trace, sets the threshold level based on the mean and a multiple of the standard deviation, selects the peaks above this threshold, and finally performs statistical analysis by acquiring time stamps, amplitudes, and widths of the detected peaks.

### 2.3. Combination of photoacoustic, fluorescent, and photothermal methods with positive and negative contrast modes

The use of a single technique limits the range of detectable cells with different optical properties. To increase the number of detectable cells, conventional flow cytometry usually integrates fluorescent, and scattering detection methods. In 2005 we proposed the integration of PT, PA, fluorescence and scattering detection methods for *in vivo* flow cytometry [9,10] which were previously used separately only [3–40,50–54]. Recently, we demonstrated advances of real-time integration of PAFC and fluorescent flow cytometry (FFC) termed as PAFFC [42] using pulsed and continuous wave (CW) lasers as traditional sources for the generation of PA and fluorescent signals, respectively (Fig. 1A). In addition, we showed the opportunity to use pulsed lasers only for the simultaneous generation of both signals that simplified the PAFFC schematic and provided time-resolved discrimination of objects with different lifetimes (e.g., quantum dots with long fluorescence compared to blood that has a shorter autofluorescence background).

Conventional PA and fluorescence techniques use preferential positive imaging contrasts when signals from strongly absorbing or fluorescent cells are above absorption or autofluorescence background, respectively. In particular, laser irradiation of blood vessels creates a constant PA background associated with absorption of the high number of RBCs in the irradiated volume. Thus, to be detected using the positive contrast mode, targets must have higher absorption compared to the RBC background as in the case of pigmented melanoma cells [30] or cells targeted by strongly absorbing NPs [28]. In PAFFC, conventional positive contrast mode was combined with the new negative PA and fluorescent contrast modes, in particular, for PA detection of cells having lower absorption than RBCs as in case of platelets or WBCs (Fig. 2B). When weakly absorbing (e.g., platelet rich white clot, Fig. 2A) or low fluorescent cells pass through laser-irradiated vessel volume, a transient decrease of the absorption or fluorescence results in a sharp negative PA and fluorescent peaks in blood absorption and the fluorescence background, respectively (Fig. 2C, middle). Thus, absorption and auto-fluorescence background as a problem in conventional positive contrast PAFC and FFC is transformed to an advantage using negative contrast PAFC, FFC, and especially its combination in PAFFC.

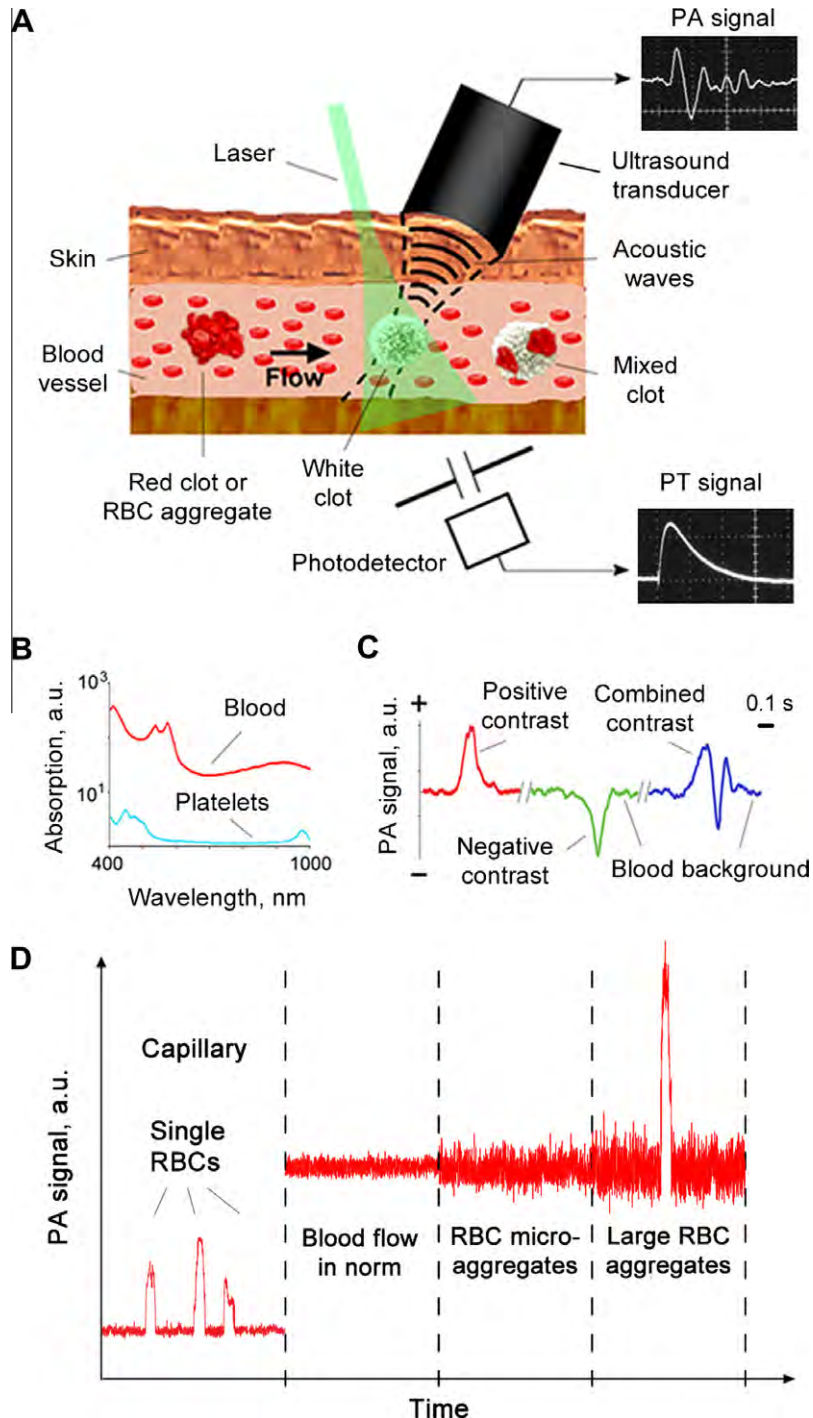


**Fig. 2.** The principles of fluctuation positive and negative contrast PA flow cytometry. (A) Schematic. (B) Absorption spectra of whole blood (red) and platelet-rich plasma (blue). (C) Example of PA positive, negative, and combined contrasts from circulating clots of different compositions. (D) PA signal trace dynamics obtained with PA fluctuation flow cytometry in different vessels in normal and pathological conditions leading to RBC aggregation.

The negative contrast can be used for label-free counting of RBCs, WBCs, and red (with dominant RBC content), white (with dominant platelet content), and combined clots (Fig. 2C, right) (see Section 6). Negative contrasts of cells can be enhanced either by their targeting with negative PA and fluorescent probes (e.g., weakly absorbing or fluorescent beads, respectively), or by increasing background through the injection of absorbing or fluorescent contrast agents. The appearance of many small negative and positive contrast objects in the detected volume, such as mixed red-white clots or RBC aggregates leads to the generation of the fluctuated

PA background which is the primary subject of *in vivo* fluctuation flow cytometry (Fig. 2D) (Section 6).

PAFC was also integrated with a PT flow cytometry (PTFC) [10,14] which was also used for verification of PA data. In the PT imaging mode [8–10,55,56], irradiation (e.g., using tunable optical parametric oscillator with wavelength of 415–2300 nm, pulse width of 8 ns, pulse rate of 100 Hz and pulse energy of 0.1–500  $\mu$ J) of absorbing objects leads to temperature-dependent variations of the refractive index that are visualized with phase-contrast [55] or a multichannel thermal lens schematic [57] using a second, collinear laser probe

pulse from a Raman shifter (639 nm, 12 ns, 0.01–10 μJ) and a CCD camera. In the PT single-channel thermal lens mode, a laser-induced refractive heterogeneity causes defocusing of a collinear He-Ne laser probe beam (633 nm; power, 1.4 mW) and hence a reduction in the beam's intensity at its center, as detected by a photodiode with a pinhole (referred to as PT signals). PT signals from single cells in a linear mode (i.e., without notable cell photodamage) represent a standard positive peak associated with rapid (pico-nanosecond scale) cell heating and a slower, microsecond scale tail corresponding to cell cooling (Fig. 2A, bottom, right). An advantage of the PAFC is its backward mode (i.e., laser and transducer are on one side), while PTFC has better sensitivity in transillumination mode. PT and PA methods beneficially supplement each other, and in combination, provide a very powerful diagnostic and therapeutic tool. For example, non-invasive PA diagnostics can be integrated with PT killing of metastatic or residual cancer cells, either static or in flow, using more powerful laser pulses triggered by PA signals from these cells.

#### 2.4. Labeling *in vivo*

The great advantage of *in vivo* flow cytometry is the possibility for cell detection without labeling, in particular, by using the positive and negative PA contrast of RBCs and WBCs, respectively, vs. the negative and positive fluorescent contrast of the same cells [42]. In this scenario, PA (or PT) signals can be generated using intrinsic chromophores and pigments such as hemoglobin, melanin, cytochromes, or carotenoids. Cells with a low endogenous absorption can be labeled directly in the bloodstream through intravenous injection of strongly absorbing functionalized NPs [28,37,40,42]. Depending upon cell and NP properties, the labeling procedure using mouse models takes from 10–20 min to one hour. High labeling specificity is provided through the selection of molecular markers that are highly expressed in targeted cells (e.g., CTCs), but almost absent in normal blood and endothelial cells (e.g., folates in CTCs) [28,51]. High labeling efficiency is associated with frequent NP-CTC collisions in partly turbulent blood flow. In accordance with our modeling, injection of  $10^{10}$  NPs into the mouse's blood circulation with a volume of ~2 mL provides, on average,  $\sim 10^3$  NP-CTC collisions per min with expected differences in the velocities of NPs and CTCs  $\leq 1$  mm/s, while their absolute velocities may be 5–10 mm/s. This allows the capture of antibodies by cell surface markers, and the capturing efficiency does not decrease at relative differences in the velocities of NPs and cells at  $\leq 1$ –1.5 mm/s and the shear stress  $\leq 0.5$  dyn/cm<sup>2</sup> [58]. The PA signals from targeted cells with a typical NP number, ranging from 500–5000 NPs per CTC is much higher than the PA background from RBCs, unbound NPs with typical numbers of 1–10 in the detected volume, or from NPs nonspecifically bound to normal blood cells (e.g., macrophages). NP clustering around naturally densely packed cancer markers leads to significant enhancement in PA signals (at least 5–10-fold), and a red-shift effect in the absorption of coupled NPs in clusters [59], both of which serve as indicators of successful cell targeting. In most studies, we optimized the amount of injected NPs which range from  $10^9$ – $10^{10}$  NPs per mouse. These NPs did not produce notable signals immediately after injection, but a latter gradual increase in the PA signal amplitude and rate indicated a successful labeling process. Occasionally, strong PA signals can be observed immediately after intravenous injection of NPs over the period of few minutes, which is associated with NP aggregates which then are quickly (typically within few minutes) cleared from the circulation. To minimize this effect, before the injection, NP clusters are disaggregated by ultrasound and then filtered. Nevertheless, if short lasting signals from NP alone occur immediately after injection, these signals can be differentiated from signals related to cell targeting *in vivo* because the latter appear typically after a time delay.

### 3. *In vivo* real-time detection of circulating tumor cells

Most cancer deaths (up to 90%) are related to metastasis in the distant organs due to the hematogenous dissemination of CTCs shed from the primary tumor. Therefore, enumeration of CTCs appears to be a prognostic marker of metastatic development (the lower the CTC count, the longer the survival), cancer recurrence, and therapeutic efficacy [58]. However, incurable metastases can be developed at the time of the initial diagnosis with existing CTC assays [58] which the current sensitivity threshold of 1–5 CTC/mL (i.e., 5,000–50,000 CTCs in the entire adult blood volume of ~5 L) is limited by the small sample volume (5–10 mL) obtained from the patient. The sensitivity threshold can be improved by assessment of a significantly larger blood volume up to the patient's entire blood volume using *in vivo* PAFC. We demonstrated that PAFC has the potential for label-free detection of melanoma CTCs [30], a multiplex targeted detection of breast CTCs using advanced NPs [28], magnetic enrichment of CTCs *in vivo*, estimation of the efficiency of PT eradication of CTCs, and study of the impact of different interventions on CTC counts.

#### 3.1. Label-free detection of circulating melanoma cells during tumor progression

We selected cutaneous melanoma as an almost ideal model for PAFC technology to provide routine, label-free, *in vivo* clinical assessment of CTCs for earlier detection of the most aggressive and epidemically growing malignancy which often progress to incurable metastasis at a very early stage of the disease. The label-free nature of PAFC when applied to melanoma denotes that PAFC can be translated to clinical application much sooner for melanoma than for other cancers, with obvious and beneficial public-health consequences for this devastating disease. In this study, the over-expression of melanin was used as an intrinsic melanoma cell marker, which provides high PA contrast in the near-infrared (NIR) range in the blood background. Real-time PA counting of metastatic melanoma CTCs (B16F10) was performed in 50 μm-diameter ear mouse vessels, 200-μm abdominal vessels, and the 0.9-mm aorta (with focused ultrasound transducer) during tumor progression in the ear and skin of the nude mouse model (Fig. 3A,B). The CTC rates in these vessels were: 0.05, 2.7, and 91 CTCs/min, respectively (Fig. 3C), underscoring the higher probability of detecting CTCs in larger vessels with higher flow rates, particular the aorta, through which nearly the entire blood volume of a mouse (~2 mL) circulates within 0.5–1 min compared with many hours (up to two days) in the smaller ear vessels. It should be emphasized that cell flow rate even in the mouse aorta is in the range of  $10^7$ – $10^8$  cells/s which is  $10^2$ – $10^3$  times higher than those achieved with modern conventional flow cytometry *in vitro*.

Scanning of a focused laser beam in the vicinity of the primary tumor in the mouse ear (PA scanning cytometry mode) revealed local PA signals from migrating individual or clustered melanoma cells in the first week after tumor inoculation. Metastatic cells appeared in ear microvessels near the tumor on week one with almost no cells detected in the abdominal skin blood vessels. Later, CTCs appeared in the systemic circulation. This indicates a much greater likelihood of detecting the initial metastatic process in the vicinity of the primary tumor before CTCs are disseminated in the large blood pool. The skin tumor growth rate was faster than that of ear tumors, and CTCs also appeared more quickly in the circulation. In particular, by week one, 1–4 CTCs/min were detected in the skin vasculature, and as the tumor size increased, the number of CTCs gradually increased (Fig. 3D) to ~7 and ~12 CTCs/min by 3 and 4 weeks, respectively. On the occasion, either PA signals with complex shapes, or one large PA signal were observed which support the hypothesis

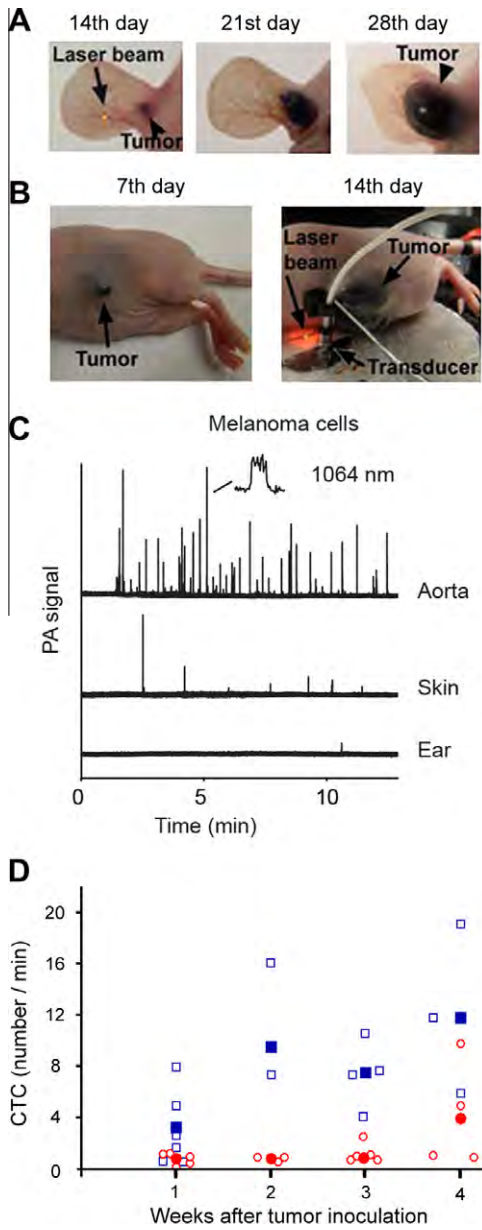


**Fig. 3.** *In vivo* label-free, PA detection of melanoma CTCs. Melanoma tumor growth in the mouse ear (A) and skin (B). (C) Average melanoma CTC rates in the ear and abdominal skin vessels, as well as the aorta, in B16F10 tumor-bearing nude mice 1 week after tumor development. (D) Change in the CTC count in the vessels of the abdominal skin as a function of time after B16F10 tumor cell inoculation in the ear (red empty circle) and skin (blue empty square). The dark red circle and blue square indicate averaged data. Laser parameters: wavelength: 904 nm; pulse energy fluence: 100 mJ/cm<sup>2</sup>; pulse rate: 10 kHz.

of circulating melanoma cells as aggregates. Indeed, optical imaging of ear vessels near a tumor revealed CTC aggregates on the vessel wall, indicating a high probability of CTC aggregating during intravasation.

The mice were euthanized, and tissue sections from different organs (e.g., lung, liver, brain, and lymph nodes) were examined by immunohistochemical staining (see details in [30]). No evidence of metastasis was found during the first 3 weeks after tumor inoculation for the ear tumor model, while PAFC demonstrated early detection of CTCs 4 days after tumor inoculation [30,37]. Thus, CTCs can be readily detected with PAFC weeks before any evidence of detectable with conventional techniques metastasis.

By PA counting rare CTCs in the aorta we estimated PAFC's sensitivity threshold as 0.5–1 CTCs/mL that was verified *ex-vivo* by assessing whole blood volume with scanning PT and PA cytometry [30]. This unprecedented threshold sensitivity on the animal model provides an opportunity to use PAFC as a powerful research tool to study CTC behaviors and CTC's role in metastasis development at an early cancer stage. The PAFC sensitivity has a potential to be further improved 1000-fold (i.e. ~1 CTC/1000 mL) by the examination of a larger blood volume in humans, which is unachievable using existing assays. We recently developed a portable clinical prototype of PAFC using a high-pulse-repetition rate laser at 1064 nm with pulse rates up to 0.5 MHz, fiber delivery of laser radiation, and a focused, ultrasound transducer gently attached to the skin near selected blood vessels. Our future clinical goal is to detect CTCs in hand vessels with diameters of 1–2 mm at 1–3 mm depths (easily accessible with PAFC) in which 3–5 L of blood circulates approximately during one hour. In preclinical testing on the mouse model this device could detect up to 72% of pigmented human melanoma CTCs and approximately 20–40% of low pigmented cells. These data obtained by comparison of PA signals from nonlabeled and labeled by NPs melanoma cells can be used for estimation of the false negative rate and hence the correction of experimental data.

We believe that the PAFC technology may have a tremendous clinical significance due to its high sensitivity and lack of a time-consuming labeling procedure. It can indicate the presence of CTCs in the blood at an extremely low concentration, much below the sensitivity threshold of other methods. Clinical applications may include: (1) blood screening for early CTCs before metastases progression; (2) testing for cancer recurrence; (3) individualized assessment of the therapeutic intervention (e.g., surgery, chemo, or radiation) and its efficiency through real-time CTC counting; and (4) potential for metastasis inhibition, if not prevention by a well-timed therapy. We identified the ways for further PAFC's improvement: (1) decrease the background signals from blood through changes in its oxygenation, osmolarity, and hematocrit, within physiological norms [30]; (2) assessment of CTCs in deep large vessels (e.g., jugular vein) with a focused ultrasound transducer [30]; (3) increase PA contrast by drug-induced activation of melanin synthesis in melanoma cells [30,56]; (4) melanogenesis activation in melanoma and even non-melanoma (e.g., breast cancer) cells via transfection with tyrosinase-activating plasmids [30,56]; (5) use melanin nanoparticles as new PA contrast agents [37] for targeting of melanoma and other nonpigmented CTCs; and (6) targeting of melanoma CTC *in vivo* by magnetic NPs conjugated with specific antibody and magnetic CTC enrichment [37].

### 3.2. Real-time monitoring of circulating tumor cells released during intervention

For many years, oncologists believed that some medical intervention may provoke metastasis; however, no direct evidences were previously presented. Using label-free PAFC and the melanoma-bearing mouse model (Figs. 1A and 3A), we discovered that palpation, biopsy, conventional and laser surgery may either initiate CTC release in the blood which previously did not contain CTCs, or dramatically increase (10–30-fold) the CTC counts above the previous level, which can increase the risk of metastasis. In particular, the 120 g weight pressure or palpation (by squeezing of the melanoma tumor with fingers), notably increased the CTC count (Fig. 1B) that eventually led to the appearance of lung metastasis at week 3 after tumor implantation, compared to no metastasis without the pressure of palpation. The damage of blood vessels in the tumor during biopsy or conventional surgery, modeled by a small, scalpel-induced incision or laser tumor treatment, led also to the appearance of CTCs in the circulation. On the contrary, complete tumor resection by cutting tissue around the localized tumor,

led to the disappearance of CTCs in circulation within a few hours (Fig. 4A), suggesting the primary tumor as the main source of CTCs. However, in several cases, CTCs appeared again in the circulation a few weeks after surgery, which might indicate the influence of metastasis in the distant organs or cancer recurrence in the primary tumor site. Although the animal model was used in this study, our results may warn to oncologists of precaution during physical examination, take a careful surgery plan, or indicate the importance of adjuvant or preventive anti-CTC therapy during primary tumor treatment. Patients should not wear tight clothes to avoid skin pressure above the tumor.

Our data shows that PAFC can be used both as a research tool on animal models to provide insights on the potential of various therapies to provoke metastasis and as a clinical instrument for personalized cancer diagnosis, and for a guidance of appropriate therapy. In particular, when we exposed an abdominal vessel by an 820-nm-wavelength laser, increasing the energy fluence from  $60 \text{ mJ/cm}^2$  to  $600 \text{ J/cm}^2$  led to an increase of PA contrast of the CTCs above the RBC background by ~6 times [30]. This phenomenon was associated with laser-induced nanobubbles around overheated strongly absorbing melanin nanoclusters in melanoma cells, which served as a nonlinear PA signal amplifier compared to linear PA signals from RBCs with homogenous hemoglobin distribution (i.e., with no nanobubble formation). On the other hand, the rate of CTCs have been gradually decreased from 12 to 1–2 CTC/min over a 1 h monitoring period (Fig. 4B). This effect was also associated with the generation of nanobubbles as a melanoma cell killer [30,59]. Nevertheless, later the CTC rate gradually increased to almost levels initially detected, indicating the appearance of new CTCs from the primary tumor. These data demonstrate a great potential of PAFC for guiding blood purging *in vivo* by periodically exposing the blood vessels to the laser. Further study could determine whether this new treatment is effective enough to be used alone, or whether it should be used in combination with chemo- or radiation therapy.

Using advanced PAFC to monitor CTCs in mice models with different melanoma tumors, we discovered the early appearance of CTCs during the first week of tumor development, but the CTC rate fluctuated and completely disappeared at the late stage of tumor development in 30–40% of the cases, thus demonstrating a low cor-

relation of CTC counts with tumor size. This phenomenon can be related either to the high heterogeneity of local tumor environments, a poor blood network in large tumors, or the development of less metastatically-active cells both in the primary tumor and in distant metastasis. This important observation requires further study with a specific focus on the role of CTC count as a marker of tumor progression and metastasis development. *In vivo* flow cytometry could be the key tool to address this important issue.

### 3.3. Multiplex molecular targeting and magnetic enrichment of breast CTCs

A combination of conventional flow cytometry with separation, isolation and enrichment methods revolutionized diagnosis and therapy of diseases [60]. Various physical cell properties, including size, motility, electrical dipole moments, as well as optical and magnetic qualities have been exploited for this purpose. In particular, specific cells (e.g., CTC or bacteria) or biomolecules (e.g., proteins, and DNA) in biological fluids such as blood, urine, or cerebrospinal liquids, were labeled using magnetic microbeads and MNPs and then they are separated and enriched from the sample flow by a magnetic field [60]. To date, these techniques are used only in *ex vivo*, while the applications *in vivo* are limited by static objects only. We demonstrated for the first time, the application of magnetic enrichment of CTCs directly in bloodstream (Fig. 5A–D) [28].

In light of the limited expression of most cancer markers, we applied a multiplex targeting strategy for the detection of CTCs. Specifically, we used duplex molecular targeting of the MDA-MB-231 human breast cancer cells, which is positive for urokinase protease-activated receptors (uPAR) and folate receptors (FRs). It has been demonstrated that 60–90% of breast cancers express uPAR ( $\sim 10^5$  receptors/cell vs. 2,500 receptors/cells for normal human epithelial cells) [28] and 80–90% express FRs [51]. Advanced golden carbon nanotubes (GNTs) (Fig. 5C) having an absorption maximum at 900 nm and a minimum at 639 nm (Fig. 5D) were coated with polyethylene glycol (PEG) and conjugated with folate. As the second NPs, 10-nm MNPs coated with PEG and amphiphilic tri-block polymers were conjugated with the amino-terminal fragment (ATF) of a urokinase plasminogen activator (uPA), which is a high-affinity, natural ligand for uPAR (Fig. 5B). MNPs have a absorption in the broad NIR range; nevertheless, the absorption spectrum is different from that of GNTs (Fig. 5D). PA and PT scanning cytometry [22,27,30], in combination with fluorescent imaging, revealed that this NP cocktail exhibited the best targeting efficiency (96%) *in vitro*, in a blood sample spiked with rare tumor cells and a negligible level (~6%) of background PA signals from unbound or nonspecifically bound NPs. At weeks 2, 3 and 4 of tumor development in mouse models (Fig. 6A), a cocktail of the conjugated NPs were injected intravenously into the circulation. PA monitoring of targeted CTCs at 20 min after injection (to allow clearance of most unbound NPs) showed that the ratio of the numbers of CTCs in the ear of the mouse compared to those in abdominal vessels (CTCs/min) increased from  $(0.9 + 0.3)/(6 + 2.1)$  at week 2 to  $(7.2 + 0.3)/(26 + 2.1)$  at week 3 and to  $(15.1 + 2.7)/(47 + 6.4)$  at week 4 (Fig. 6B). These data approximately correlated with the stage of the tumor progression. Attaching a magnet with a field strength of 0.39 Tesla led to immediate increases in both PA signal amplitude and rate, and changed the character of the PA signal from infrequent flashes to a continuous increase of permanent PA signals up to 88-fold within 1.5 h, indicating successful magnetic CTC capturing [28]. Applying this method to clinical use, the patients may potentially carry a magnet attached to selected peripheral vessels (e.g., in wrist area) for trapping of CTCs, followed by a quick PA detection of the trapped CTCs, and, if necessary, local PT treatment or removal of CTCs by using syringe-based systems for further molecular analysis.

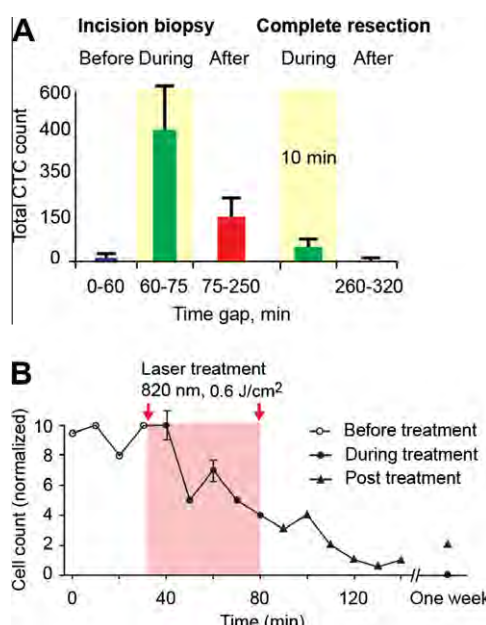
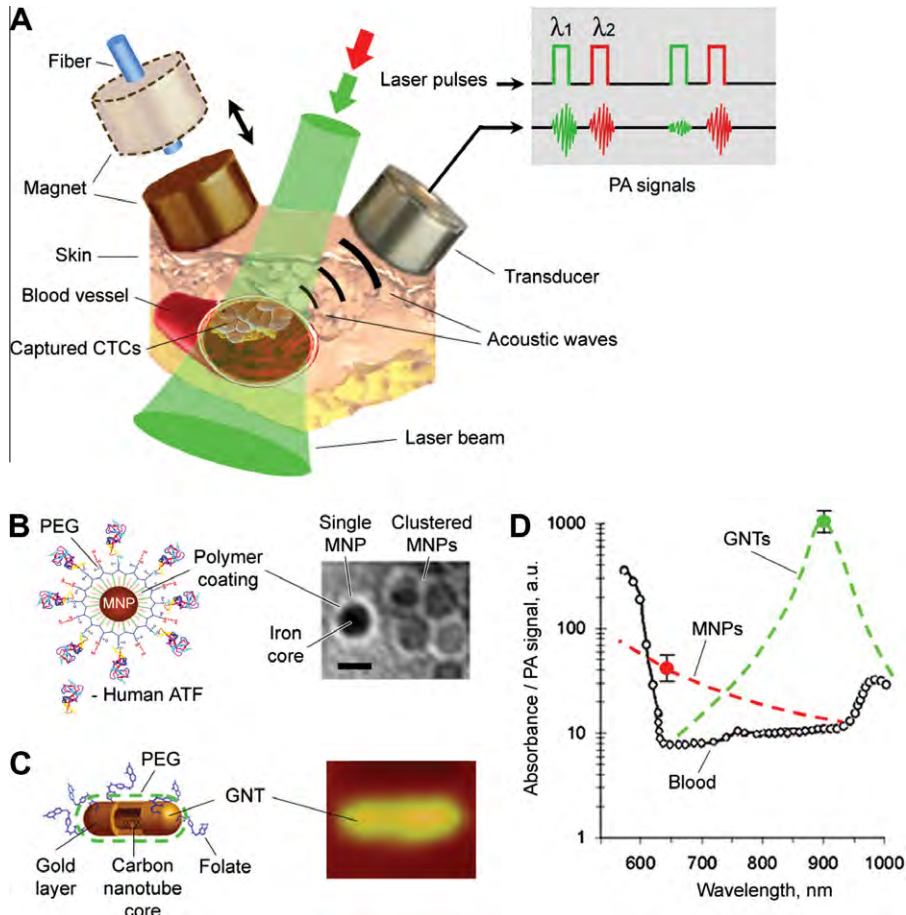


Fig. 4. CTC count as a marker of therapy efficacy. (A) Effect of incisional biopsy and complete resection on CTC dynamics. (B) PA guidance of PT therapy of CTCs.



**Fig. 5.** *In vivo* magnetic enrichment and two-color PA detection of breast CTCs. (A) Schematic of setup. The laser beam is delivered either close to the external magnet or through a hole in the magnet using a fiber-based delivery system. (B) Schematic (left) and transmission electron microscopy image (right) of MNPs, each with a 10-nm core, a thin (2 nm) layer of amphiphilic triblock copolymers modified with short polyethylene glycol (PEG) chains and the amino-terminal fragment (ATF) of the urokinase plasminogen activator. Scale bar, 10 nm. (C) Schematic (left) and topographic atomic force microscopy image (right) of a GNT ( $12 \times 98$  nm) coated with PEG and folic acid. (D) PA spectra of 70- $\mu\text{m}$  veins in the mouse ear (open circles). Absorption spectra of magnetic nanoparticles (MNPs) and GNTs (dashed red and green curves) are normalized to PA signals from CTCs labeled with MNPs (filled red circle) and GNTs (filled green circle).

### 3.4. Flow cytometry platform for detection and killing of circulating cancer stem cells

It is believed that a small population of cancer cells (3–5%), called tumor-initiating or cancer stem cells, may be a cornerstone of metastatic initiation and progression due to their extensive self-renewal capacity, tumorigenicity and multipotentiality associated with drug and irradiation resistance [61]. Thus, these cells could be a novel and crucial target for diagnosis and therapy. However, little is known about subpopulations of these cells that can enter the circulation and migrate to distant sites, forming metastases. Because an extremely low concentration of stem CTCs are expected in the circulation, we proposed to use high sensitivity PAFC for detection of stem CTCs [31]. Specifically, *in vivo* targeting of breast CTCs with a stem-like phenotype, which are naturally shed from the parent tumor in mouse models, were performed with functionalized gold-based GNTs and MNPs. Data *in vivo* were verified *in vitro* using PA and PT scanning cytometry. We discovered that magnetic-induced clustering of MNPs in individual cancer cells (MDA-MB-231) led to significant (10-fold) amplification of PT and PA signals. We also demonstrated the proof-of-concept *in vitro* that PA diagnosis can be integrated with targeted PT eradication of individual stem CTCs.

In the preliminary study *in vivo*, GNTs and MNPs conjugated with folic acid and antibodies to CD44 were selected for the detection of stem-like CTCs. For identification of bulk CTCs, we used

markers described in Section 3.3. At week 4 of the tumor inoculation, when the metastatic disease was well recognized by metastasis in the distant organs (e.g., liver), MNPs-Folate and GNT-CD44 were separately injected into a vein in the mouse tail. To allow effective labeling of CTCs in the bloodstream and washing out of unbound NPs, PA monitoring of blood vessels began 20 min after injection. As expected, the flashing readable PA signals above the PA background of blood were detected within 2 h of the observation. This indicated approximately 10–15% of stem-like CTCs were among the bulk CTCs (Fig. 6C). To the best of our knowledge, we demonstrated for the first time, that the multifunctional PAFC-PT-nanotechnology-based-platform has the potential for ultrasensitive PA molecular detection of stem CTCs *in vivo*. The interpretation of the obtained data at the current stage requires further studies, which are now in progress in our laboratory. It includes exploring the role of the folate receptor and adding CD24 and CD45 markers to increase detection and specificity of stem-like CTCs and excludes possible false positive signals from leukocytes, respectively.

### 3.5. Detection of disseminated tumor cells in lymph flow and sentinel lymph nodes

The fact that common pathways for the dissemination of cancer cells from the primary tumor are lymph and blood vessels, and that tumor cells may pass from one system to another through numer-

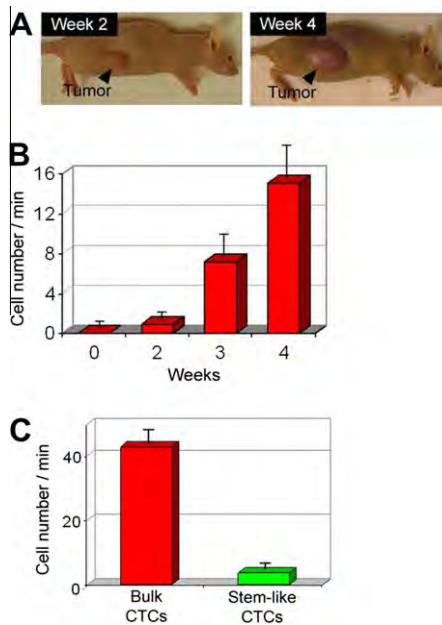


**Fig. 6.** PA detection of bulk and stem-like breast CTCs in tumor-bearing mice. (A) The size of the primary breast cancer xenografts at different stages of tumor development. (B) The average rate of bulk CTCs in the mouse ear vein over a period of 1–4 weeks. (C) Average rate of CTCs associated with bulk Folate+/uPAR + CTCs and Folate-CD44 + stem-like CTCs in 200  $\mu$ m in abdominal skin blood vessels in the mouse model of breast tumor (at week 4).

ous anatomical interconnections between lymph vessels, sentinel lymph nodes (SLNs) and the blood circulatory system has been well-known for many years (see [62] and references there). Nevertheless, until now, so-called disseminated tumor cells (DTCs) and CTCs in lymph and blood systems, respectively, have been studied separately. Moreover, most efforts have been focused on the examination of CTCs in the blood system, while studies of the metastasis process in lymphatics were paid much less attention to.

Compared with the blood vasculature, lymph vessels are colorless, with a relatively low pressure and low concentrations of cells. As a result, lymph sampling is impractical due to its yields of only a few microliters at a time and long-term cannulation. Recently, we integrated *in vivo* blood and lymph PAFC, PA lymphography, and PA scanning cytometry (study of nonmoving cells), and demonstrated a potential of this platform for real-time, *in vivo* quantitative monitoring of CTCs in blood, DTCs in prenodal lymphatics, and SLNs, using intrinsic melanin or functionalized NPs as PA contrast agents in melanoma and breast tumor bearing mice models, respectively. It allowed us to define cross-correlations between lymph DTCs, blood CTCs, the size of the primary tumor, and nodal and distant metastases (Table 1). Specifically, in the preclinical mouse melanoma model, we revealed that early metastatic cells in latent metastatic disease (4–7 days after tumor inoculation) are equally disseminated through blood and lymph pathways. However, in a few cases, metastatic cells appeared in lymph vessels at week 1 without any cells detected in the blood vessels and vice versa, suggesting an individualized character of tumor cell dissemination. During week 2, a 3.5-fold primary tumor growth was accompanied by a 10-fold increase of DTC count in the lymph flow and by a 6.5-fold increase in the number of PA signals in SLNs as a sign of metastasis development (Fig. 7), while much less CTCs were observed in the blood flow. PAFC demonstrated an unprecedented sensitivity threshold for *in vivo* lymph testing, as one melanoma CTC in the background of  $10^6$  WBCs could be identified [20]. The association between DTC count and SLN metastasis progression supports lymphatic DTCs as a novel prognostic marker of metastasis.

In addition, we demonstrated PAFC-guided, PT purging of melanoma and breast cancer micrometastasis in SLNs mimicked by direct injection of cancer cells in SLNs. Targeted detection of breast cancer metastasis in the SLNs of the mouse models was performed by injection of the GNT-folate conjugates in the mouse ear. At five minutes after the injection, strong PA signals above the background, with a contrast of 10–15 appeared in the SLN due to the transportation of the NPs through the lymph vessels to the SLN and the targeting micrometastasis in the SLNs. Subsequent application of the therapeutic laser pulses with enhanced energy fluence led to a decrease of these initially PA strong signals to a background level, which indicated laser-induced destruction of tumor cells. On the contrary, when the experiment was repeated with unconjugated GNTs, low PA signals with a contrast of ~3 above the background were observed, suggesting random distribution of GNTs in the SLN volume. To verify these data, *ex vivo* experiments mimicking the lymph node micrometastasis were carried out using conjugated GNT-folate and fluorescent dye for visualization of the tumor cells [22]. These results support the feasibility of the theranostic PAFC–PT platform for the *in vivo* detection and killing of metastatic cells in SLNs exploring NP clustering in micrometastasis accompanied by red-shift effect and PA signal amplitude enhancement as an indicator of molecular targeting [59]. This platform, in combination with microarrays, might provide assessments of the biological properties of lymph DTCs (e.g., molecular profiles and viability) compared to those in the primary tumor, regional and distant metastasis, and blood CTCs during metastasis progression, with a focus on identifying the tumor initiating cells among the bulk lymph DTCs. The expanded knowledge of lymphatic-related metastasis may catalyze a paradigm shift in the diagnostic clinical oncology, from conventional assessment of early metastasis in SLNs toward lymph DTC testing. Taking into account the safe nature of the proposed *in vivo* lymph cancer tests as supplementary (or in some cases as alternative) to conventional blood tests, we anticipate a quick translation of this technology for use in humans.

### 3.6. *In vivo* photoacoustic detection of circulating tumor cells in cerebrospinal fluid

The dissemination of cancer (e.g., leukemia, lymphoma, breast cancer, and melanoma) into the central nervous system either through hematogenous spread, direct release from the tumor itself, or by migration along perineural or perivascular spaces is a serious medical problem leading to neurological symptoms (e.g., neoplastic meningitis) and rapid mortality [63]. In particular, the presence of tumor cells in cerebrospinal fluid (CSF) may serve as a marker of disease progression and early-stage brain metastasis in breast cancer. The CSF is a colorless body fluid with a total volume of 135–150 mL in adults, which circulates through the ventricular system around and inside the brain and the spinal cord. The CSF flow has pulsatile “forward–backward” characteristics that correlate with cardiac cycles. Forward velocity in the spinal canal ranges from 10 mm/s in the craniocervical junction to 1 mm/s in the lumbar part of the canal; the velocity of backward flow is approximately two times slower than that of forward flow. The CSF function is bathing the central nervous system, and bridging the vascular and lymphatic systems. The current tools available for detecting CTC spread into the CSF such as cytology, *in vitro* flow cytometry and others [63,64] are limited by small sample volume and suffer from a lack of sensitivity, leading to delays in treatment. Improved detection of CSF malignancy is a clinical imperative.

We propose that many of these problems could be resolved by increasing the sensitivity and specificity of CSF examination through *in vivo* analysis of a relatively large volume of circulating CSF using noninvasive PAFC, and functionalized NPs as PA contrast

**Table 1**

Correlation between primary tumor size, metastasis in SLN and number of tumor cells in lymph- and blood flow.

	Tumor size (mm <sup>2</sup> )	Rate of lymph CTCs (cell/min)	Rate of blood CTCs (cell/min)	Number of PA signals associated with metastasis in SLNs	Histology
1 week	1.0 ± 0.2	0.26 ± 0.05	0.85 ± 0.03	493	No
2 weeks	3.6 ± 0.5	2.13 ± 0.30	1.07 ± 0.05	3,188	Yes

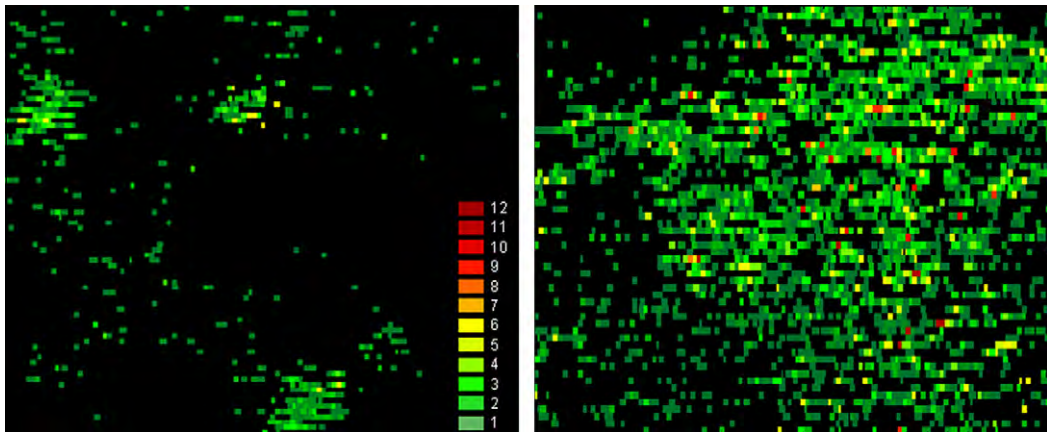


**Fig. 7.** PA scanning cytometry of melanoma metastasis in the sentinel lymph node (1.6 × 3 mm) at a single cancer cell level using the tumor-bearing mouse model at weeks one (left) and two (right) of tumor development. Red pseudo-color peaks indicate PA signals with maximum amplitudes. Each single spot is associated with single metastatic cells.

agents. This approach has not been attempted previously. In our study, gold nanorods (GNRs)-folate conjugates with maximum absorption near 670 nm were injected in primary tumor of tumor-bearing mice 10 weeks after tumor inoculation. The next day irradiation through a 300-μm fiber of CSF in the cisterna magna of nude mice with a nanosecond laser pulse at 671 nm revealed rare PA signals with a rate of a few signals per hour associated with targeted breast tumor cells flowing though the CSF. Using the methodology described in Sections 3.3–3.5, the assessment of the brain confirmed the presence of micrometastasis as a potential source of tumor cells in the CSF. The estimated sensitivity was approximately a few CTCs among a million leukocytes over a four-hour period. Our approach may provide a semi-automated PA molecular analysis that vastly improves the sensitivity, reliability, objectivity, and accuracy of detecting tumor cells in CSF compared to CSF cytology. Due to high depth assessment (up to few cm), fiber-based PAFC could be applied to different sites of the spinal canal (e.g., cervical, lumbar) and ventricles. If clinically successful, this tool may provide a tremendous leap forward in a previously unexplored scientific area of *in vivo* CSF testing including cell trafficking and counting, cell-to-cell interactions in the CSF, and the route of CSF circulation, especially in the terminal end of the spinal canal.

#### 4. Detection and killing of circulating bacterial cells

Despite major advances in medicine over the last decade, microbiologically-based diseases continue to present enormous global health problems, especially due to the appearance of multi-drug-resistant bacteria strains. The critical steps in the development of bacterial infections include their penetration into the blood system, interactions with blood cells flowing in the circulatory system, or with endothelial cells, and further translocations in the host organisms. Unfortunately, little is known about circulating bacterial cell (CBC) kinetics in the blood pool. This includes their clearance and adherence rates, which might be very important for understanding the transition from the bacteremic stage to the tissue invasive stage and development of an effective ther-

apy. Previously, we demonstrated the capability of the PAFC-PT platform for *in vitro* detection and killing of *S. aureus* and *E. coli* labeled with gold NPs and carbon nanotubes (CNTs) [15,65,66]. Recently, we extended this platform for *in vivo* magnetic enrichment, multiplex PA detection and PT eradication of circulating *S. aureus* (Fig. 8A) using the methodology developed for CTCs [28]. Bacteria were targeted directly in the bloodstream through intravenous injection of silica-coated MNPs (siMNP) and GNRs (with a maximum absorption near 820 nm) functionalized with antibodies specific for *S. aureus* surface protein A and lipoprotein, respectively. These are both highly expressed in *S. aureus* and absent in mammalian cells. After successful two-color PA detection of targeted CBCs at low energy fluence (50 mJ/cm<sup>2</sup>) of lasers at 671 and 820 nm, mice were subjects of PT therapy by a one-hour laser exposure of a 300-μm abdominal blood vessel with a laser fluence of 800 mJ/cm<sup>2</sup> at 820 nm, coinciding with an absorption spectra of GNRs. PT nanotherapy led to a significant decrease in the PA signal rate (Fig. 8B, red curve) compared to the control group (blue curve) at a laser fluence shown to be safe for blood cells. To confirm this therapeutic effect, mice were euthanized, and the blood was examined for the presence of viable bacteria. Blood from the control and PA-diagnostic groups showed similar bacterial growth, while the number of bacteria from the PT therapeutic group was reduced by 10-fold.

Compared to existing diagnostic and therapeutic approaches, the PAFC-PT nano-theranostic platform may offer many advantages: (1) ultra-high sensitivity (0.5 CFU/mL); (2) physical, PT-based destruction of bacteria, thus retaining its therapeutic efficacy irrespective of the antibiotic resistance status of the offending bacteria; (3) integration of multiplex PA molecular detection and PT targeted elimination of CBCs with real-time PA monitoring of therapeutic efficacy; and (4) high spectral specificity based on distinct spectral properties of NPs [41]. Because some gold NPs were already approved for pilot studies on humans [28], and the clinical potential and safety of PA technology has been successfully demonstrated in pilot trials [46–49], early laser-based detection and treatment of CBCs could be feasible in a 0.5–1.5 mm hand vein at 1–2 mm depths, which is within the well-documented capacity

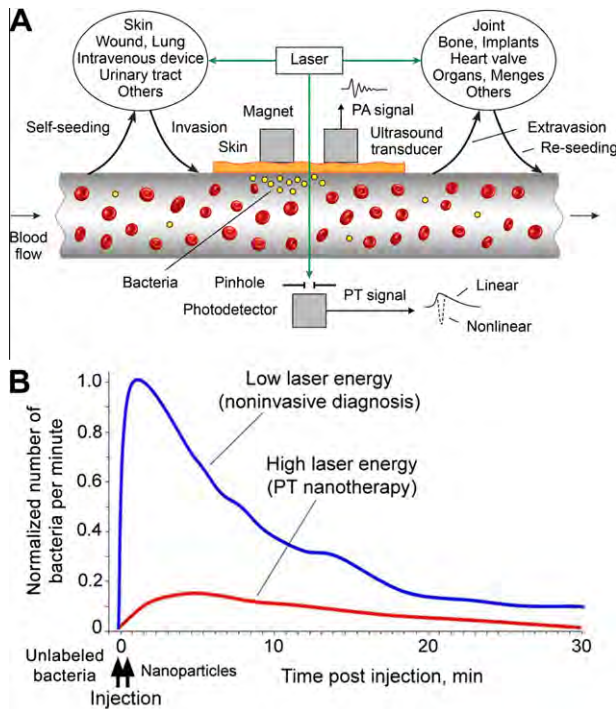


**Fig. 8.** PA molecular diagnosis and photothermal-targeted eradication of circulating *S. aureus* in the blood of the mouse model with real-time PA monitoring of PT nanotherapeutic efficacy. (A) Schematic. (B) Experimental data. This figure is from a paper Galanzha et al. [73].

of the PA technology to assess much deeper (5–7 cm) and larger (1 cm) human blood vessels [46].

## 5. Detection of circulating clots using negative and positive photoacoustic contrasts

When a blood vessel is injured, the normal physiological response of the body is clot (thrombus) formation to prevent blood loss. Alternatively, even without vessel's injury, pathological condition called thromboembolism may lead to formation of circulating blood clots (CBCs) that eventually can plug the vessels of different locations, in particular, in the veins of extremities (venous thromboembolism), lungs (pulmonary embolism), brain (embolic stroke), heart (myocardial infarction), kidney, or gastrointestinal tract. Thromboembolism is a significant cause of morbidity and mortality, especially in adults. Despite clear medical significance of CBCs little progress has been made in the development of methods for real-time detection and identification of CBCs. Many CBCs remain undetectable, unless they result in clinical phenomena. The majority of patients die because of a failure in diagnosis rather than inadequate therapy. Commonly used *ex vivo* methods of detecting clots are time-consuming, low sensitive due to small volume blood samples, and are limited by discrete time-point sampling with difficult access to clinically relevant sites. Most *in vivo* methods are only able to detect fixed or slowly moving large clots. A pulse Doppler ultrasound is a promising technique for the detection of CBCs, but this technique cannot assess clot composition, detect small clots, and may be affected by artifacts [36 and refs. there].

To overcome these limitations, we proposed an *in vivo* PAFC for real-time detection of clots of different compositions (Fig. 2A) [36] using a combination of positive and negative contrast modes. Laser irradiation of blood vessels in normal vessels creates a constant PA background determined by the absorption of RBCs randomly distributed in the irradiated volume. Depending on the size of the ves-

sels, hematocrit (Ht), and PAFC spatial resolution, the number of RBCs in the detected volume can vary from one or a few RBCs in the capillary to thousands in larger vessels. When a RBC-rich red clot passes through the irradiated blood volume, a transient increase in the local absorption which is associated with a high concentration of hemoglobin (Hb), results in a sharp positive PA peak (Fig. 2C, left). Red clots can be detected when they have a higher local absorption than the normal RBC background in the detected volume. For example, five RBCs in a red clot have a volume of ~450 fL (corpuscular volume of a single RBC is 90 fL [35]) with a total Hb amount of 150 pg (~30 pg of Hb per one RBC), while the same volume of whole blood with a Ht of 45% contains just two RBCs with 60 pg of Hb. Thus, the expected ratio of PA signals from even a small RBC number in the clot to blood background is 2.5, which is sufficient for the detection of RBC aggregates. When a weakly-absorbing, platelet rich white clot (Fig. 2A) passes through the laser-irradiated vessel volume, a transient decrease in the local absorption results in a sharp negative PA signal (Fig. 2C, middle). A mixed clot with both RBC-rich (i.e., high-absorbing) and platelet-rich (i.e., low-absorbing) local zones will produce a pattern of positive and negative PA signals (Fig. 2C, right).

This phenomenological model was first verified *in vitro* using human blood, then *in vivo* in animal models by injection of well-established agents for the creation of circulating clots, and eventually in preclinical studies using the mouse model of myocardial infarction [36]. The readable transient PA signals were observed with different patterns of negative, positive, and combined contrasts (Fig. 9A) associated with white, red, and mixed clots, respectively, compared to no signals in control normal mice. The concentration and size of clots were measured with a threshold of a few clots in the entire circulation (i.e., 1–3 clots/mL in mice) with the size as low as 20 μm that is unachievable with the existing techniques. This PAFC-based diagnostic platform can be used in real-time defining risk factors for cardiovascular diseases, as well as for the prognosis and potential prevention of stroke by using a well-timed therapy or for a clot counting as a marker of therapy efficacy.

It is believed that clots are also common complications of infection, inflammation, cancer, surgery, radiation and coronary artery bypass graft (CABG resulting in heart attacks and strokes (e.g., [67,68]). However, due to restrictions of existing assays, little data has been available of CBC detection during these complications. Fig. 9B illustrates PA detection of clots during melanoma development on the melanoma-bearing mouse model. PAFC allowed to identify clots traveling separately or together with melanoma cells through temporal coincidence of CTC-related positive peaks and negative peaks associated with white clots, respectively. PA data supports the hypothesis of platelets aggregating around CTCs. We also observed that a surgery modeled by surgical removal of tissue or local incision led to the immediate appearance of circulating white clots associated likely with aggregated platelets (Fig. 9C). Thus, the PAFC-based diagnostic platform can provide insights on clot formation occurring in different diseases, pathological states or therapeutic interventions. This platform has a potential for real-time defining of risk factors for cardiovascular diseases, for prognosis and potentially prevention of stroke by well-timed therapy, and estimation of therapy efficacy through PA clot counting.

## 6. In vivo fluctuation flow cytometry for dynamic monitoring of red blood cell aggregation and sickle cells

Alterations in blood rheology (hemorheology) are important for the early diagnosis, prognosis, and prevention of many diseases including sickle cell anemia, thromboembolism, trauma, inflammation, diabetes, heart attack, stroke and malignancies [35]. However,

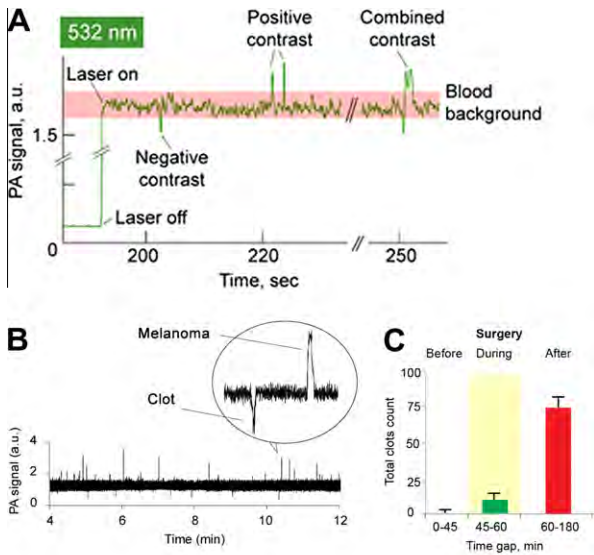


**Fig. 9.** Label-free, real-time, PA detection of white, red, and mixed clots in the ear vessel of the mouse model in various disease states. (A) Monitoring of clots in the myocardial infarction animal model at a laser wavelength of 532 nm. The laser pulse repetition rate is 10 kHz. (B) Detection of clot formation in the blood vessels of the melanoma-bearing mouse model (at week 4). (C) Monitoring of clot formation during and after surgery modeled by small skin incision.

real-time *in vivo* assessment of multiple hemorheological parameters over long periods of time has not been developed. PAFC alone, or in combination with PT techniques has the capability of label-free, dynamic monitoring of hemorheological parameters *in vivo* including RBC aggregation, shape and deformability, hemoglobin distribution, individual cell velocity, shear rate and viscosity [35]. The detection of RBC aggregation and sickle cells can be performed by so-called *in vivo* fluctuation PAFC. Irradiation of blood vessels created a different PA background pattern determined by vessel diameter and RBC properties (Fig. 2A). The average level of this background is proportional to the number of RBCs in the irradiated volume, thus allowing the estimation of the Ht after the corresponding calibration procedures taking into account blood oxygenation, Hb concentration, and vessel size [35]. The fluctuation in the background absorption is associated with changes in the number of RBCs in the irradiated volume. This fluctuation increases as the vascular diameter decreases. Ultimately, in a capillary with single-file RBC flow, single flash PA signals appear when individual RBCs sequentially pass through the irradiated volume (Fig. 2D, left trace). In arterioles and venules in which several RBCs appear simultaneously in the irradiated volume, the background level increases, but its fluctuation decreases. In large vessels containing hundreds or thousands of RBCs in the irradiated volume, the background continues to rise and fluctuations are minimized and are ultimately determined by laser pulse energy instability. The dilution of blood with a physiological solution leads to a decrease in the background level that can be used to calculate Ht [35].

When many small RBC aggregates or a single large RBC aggregate passes through the irradiated volume, it results in an increase in PA signal fluctuations (Fig. 2D, third trace) and/or transient strong PA peaks (Fig. 2D, fourth trace), respectively. The increase of local absorption in two- and three-dimensional aggregates leads to a significant increase in PA signal fluctuations as a marker of either normal formation of reversible (physiological) rouleaux or irreversible (pathological) clumps of RBCs. These data were obtained in the mouse model by intravenous injection of Dextran500 (a well known agent for activation RBC aggregation) [35]. In 40 μm ear blood vessels a few minutes after injection the PA signal ampli-

tude fluctuations increased on 10–30% as compared to control blood vessels, and occasionally large PA signal peaks were observed (Fig. 2D, fourth trace). These data suggest that PA signal fluctuations and PA spectral analysis can be used to monitor RBC aggregation. In particular, analogous to large CNT clusters [33] and clots [36], we observed that the shape of individual PA signals from relatively large RBC aggregates is changed and accompanied by a shift of the central frequency in individual PA signal spectra to that of a lower frequency. Therefore, analysis of spectra of individual PA signals (Fig. 2A, top right) as well as the amplitude and width of averaged peaks in PA signal traces (Fig. 2C) can provide information of the average aggregate size, and potentially its two- and three-dimensional spatial configuration.

A similar approach can be used to study sickle cell disease (or sickle-cell anemia) associated with a genetic modification of RBCs which result in the production of abnormal hemoglobin, HbS instead of hemoglobin HbA. This point mutation exerts its effects by causing precipitation and polymerization of the deoxygenated HbS, resulting in the sickling of RBCs. The elongated-shaped, rigid, sickle cells lack deformability, occlude the microvasculature, and lead to tissue infarctions, which manifest as a painful sickle cell crises. Optical and other methods have helped to develop an explanation for the sickle crises caused by cell adhesion to the vascular endothelium followed by “log-jamming” of the rigid sickle cells, which has stimulated much research into new treatments. However, characterization of sickle cell properties at the single cell level has been poorly explored. We believe that fluctuation PAFC integrated with PT techniques could benefit sickle cell disease research by focusing on *in vivo* study of the behavior of sickle cells in a real biological environment.

Using a genetically modified mouse model of human sickle cell disease, high-sensitivity PT imaging demonstrated the ability to distinguish sickle RBCs on the basis of their specific shape and intracellular PT patterns [35]. Sickled RBCs had a more profound spatial heterogeneity than normal RBCs which may be associated with increased clustering of HbS compared to HbA. Comparison of PA, PT and the conventional absorption spectra of normal and sickle RBCs demonstrated a slight difference in the spectral range of 590–660 nm which makes spectral identification difficult.

However, both PT and PA signal amplitudes from normal RBCs were 2–7-fold higher than the amplitudes from sickle RBCs. This difference in amplitudes was associated with the specific cell shape and Hb concentration (Fig. 10). As a result, the assessment with PAFC of similar size the ear blood microvessels in normal and genetically modified mice revealed lower PA blood background and more profound PA signal amplitude fluctuations in mice with sickle cells as compared to normal mice [35]. The level of these differences depended on the number of abnormal cells in circulation. Thus, *in vivo* fluctuation PAFC has the capability for real-time monitoring of RBC aggregation, sickle disease status and potentially the response to the corresponding therapy.

## 7. *In vivo* photoacoustic bone flow cytometry

We determined that even after significant attention of laser radiation in the bone tissue, the laser energy is still enough to generate readable PA signals from strongly absorbing objects inside bones using focused ultrasound transducers (Fig. 11A). Indeed, intravenous injection of carbon nanotubes (CNTs) led to the appearance of PA signal traces from the mouse tibia [39]. To exclude possible PA background signals from CNTs circulating in blood vessels between fiber used for delivery laser radiation and bones, the fiber was gently attached to the skin in an area with no visible vessels. A time-resolved detection system was used to select PA signals coming with a time delay from relatively deep bone compared to the depth of superficial blood vessels. Scanning of the laser beam along

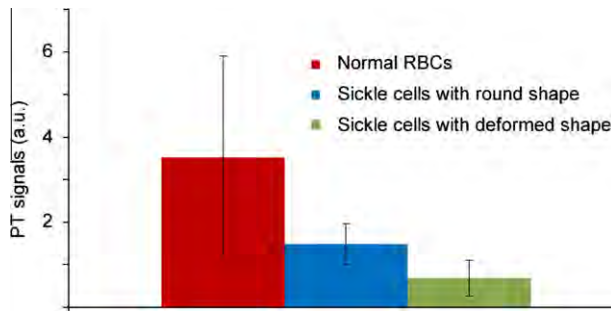


**Fig. 10.** Average PT signal amplitudes from normal and sickle RBCs of different shapes at a laser wavelength of 532 nm.

the bone revealed rare stationary PA signals associated with the accumulated CNTs in bone. Similar results were obtained for breast cancer cells (MDA-MD-321-GFP) targeted by GNRs with a maximum absorption at 670 nm. The GNRs conjugated with folate were intravenously injected in the tumor-bearing mouse model at week 4 after tumor inoculation. We observed rare PA signals from the tibia irradiated using a high-pulse-rate laser (10 kHz) at 671 nm (Fig. 11B). These signals were associated with individually targeted CTCs. PA scanning cytometry revealed also rare stationary PA signals associated with CTCs captured in bone. This technique, after further optimization, has the potential for early and painless diagnosis of bone cancer metastasis (noninvasive bone marrow biopsy) or infection through the administration of strongly absorbing NPs functionalized to identify specific cancer cells or infection markers. The identification of targeted cells can be performed in analogy to detection of micrometastasis in SLNs (Section 3.5). In particular, healthy bones produce low-level background PA signals because low concentrations of NPs are randomly and nonspecifically distributed in the bone tissue as compared to a high local concentration of NPs that is found in cells causing bone metastasis with possible red-shift effect in clustered plasmonic NPs [59].

### 8. In vivo photoacoustic plant flow cytometry

Understanding the nature of interactions between engineered nanomaterials and plants is very important to comprehend the impact of nanotechnology on the environment and agriculture. We demonstrated that an advanced imaging platform integrating genetic, PT and PA scanning methods can provide the study of NP–plant interactions in stationary condition at the single NP levels [69]. We developed also PAFC for the real-time noninvasive monitoring of nanomaterial transport in xylem and phloem of plant vascular systems [34]. The PA signals were detected in the plant using

fiber to deliver laser radiation at 1064 nm (with minimum background absorption in plant tissue) and an ultrasound transducer attached to the plant surface. In particular, PAFC was able to monitor quantum dot–carbon nanotube (QD–CNT) conjugate uptake by the roots of the plants and trace its spreading through stem to leaves in a tomato plant. PA signals in the leaf mid-vein (Fig. 12A) were observed at ~5 min after the QD–CNTs were added to the water surrounding the roots (Fig. 12B). Taking into account the average distance between the roots and the detection point (5 cm), and some delay in NP uptake, the average linear flow velocity in the stem can be estimated as 0.2 mm/s. As xylem bundles are arranged symmetrically around the stem center, a fiber tip can easily be positioned against any part of the stem. In the stem, which was thicker than the leaf, laser radiation at 1064 nm was more strongly absorbed by deep stem structures providing an increase in the PA background (3–4-fold). Nevertheless, PAFC allowed the assessment of the QD–CNT aggregates passing through the stem [34]. We believe that PAFC using both endogenous and exogenous contrast agents have a potential to open new avenues of *in vivo* study of the transport the nutrients, products of photosynthesis and metabolism, NPs, infectious agents, and other objects through the plant vasculature.

### 9. Photoacoustic time-of-flight velocity measurement of single cells and nanoparticles

Existing optical techniques for *in vivo* measurement of blood flow velocity are not quite applicable for determination of the velocity of individual cells or NPs. PAFC may solve this problem by using time-of-flight technique with single or multiple laser beams (Fig. 13A). In the one-beam scheme, an object crossing a laser beam created transient PA signals with a width  $t_L$ , defined as  $t_L \approx (D + d)/V_F$  where  $D$  is the diameter of object,  $d$  is the width of the linear laser beam, and  $V_F$  is the velocity of the object. Thus,  $V_F$  can be measured for objects and laser beam of known sizes. In the three-beam scheme, velocity of an object is determined by the time it takes for the object to travel between multiple laser beams (Fig. 13A, bottom). In this case, an object in flow produces multiple consequent trains of PA signals. Object velocity can be estimated by using the time intervals between the trains and the distances between the beams. This measurement is independent on the object size. These approaches were demonstrated *in vivo* using an animal (mouse) model by estimating velocity of GNRs, melanin NPs, RBCs, WBCs, and CTCs in the broad range of flow velocity from 0.1 mm/s to 20 cm/s [40]. In particular, monitoring of PA signal widths in mouse ear vessels from WBCs labeled with GNRs revealed the double maxima in peak-width histograms (Fig. 13B) associated with the fast moving portion of WBCs in central flow and slowly rolling WBCs. In general, the peak-width analysis in the time-of-flight mode provided important information on objects' velocities, cell aggregation manifested by the appearance of wider peaks with complex shapes, and on rolling effects that result in slower cell velocity. However, width histograms alone were not sufficient to distinguish a large aggregate of cells with high velocity and an individual rolling cell moving slowly because both would produce peaks of similar widths. We determined that these objects could be identified with a two-parameter plot representing PA peak amplitude and peak widths obtained from time-of-flight measurements. Fig. 13C illustrates verification of this approach for label-free detection of melanoma B16F10 cells. Three areas of interest were selected for this scatter plot: I) the area with the highest density of events, corresponding to fast-moving individual cells; II) aggregates of cells that were larger and had more melanin than individual cells; and III) peaks with PA signal too small to consider these objects as aggregates. Large peak widths in III suggested that these cells were moving more slowly than the other cells. Therefore, multi-

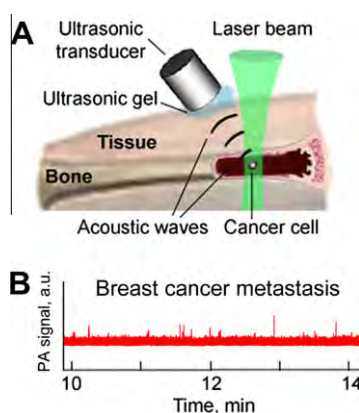


**Fig. 11.** *In vivo* PA bone flow cytometry. (A) Schematics. (B) Noninvasive *in vivo* molecular targeted detection of breast CTCs in mouse tibia.

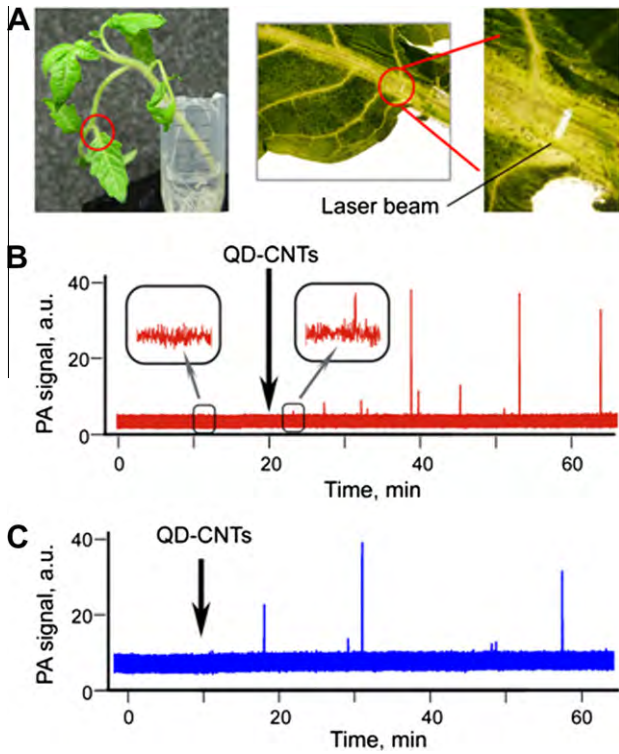


**Fig. 12.** *In vivo* PA plant flow cytometry of QD-CNTs in tomato vasculature. (A) Linear laser spot in a leaf mid-vein, close to petiole. The red lines denote the part of the plant used for monitoring. (B) The trace of PA signals recorded in the leaf mid-vein after QD-CNTs were introduced into the water tank. Insets demonstrate the enlarged parts of the control trace and the trace fragment with signals from QD-CNTs. (C) The trace of PA signals from QD-CNTs recorded in the stem of the tomato plant. Black arrows indicate the moment QD-CNTs were introduced into the water tank. The PA traces before the introduction of QD-CNTs represent control data. Laser parameters: wavelength: 1064 nm; pulse width: 10 ns; pulse repetition rate: 10 kHz; laser pulse energy: 20  $\mu$ J; laser spot size in sample:  $50 \times 150 \mu\text{m}$  (B) and  $100 \times 400 \mu\text{m}$  (C).

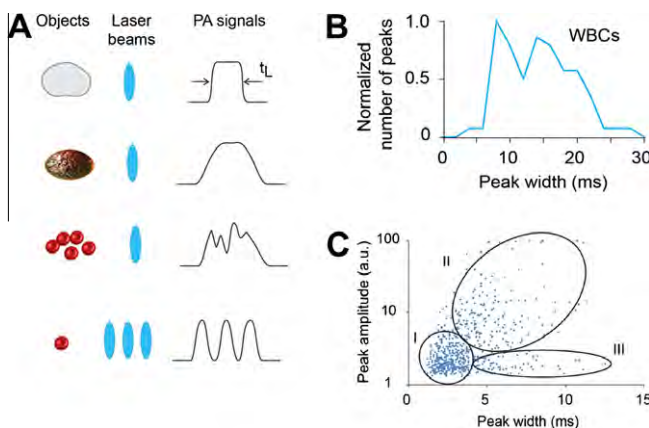


**Fig. 13.** *In vivo* PA time-of-flight velocity measurements of cells and nanoparticles. (A) Shapes of peaks in PA trace for particles of different sizes and various beam geometries. (B) Peak widths distributions in the WBCs in the mouse circulatory system targeted by GNRs with antibodies specific for the CD45 receptor. Laser parameters: wavelength: 820 nm, pulse width, 8 ns; pulse repetition rate: 10 kHz; laser pulse energy: 20  $\mu$ J. (C) Scatter plot of the height and width of peaks for label-free PA detection of circulating B16F10 cells in an arteriole of the mouse ear. Area I indicates signals from individual cells. Area II includes aggregates of several cells. Area III indicates possible ‘rolling’ cells.

parameter analysis of PA data may provide a criterion for distinguishing aggregates and individual rolling cells [40].

## 10. Pharmacokinetics of circulating contrast agents: NPs, dyes, liposomes, and microbubbles

The rapidly growing application of *in vivo* imaging modalities (e.g., optical, MRI, or ultrasound) and nanotechnology-based probes has placed new demands on monitoring the clearance rate of various contrast agents including NPs, drug carriers (e.g., liposomes), dyes and microbubbles. No clinically relevant method has been developed for rapid and ultrasensitive study of the pharmacokinetics of these agents including their clearance rate in different vessels. As most contrast agents have intrinsic optical absorption, PAFC is an almost ideal tool for real-time, label-free monitoring of their pharmacokinetics. We demonstrated PAFC's capability to monitor the circulation lifetime of NPs (e.g., GNRs, GNTs, MNPs), dyes (ICG, Methylene Blue [MB], and Trypan Blue [TB], Evans Blue, and Lymphazurine), microbubbles, normal blood cells, and CTCs (melanoma, breast cancer, squamous carcinoma, pancreatic cancer) using a laser with different wavelengths [11,15,28–30,33,38,40]. Circulating objects can be detected when PA signals from them are above the blood background associated preferentially with absorption of RBCs (Fig. 14A, top). After injection of contrast agents, PAFC provides two typical signal trace patterns (Fig. 14 middle and bottom) as an increase in the baseline level above blood backgrounds and strong fluctuations above the baseline. The first pattern is associated with homogenous random distribution of dye molecules, individual microbubbles, or NPs in the detection volume, while the second pattern is related with the presence of their aggregates with a more strong localized absorption. The clearance rate for most NPs depending on their protective layer properties, was in the range of 20–40 min, and in rare cases a few hours, while liposomes demonstrated a long term circulation of up to few days [42]. Some NPs demonstrated aggregation in blood flow especially during injection procedures. The described approach should be useful to the routine evaluation of the possible influence of the natural properties of NPs, the protective materials, and the coating procedures on NP clearing. The approach *in vivo* allows minimization of the animal number compared to *ex vivo* methods with periodical blood sampling.

Intravenous injection of normal blood cells and tumor cells labeled with various contrast agents and having different functional states revealed their different clearance rates (Fig. 14B): 1–3 min for necrotic cells, 5–15 min for apoptotic cells, 30–60 min for high metastatic tumor cells, one-three hours for cancer cells with lower metastatic activity, and several days for normal RBCs and WBCs, respectively. These data showed that the immune responses to abnormal and especially metastatic active cells were stronger than those to normal blood cells with labels.

PA monitoring of the clearance of dyes (ICG, MB, and TB) revealed increased dynamic PA signal fluctuations, which can be associated with interactions of dyes with circulating blood cells and plasma proteins [38]. The injection of TBs, which is broadly used for viability tests *in vitro*, led to rare notable PA signals *in vivo* which can be associated with dead cells uptaking TB directly in bloodstream. Thus, in addition to previously demonstrated detection of circulating normal and apoptotic cells [20], we demonstrated the potential of PAFC for detection of circulating rare dead cells. This is important for many applications including studies of cell metabolism in normal and pathological states or response to various therapies. PAFC can provide also detection of circulating microbubbles labeled with NPs (e.g., GNTs) as an ultrasound and PT contrast agents for imaging and thrombolysis of clots. Later was based on laser-induced transient microbubbles using stationary microbubbles labeled with NPs [39]. The typical clearance rate of microbubbles was in the range of 5–10 min.

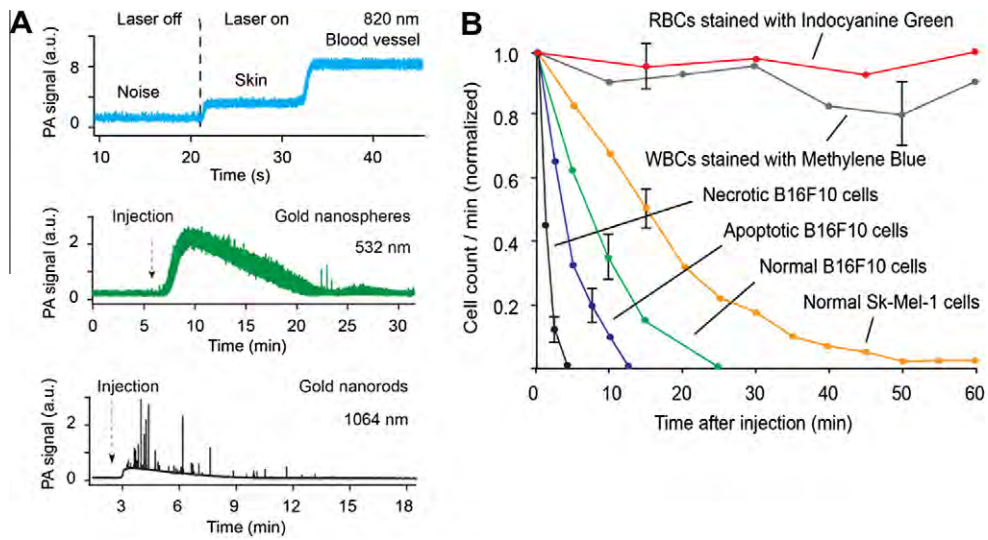


**Fig. 14.** PA monitoring of NP and cell clearance rates. (A) *In vivo* PA signal levels from the mouse ear vein and surrounding skin, compared to baseline noise, when the laser is off (top). Laser parameters: wavelength: 820 nm; fluence, 0.2 J/cm<sup>2</sup>; pulse rate: 10 kHz. PA monitoring of the clearance rate of 30-nm spherical gold NPs in a blood vessel of the mouse ear (middle). Laser parameters: 532 nm/cm<sup>2</sup>, 9 kHz. PA monitoring of GNR clearance in a blood vessel of the mouse ear (bottom). Laser parameters: 1064 nm, 0.1 J/cm<sup>2</sup>, 9 kHz. (B) PA monitoring of the clearance rates of melanoma cells at different functional states and normal blood cells labeled with contrast dyes.

## 11. Ultrasharp nonlinear photoacoustic and photothermal resonances for multicolor flow cytometry

PAFC's selectivity to identify many disease-associated markers can be limited by the wide NIR spectral band (80–200 nm in width) of available contrast agents, in particular plasmonic NPs. Using the nonlinear laser-NP interaction, we demonstrated the “sharpening” of the broad absorption spectra of gold NPs to a 1–5 nm in PA and PT spectra [41]. Specifically, a tuning of the laser wavelength toward the absorption NP center leads to increased absorbed energy, raising the temperature above the nanobubble-formation threshold accompanied by significant (1–2 orders of magnitude) nonlinear PA/PT signal amplification. As a result, spectrally dependent signal amplification will lead to the sharpening of PA/PT resonances near the center of the absorption peaks at optimal laser energy providing nanobubble formation in this center only (Fig. 15A). At higher laser energy nonlinear spectral resonances can be red- or blue shifted from absorption peaks. For example, Fig. 15B demonstrates an asymmetric red-shifted resonance in GNRs with a minimum width of 0.8 nm limited by laser spectral line width. Similar nonlinear effects using pump-probe excitation results in the creation of ultrasharp dips [41]. This technique made it possible to easily identify each GNR in a mixture of seven NPs with nearly overlapping longitudinal plasmon resonances that were hardly distinguishable in conventional absorption spectra (Fig. 15C). Thus, up to 10–15 multicolor functionalized NPs whose nonlinear spectra do not overlap in the window of tissue transparency (650–1100 nm) can be used to simultaneously target 10–15 and potentially more biomarkers. It should be emphasized that tunable ultrasharp resonances can be created both in the center and outside the absorption peaks [41]. Indeed, at higher laser energy the threshold for nanobubble formation can be achieved at lower NP absorption. With even small laser wavelength shifts towards the absorption peaks, PA signal amplification is immediately changed on PA signal inhibition due to ultra-fast reaching of the threshold of NP destruction during laser pulse through thermal-based NP melting and explosion [41]. It is important to note that nonlinear, ultrasharp PA spectral resonances are accompanied by amplification of PA signals that lead to dramatic increases in both the specificity and sensitivity of PAFC.

## 12. Combination of photoacoustic and fluorescent flow cytometry

*In vivo* PAFC and fluorescence flow cytometry (FFC) systems were previously employed separately using preferentially positive contrast and a pulsed and continuous wave laser sources, respectively. Recently we introduced a multimodal *in vivo* flow cytometry (PAFFC, Section 2.3) which integrates both techniques, and can use positive and negative contrasts and pulsed lasers [42]. The supplementary nature of PA and fluorescence methods provided dramatic increases in the detectable range of absorbing and fluorescent contrast agents. These included liposomes loaded with Alexa-660 dye, RBCs labeled with ICG, B16F10 melanoma cells co-expressing melanin and green fluorescent protein (GFP), C8161-GFP melanoma cells targeted by functionalized MNPs, MTLn3 adenocarcinoma cells expressing novel near-infrared iRFP protein, and QD-CNT conjugates. The use of a pulsed laser provided time-resolved discrimination of objects with a long fluorescence lifetime (e.g., QDs) from a shorter autofluorescence background (e.g., from blood plasma). Simultaneous PA and fluorescent detection of CTC-GFP (e.g., melanoma C8161-GFP) in tumor-bearing mice after injection of MNPs functionalized with antibody specific to melanoma receptors was useful for verification of CTC targeting by NPs directly in the bloodstream [42]. Our data showed that novel flow cytometry platform using negative contrast can provide label-free detection of low absorbing or weakly fluorescent cells in strong absorption blood background and autofluorescence background, respectively. Fig. 16 illustrates detection of low pigmented melanoma C8161-GFP cell which simultaneously provided positive fluorescence and negative PA signals. These data demonstrated that negative contrast label-free PAFC has the potential to detect single low absorbing cells with sizes down to 10–15 μm in 30–50 μm blood vessels (e.g., nonpigmented CTCs and likely WBCs). FFC also demonstrated the capability of label-free detection of red clots with weakly fluorescent RBCs providing negative contrast in blood plasma autofluorescence background, and white clots with fluorescent WBCs which provide positive contrasts above fluorescence background.

Thus, the combination of the positive and negative contrasts can be used for PA label-free enumeration of RBC and WBC

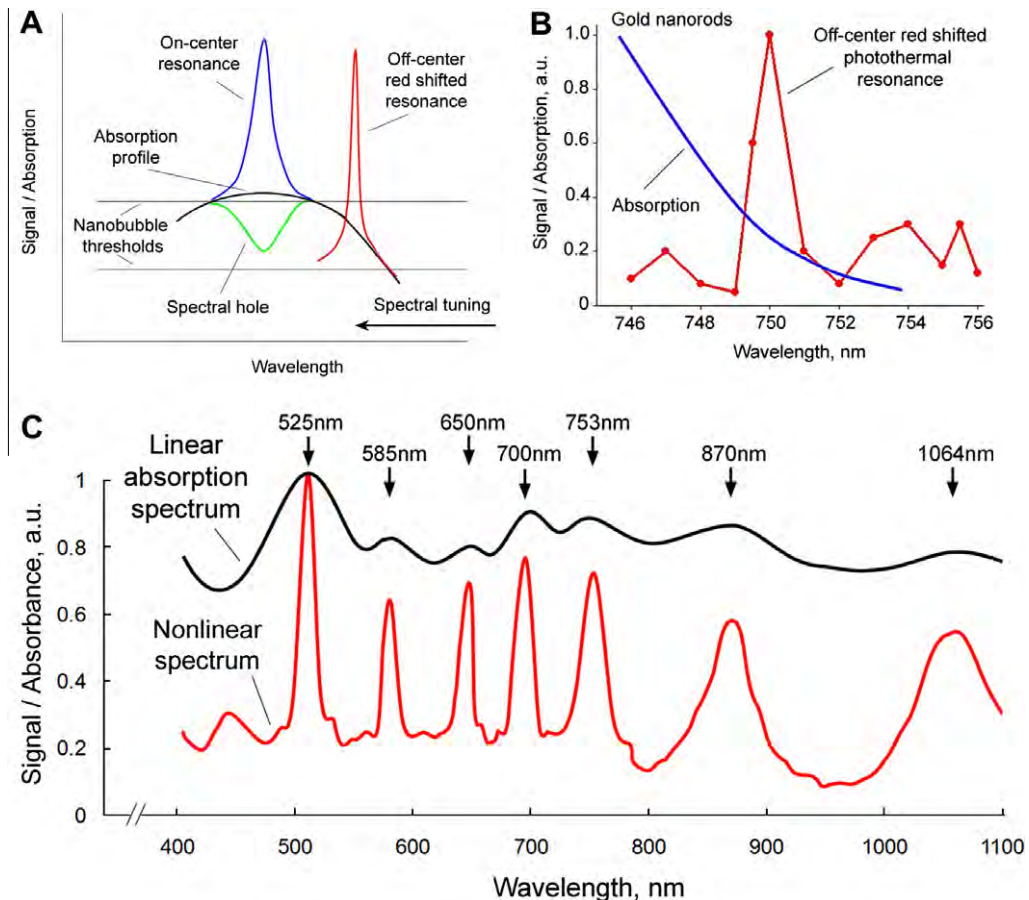


**Fig. 15.** Ultrasharp nonlinear PA and PT spectral resonances. (A) Ultra-narrow resonances and dips in a homogenous absorption profile. (B) Asymmetric (~0.8 nm in width) resonance in GNRs. (C) Absorption and nonlinear PT spectra of a mixture of 30 nm gold nanospheres and six gold nanorods with spectrally different Plasmon resonances.

aggregates, respectively. On the contrary, in FFC these cells and its aggregates produce label-free negative and positive contrast, respectively. This can provide synergy in identification of these cells using integrated PAFFC.

### 13. Conclusion

In this review, we have focused on the analysis of our recent results in the application of advanced *in vivo* flow cytometry using PA detection schematic and its combination with fluorescent techniques. The presented results suggest the excellent potential of PAFC as a new promising tool in biological research. This technology provides an unprecedented capability for real-time detection

of tumor cells, bacteria, and clots in circulation with ultra-high sensitivity as one cells or clot in the background of billion normal blood cells. This is unachievable with existing techniques.

Analogous to conventional *in vitro* flow cytometry, *in vivo* PAFC may have a broad spectrum of similar applications *in vivo*, as well as provide many new applications that may include label-free detection of various objects with intrinsic absorption or targeted by functionalized PA probes (e.g., NPs) in a variety of vessels such as capillaries, veins, arteries and afferent and efferent lymphatics in assorted locations including ear, skin, and deep organs for many disease models (e.g., cancer, infections, cardiovascular or immune system disorders). Further development of this technology may solve very complex and largely unexplored areas of medicine related to detection *in vivo* of infectious agents and stem, dendritic, and metastatic cells in different functional states (e.g., apoptosis) in lymph and blood flow at the single cell level. It may especially be used for early diagnosis of infections during its hematogenous spread with translocation of bacteria into different organs, vascular grafts, and stents. These infections commonly result in death caused by sepsis, despite aggressive treatment at the developed disease stage.

A transition of this technology to humans is anticipated with the development of portable devices attached to skin above selected blood vessels for alarm control of bacterial infection dissemination, cancer recurrence, metastasis development, and therapy assessment through controlling the number of circulating bacteria or metastatic cells, or monitoring of drug carriers (e.g., liposomes). One of the first clinical applications should be label-free detection of melanoma and circulating clots. The PAFC platform may allow

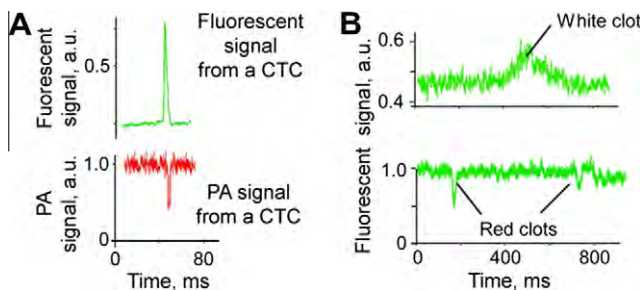


**Fig. 16.** Positive and negative contrasts in PA and fluorescence flow cytometry. (A) Negative PA, and positive fluorescent contrast signals from circulating C8161-GFP cells in 40- $\mu$ m ear artery of the mouse. (B) *In vivo* fluorescent monitoring of white and red clots with positive and negative contrast, respectively. Laser excitation wavelength: 488 nm; intensity: 80 W/cm<sup>2</sup>.

the development of portable, personal flow cytometers for blood testing without a needle stick, using compact, robust, low-cost, laser diode arrays with different wavelengths. The ability to assess a large blood volume *in vivo* [potentially the patient's entire blood volume (in adults ~5 L)] may significantly (10<sup>3</sup>-fold) enhance the sensitivity of CTC detection including rare cancer stem cells compared to the existing CTC assay *ex vivo*. If oncoming pilot clinical trials using the portable PA flow cytometry device are successful, this technology can provide breakthroughs for the early detection of CTCs when metastasis has not yet developed and, hence well-timed therapy including PT therapy is more effective. The future developments of PAFC may include the use of integrated PA – Raman cytometry, or the identification of various hemoglobins (e.g., metHb, HbCo, and HbCN) and measurements of oxygenation at a single RBC level [70,71], and nano-theranostics as the integration of ultrasensitive PA diagnostics and multiplex nanotechnology-based targeted PT therapy.

## Acknowledgements

This work was supported by the NIH Grants R01EB000873, R01CA131164, R01EB009230, and R21CA139373, by NSF Grants DBI-0852737 and by the Grants W88XWH-10-2-0130, W81XWH-11-1-0123 and W81XWH-11-1-0129. We thank Drs. J. Suen, D. Nedosekin, M. Proscurnin, M. Sarimollaoglu, E. Shashkov, M. Juratli and S. Ferguson and many other colleagues who participated in this work and co-authors of cited papers.

## References

- [1] H.M. Shapiro, Practical Flow Cytometry, fourth ed., Wiley-Liss, New York, 2003.
- [2] U. Sack, A. Tárnok, G. Rothe (Eds.), Cellular Diagnostics: Basic Principles, Methods and Clinical Applications of Flow Cytometry, Karger, Basel, Freiburg, Paris, 2008.
- [3] V.V. Tuchin, A. Tarnok, V.P. Zharov, *Cytometry A* 79A (2011) 737–745.
- [4] V.P. Zharov, E.I. Galanzha, V.V. Tuchin, Proc. SPIE 5320 (2004) 256–263.
- [5] E.I. Galanzha, V.V. Tuchin, P. Chowdhury, V.P. Zharov, Proc. SPIE 5474 (2004) 204–214.
- [6] E.I. Galanzha, P. Chowdhury, V.V. Tuchin, V.P. Zharov, *Lymphology* 38 (2005) 181–192.
- [7] E.I. Galanzha, V.V. Tuchin, V.P. Zharov, *J. Biomed. Opt.* 10 (2005) 54018.
- [8] V.P. Zharov, E.I. Galanzha, V.V. Tuchin, *Opt. Lett.* 30 (2005) 628–630.
- [9] V.P. Zharov, E.I. Galanzha, V.V. Tuchin, *J. Biomed. Opt.* 10 (2005) 51502.
- [10] V.P. Zharov, E.I. Galanzha, V.V. Tuchin, *J. Cell. Biochem.* 97 (5) (2006) 916–932.
- [11] V.P. Zharov, E.I. Galanzha, E.V. Shashkov, N.G. Khlebtsov, et al., *Opt. Lett.* 31 (2006) 3623–3625.
- [12] V.P. Zharov, E.I. Galanzha, Y.A. Menyaev, V.V. Tuchin, *J. Biomed. Opt.* 11 (2006) 054034.
- [13] V.P. Zharov, Yu. Menyaev, E.V. Shashkov, E.I. Galanzha, et al., Proc. SPIE 6085 (2006) 10–21.
- [14] V.P. Zharov, E.I. Galanzha, V.V. Tuchin, *Cytometry A* 71A (2007) 191–206.
- [15] V.P. Zharov, E.I. Galanzha, E.V. Shashkov, J.-W. Kim, et al., *J. Biomed. Opt.* 12 (2007) 0551503.
- [16] E.I. Galanzha, V.V. Tuchin, V.P. Zharov, *Lymphat. Res. Biol.* 5 (2007) 1127.
- [17] E.I. Galanzha, V.V. Tuchin, V.P. Zharov, *World J. Gastroenterol.* 13 (2007) 192218.
- [18] V. Kalchenko, A. Harmelin, I. Fine, V. Zharov, et al., Proc. SPIE 6436 (2007) 64360.
- [19] V. Kalchenko, A. Brill, M. Bayewitch, I. Fine, et al., *J. Biomed. Opt.* 12 (5) (2007) 052002-1–4.
- [20] E.I. Galanzha, E.V. Shashkov, V.V. Tuchin, V.P. Zharov, *Cytometry A* 73A (2008) 884–894.
- [21] W.L. Olszewski, A. Tárnok, *Cytometry A* 73A (2008) 1111–1113.
- [22] E.I. Galanzha, M.S. Kokoska, E.V. Shashkov, J.-W. Kim, et al., *J. Biophotonics* 2 (2009) 528–539.
- [23] S. Tanev, W. Sun, J. Pond, V.V. Tuchin, et al., *J. Biophotonics* 2 (2009) 505520.
- [24] V.V. Tuchin, E.I. Galanzha, V.P. Zharov, *In vivo Image Flow Cytometry*, in: V.V. Tuchin (Ed.), *Advance Optical Cytometry: Methods and Disease Diagnoses*, Wiley-VCH Verlag GmbH & Co. KGaA, Weinheim, 2011, pp. 387–431.
- [25] S. Tanev, W. Sun, J. Pond, V.V. Tuchin, V.P. Zharov, *Optical Imaging of Cells with Gold Nanoparticle Clusters as Light Scattering Contrast Agents: A Finite-Difference Time-Domain Approach to the Modeling of Flow Cytometry Configurations*, in: V.V. Tuchin (Ed.), *Advance Optical Cytometry: Methods and Disease Diagnoses*, Wiley-VCH Verlag GmbH & Co. KGaA, Weinheim, 2011, pp. 35–62.
- [26] V.V. Tuchin, E.I. Galanzha, V.P. Zharov, *In vivo Photothermal and Photoacoustic Flow Cytometry*, in: V.V. Tuchin (Ed.), *Advanced Optical Flow Cytometry*, Wiley-VCH Verlag GmbH & Co. KGaA, Weinheim, 2011, pp. 501–571.
- [27] J.-W. Kim, E.I. Galanzha, E.V. Shashkov, H.-M. Moon, et al., *Nat. Nanotechnol.* 4 (2009) 688–694.
- [28] E.I. Galanzha, E.V. Shashkov, T. Kelly, J.-W. Kim, et al., *Nat. Nanotechnol.* 4 (2009) 855–860.
- [29] A.S. Biris, E.I. Galanzha, Z. Li, M. Mahmood, et al., *J. Biomed. Opt.* 14 (2) (2009) 021006.
- [30] E.I. Galanzha, E.V. Shashkov, P. Spring, J.Y. Suen, et al., *Cancer Res.* 69 (2009) 7926–7934.
- [31] E.I. Galanzha, J.-W. Kim, V.P. Zharov, *J. Biophotonics* 2 (2009) 725–735.
- [32] E.V. Shashkov, E.I. Galanzha, V.P. Zharov, *Opt. Exp.* 18 (7) (2010) 6929–6944.
- [33] D.A. Nedosekin, M. Sarimollaoglu, E.V. Shashkov, E.I. Galanzha, V.P. Zharov, *Opt. Exp.* 18 (8) (2010) 8605–8620.
- [34] D.A. Nedosekin, M.V. Khodakovskaya, K. de Silva, E. Dervishi, et al., *Cytometry A* 79A (2011) 55–65.
- [35] E.I. Galanzha, V.P. Zharov, *Cytometry A* 79A (2011) 746–757.
- [36] E.I. Galanzha, M. Sarimollaoglu, D.A. Nedosekin, S.G. Keyrouz, et al., *Cytometry A* 79A (2011) 814–824.
- [37] D.A. Nedosekin, M. Sarimollaoglu, J.-H. Ye, E.I. Galanzha, et al., *Cytometry A* 79A (2011) 825–833.
- [38] M. Proskurnin, E.I. Galanzha, D.M. Mock, V.P. Zharov, *Cytometry A* 79A (2011) 834–847.
- [39] A. De la Zerda, J.W. Kim, E.I. Galanzha, S.S. Gambhir, et al., *Contrast Media Mol. Imaging* 6 (2011) 346–369.
- [40] M. Sarimollaoglu, D.A. Nedosekin, Y. Simanovsky, E.I. Galanzha, et al., *Opt. Lett.* 36 (2011) 4086–4088.
- [41] V.P. Zharov, *Nat. Photonics* 5 (2011) 110–116.
- [42] D.A. Nedosekin, M. Sarimollaoglu, E.I. Galanzha, R. Sawant, et al., *J. Biophotonics*, in press.
- [43] A.G. Bell, *Am. J. Sci.* 20 (1880) 305–324.
- [44] V.P. Zharov, V.S. Letokhov, *Laser optoacoustic spectroscopy*, Springer-Verlag, New York Springer, 1986.
- [45] A.A. Oraevsky, A.A. Karabutov, *Optoacoustic Tomography*, in: T. Vo-Dinh (Ed.), *Handbook of Biomedical Photonics*, CRC Press, Florida, 2003, pp. 34-1–34-34.
- [46] L.V. Wang, *Nat. Photon* 3 (2009) 503–509.
- [47] D. Rasansky, et al., *Nat. Photon.* 3 (2009) 412–417.
- [48] S.Y. Emelianov, P.C. Li, M. O'Donnell, *Phys. Today* 2 (8) (2009) 34–39.
- [49] P.C. Beard, *Interface Focus* 1 (4) (2011) 602–631.
- [50] J. Novak, I. Georgakoudi, X. Wei, A. Prossin, et al., *Opt. Lett.* 29 (2004) 7779.
- [51] W. He, H. Wang, L.C. Hartmann, J.X. Cheng, *Proc. Natl. Acad. Sci. USA* 104 (28) (2007) 1176011765.
- [52] E.R. Tkaczyk, C.F. Zhong, J.Y. Ye, A. Myc, et al., *Opt. Commun.* 281 (2008) 888894.
- [53] C. Greiner, I. Georgakoudi, *Advances in Fluorescence-Based In vivo Flow Cytometry for Cancer Application*, in: V.V. Tuchin (Ed.), *Advanced Optical Cytometry: Methods and Disease Diagnoses*, Wiley-VCH Verlag GmbH & Co. KGaA, Weinheim, 2011, pp. 463–500.
- [54] E.R. Tkaczyk, A.H. Tkaczyk, *Cytometry A* 79 (10) (2011) 775–788.
- [55] V.P. Zharov, D.O. Lapotko, J. Sel., *Topics Quant. Electron.* 11 (2005) 733–751.
- [56] D.A. Nedosekin, E.I. Galanzha, S. Ayyadevara, et al., *Biophys. J.* 102 (3) (2012) 672–681.
- [57] V.P. Zharov, V. Galitovskiy, C.S. Lyle, T.C. Chambers, et al., *J. Biomed. Opt.* 11 (2006) 064034.
- [58] M. Yu, S. Stott, M. Toner, S. Maheswaran, D.A. Haber, *J. Cell Biol.* 192 (3) (2011) 373–382.
- [59] V.P. Zharov, J.-W. Kim, M. Everts, D.T. Curiel, *J. Nanomed.* 1 (2005) 326–345.
- [60] N. Pamme, *Lab Chip* 6 (2006) 24–38.
- [61] H. Nakshatri, E.F. Srour, S. Badve, *Curr. Stem Cell Res. Ther.* 4 (1) (2009) 50–60.
- [62] E.I. Galanzha, *J. Blood Lymph* 1 (2011) 1–2.
- [63] C.L. Weston, M. J. Glantz, J. R. Connor, *Fluids Barriers CNS* 8(1) (2011) 14.
- [64] A.S. Patel, J.E. Allen, D.T. Dicker, K.L. Peters, et al., *Oncotarget* 10 (2011) 752–760.
- [65] V.P. Zharov, K.E. Mercer, E.N. Galitovskaya, M.S. Smeltzer, *Biophys. J.* 90 (2006) 619–627.
- [66] J.W. Kim, E.I. Galanzha, E.V. Shashkov, N. Kotagiri, et al., *Laser Surg. Med.* 39 (2007) 622–634.
- [67] P. Jurasz, A. Escalano, M.W. Radomski, *Br. J. Pharmacol.* 143 (2004) 819–826.
- [68] G.G. Agnelli, *Circulation* 110 (Suppl. IV) (2004) IV4–IV12.
- [69] M.V. Khodakovskaya, K. de Silva, D.A. Nedosekin, E. Dervishi, et al., *Proc. Natl. Acad. Sci. USA* 108 (3) (2011) 1028–1033.
- [70] A. Brusnickin, D. Nedosekin, E. Ryndina, M. Proskurnin, E. Gleb, D. Lapotko, Y. Vladimirov, V. Zharov, *Moscow Univ. Chem. Bull.* 64 (2009) 45–54.
- [71] V. Zharov, E. Galanzha, E. Shashkov, N. Khlebsov, V. Tuchin, *SPIE Newsroom* (2006), <http://dx.doi.org/10.1117/2.1200609.0391>.
- [72] J. Mazen, E.I. Galanzha, M. Sarimollaoglu, D.A. Nedosekin, J. Suen, V.P. Zharov, *In vivo detection of circulating tumor cells during tumor manipulation*. Head Neck, submitted for publication.
- [73] E. Galanzha, E.I. Shashkov, M. Sarimollaoglu, K.E. Beenken, A. Basnakian, J.-W. Kim, M. Shirtliff, M.S. Smeltzer, V.P. Zharov, *In vivo magnetic enrichment, photoacoustic diagnosis and photothermal purging of infected blood using multifunctional gold and magnetic nanoparticles*. *PloS ONE*, in press.

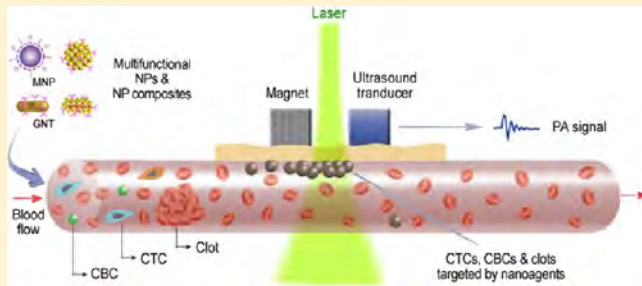
## Nanotheranostics of Circulating Tumor Cells, Infections and Other Pathological Features *In Vivo*

Jin-Woo Kim,<sup>\*,†,‡,§</sup> Ekaterina I. Galanzha,<sup>||,⊥</sup> David A. Zaharoff,<sup>§</sup> Robert J. Griffin,<sup>⊥,#</sup> and Vladimir P. Zharov<sup>\*,||,⊥</sup>

<sup>†</sup>Bio/Nano Technology Laboratory, Institute for Nanoscience and Engineering, <sup>‡</sup>Department of Biological and Agricultural Engineering, and <sup>§</sup>Department of Biomedical Engineering, University of Arkansas, Fayetteville, Arkansas 72701, United States

<sup>||</sup>Phillips Classic Laser and Nanomedicine Laboratories, <sup>⊥</sup>Arkansas Nanomedicine Center, and <sup>#</sup>Department of Radiation Oncology, University of Arkansas for Medical Sciences, Little Rock, Arkansas 72205, United States

**ABSTRACT:** Many life-threatening diseases are disseminated through biological fluids, such as blood, lymph, and cerebrospinal fluid. The migration of tumor cells through the vascular circulation is a mandatory step in metastasis, which is responsible for ~90% of cancer-associated mortality. Circulating pathogenic bacteria, viruses, or blood clots lead to other serious conditions including bacteremia, sepsis, viremia, infarction, and stroke. Therefore, technologies capable of detecting circulating tumor cells (CTCs), circulating bacterial cells (CBCs), circulating endothelial cells (CECs), circulating blood clots, cancer biomarkers such as microparticles and exosomes, which contain important microRNA signatures, and other abnormal features such as malaria parasites in biological fluids may facilitate early diagnosis and treatment of metastatic cancers, infections, and adverse cardiovascular events. Unfortunately, even in a disease setting, circulating abnormal cells are rare events that are easily obscured by the overwhelming background material in whole blood. Existing detection methods mostly rely on *ex vivo* analyses of limited volumes (a few milliliters) of blood samples. These small volumes limit the probability of detecting CTCs, CECs, CBCs and other rare phenomena. *In vivo* detection platforms capable of continuously monitoring the entire blood volume may substantially increase the probability of detecting circulating abnormal cells and, in particular, increase the opportunity to identify exceedingly rare and potentially dangerous subsets of these cells, such as circulating cancer stem cells (CCSCs). In addition, *in vivo* detection technologies capable of destroying and/or capturing circulating abnormal cells may inhibit disease progression. This review focuses on novel therapeutic and diagnostic (theranostic) platforms integrating *in vivo* real-time early diagnosis and nano-bubble based targeted therapy of CTCs, CECs, CBCs and other abnormal objects in circulation. This critical review particularly focuses on nanotechnology-based theranostic (nanotheranostic) approaches, especially *in vivo* photoacoustic (PA) and photothermal (PT) nanotheranostic platforms. We emphasize an urgent need for *in vivo* platforms composed of multifunctional contrast nanoagents, which utilize diverse modalities to realize a breakthrough for early detection and treatment of harmful diseases disseminated through the circulation.



**KEYWORDS:** metastasis, circulating tumor cells (CTCs), circulating endothelial cells (CECs), circulating cancer stem cells (CCSCs), circulating microparticles and exosomes, circulating pathogens, viruses and parasites, blood clots, blood and lymph flow, contrast nanoagents, positive and negative photoacoustic contrasts, micro- and nanobubbles, multimodal, multicolor, nanotechnology, multifunctional real-time nanotheranostics, nanomedicine

### INTRODUCTION

Progression of many fatal diseases is mediated through the vascular dissemination of pathological cells. For example, tumor cells are continuously shed from primary solid tumors into the vascular circulation. These circulating tumor cells (CTCs) are the precursors of metastasis, which accounts for 9 out of every 10 cancer-related deaths.<sup>1</sup> Also, bacteria reaching the circulation often cause systemic infections and sepsis. Bacteremia is a significant cause of mortality in developing countries as well as a threat to developed countries due to the rapid emergence of antibiotic-resistant strains.<sup>2</sup> Furthermore, arterial and pulmonary embolisms due to circulation of blood

clots often lead to severe cardiovascular and cerebrovascular events. Taken together, the detection and enumeration of circulating pathological features, such as CTCs, circulating bacterial cells (CBCs), and clots (referred also as throm-

**Special Issue:** Theranostic Nanomedicine with Functional Nano-architecture

**Received:** October 11, 2012

**Revised:** February 1, 2013

**Accepted:** February 4, 2013

**Published:** February 4, 2013

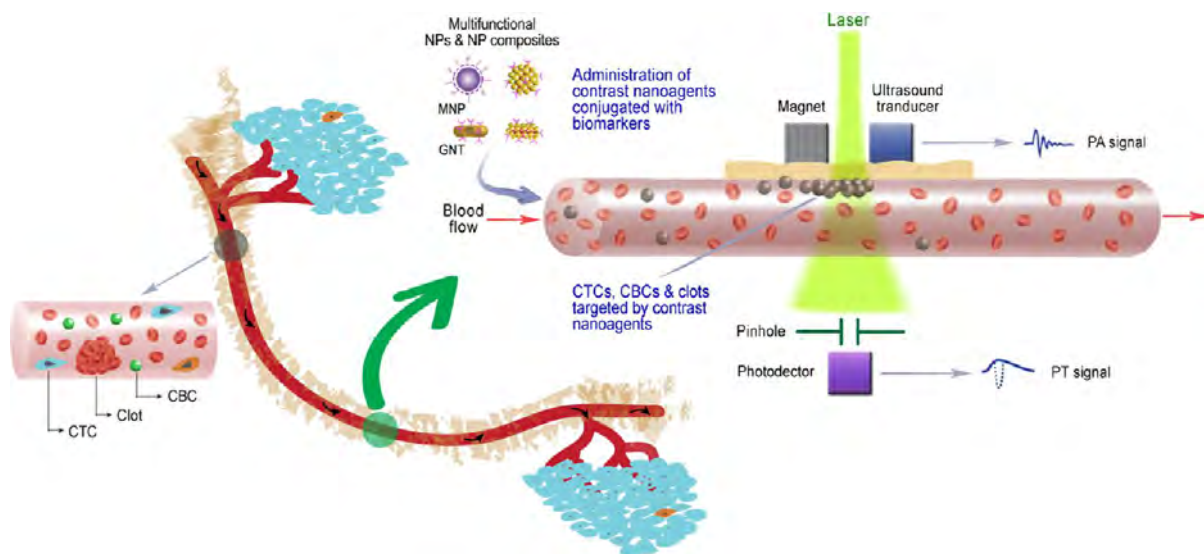


**Figure 1.** *In vivo* multimodal multicolor nanotheranostic platform integrating magnetic enrichment, PA detection, PT therapy, and real-time PA monitoring of PT therapeutic efficacy of circulating pathological features, including circulating tumor cells (CTCs), circulating endothelial cells (CECs), circulating cancer stem cells (CCSCs), circulating bacterial cells (CBCs), circulating blood clots (i.e., thromboemboli and emboli), and other biomolecules and cells (i.e., DNA, RNA, exosomes and microparticles, etc.).

boemboli or emboli), are clinically significant for many life-threatening diseases.

However, detection of circulating abnormal features presents numerous challenges given their rarity relative to the overwhelming amount of nonpathogenic or background material in blood. For example, even in patients with advanced cancer, only about one CTC for every million leukocytes and billion erythrocytes is expected. To date, most detection methods enumerate circulating abnormal cells in a small volume (5–20 mL) of blood drawn from patients.<sup>3–15</sup> The small sample volume limits the ability of *ex vivo* techniques to detect exceedingly rare populations. In particular, the potential for real-time diagnosis of metastatic diseases at earlier stages is hindered by low cell counts in small volumes acquired at fixed time points.<sup>11,13</sup> Furthermore, the use of small blood volumes limits the collection of abnormal cells for later analysis to investigate their role in disease progression. Hence, the development of effective and efficient detection platforms capable of interrogating the entire circulation *in vivo* and in real time is necessary to realize the enormous diagnostic potential of circulating pathogenic cells and biomolecules.

Recent development of nanoparticles (NPs) with unique physicobiochemical properties for biomedical applications offers immense promise in the advancement of therapeutics and diagnostics (theranostics). Various NPs with different shapes and compositions have been proven effective as theranostic contrast nanoagents.<sup>9,16–20</sup> Particularly, tunable near-infrared (NIR)-responsive plasmonic NPs, including gold nanoshells (GNSs), gold nanorods (GNRs), and golden carbon nanotubes (GNTs),<sup>9,12,16,21</sup> have attracted attention for minimally invasive imaging and therapy owing to their high NIR absorption (e.g., ~700–900 nm) in the window of optical transparency of most biological tissues as well as high efficiency conversion of absorbed energy into thermal and acoustic phenomena.<sup>2,9,11–15</sup> Recently,<sup>2,9,11–15</sup> a completely new *in vivo* noninvasive multicolor and multimodal concept using dual NIR-responsive NP-based contrast agents and two-color laser-based *in vivo* photoacoustic (PA) and photothermal (PT) flow cytometry (PAFC/PTFC) to detect, capture, and

purge rare circulating tumor and other pathological cells in the peripheral circulation were introduced by our team (Figure 1). These technical platforms demonstrated high potential to overcome the aforementioned limitations of small blood sample volumes and to enable a broad range of clinical applications, including early disease theranostics and evaluation of disease progression.<sup>2,9,11–15</sup> Some groups also proposed similar approaches to achieve real-time detection of CTCs using fluorescence-labeled biomarkers with some degree of success.<sup>22,23</sup> Although PAFC/PTFC is still at an early stage in development, the *in vivo* theranostic platforms, in particular nanotechnology-based theranostics (nanotheranostics), carry enormous clinical potential for the therapy and management of life-threatening diseases.

Here, we review recent advances in *in vivo* real-time detection and characterization of circulating pathogenic cells and other disease-associated features. The challenges of *in vivo* detection, particularly at early stages of disease, are discussed as well as several potential strategies to overcome them. This critical review is not meant to be comprehensive. The history and current state of the art and science for cancer cell metastasis and recent advances in their detection technologies, in particular *ex vivo* approaches and a few reports on *in vivo* micro- or macro-scale devices such as implantable microfluidic devices, have been reviewed elsewhere.<sup>3–7,10</sup> Specifically, this critical review focuses on nanotheranostic approaches, particularly PA and PT *in vivo* platforms, with advanced multifunctional contrast nanoagents to realize real-time imaging and therapy for CTCs and other circulating pathological cells and biomolecules. Also, we stress the need and promise of *in vivo* multimodal synergistic platforms, which integrate multimodal contrast nanoagents and multiple modalities for effective early diagnosis and therapy. Finally, we conclude with a discussion of future directions and current needs for research in the field. The purpose of this discussion is to stimulate ideas regarding practical strategies for implementation of *in vivo* multifunctional nanotheranostics in the clinic.

## ■ CHALLENGES AND OPPORTUNITIES

The detection of circulating markers of disease including CTCs, circulating endothelial cells (CECs), circulating cancer stem cells (CCSCs), CBCs, circulating blood clots, and other biomolecules and cells (i.e., DNA, RNA, exosomes, micro-particles, parasites and other infected cells) is emerging as a vital clinical tool for the early diagnosis and treatment of cancer, infections, and cardiovascular diseases. In addition, platforms that allow for the collection of sufficient numbers of circulating pathogenic cells are helping to elucidate critical biological mechanisms of disease progression. For example, the collection and study of CTCs is helping improve our understanding of metastasis, including the discovery of critical surface and intracellular biomarkers related to metastatic progression and/or more aggressive phenotypes.

A considerable number of highly sensitive and specific *ex vivo* detection techniques are under investigation to detect CTCs, CECs, and CBCs in small volumes of peripheral blood. These techniques involve reverse transcriptase polymerase chain reaction (RT-PCR), flow cytometry, microfluidics-based technologies, and others.<sup>3–11</sup> The relative ease of sample collection makes *ex vivo* peripheral blood assessments convenient for noninvasive monitoring of disease progression. However, sensitivity thresholds of existing *ex vivo* detection methods are 1–10 cells per 1 mL of whole blood. Therefore, on average, abnormal cells remain undetectable until their numbers reach 5,000–50,000 in an average adult blood volume of ~5 L.

Another challenge is that CTCs, like many circulating pathogenic cells, are highly heterogeneous.<sup>24–26</sup> Not all CTCs express the same markers, and some may even have completely different phenotypes than the associated primary tumor.<sup>1</sup> Furthermore, while CTCs are mandatory for metastasis, not all CTCs cause metastasis.<sup>24–27</sup> Recent evidence indicates that certain subpopulations of CTCs, such as tumor-initiating cells or CCSCs,<sup>27</sup> may be key drivers of metastasis.<sup>1</sup> In fact, only about 0.01% of CTCs were estimated to form metastatic lesions.<sup>28,29</sup> It is not known whether this 0.01% represents a unique subset of aggressive tumor cells, perhaps CCSCs or invasive mesenchymal-like tumor cells, or whether 0.01% represents the infinitesimal probability that a given CTC can survive a “decathlon”<sup>29</sup> of challenges to establish a metastatic lesion. If 0.01% represents some exceedingly rare subpopulation of CTCs, the probability of detecting or collecting these cells in a 5–20 mL sample is negligible.

Similar to cancer metastasis via CTCs, many key questions regarding bacteria dissemination to distant organs, including CBC migration in tissue, invasion dynamics, interaction with blood and endothelial cells, and extravasation, remain unanswered.<sup>2</sup> Unfortunately, the removal of either CTCs or CBCs from the host in order to study their biological processes may alter properties, such as cell morphology and biomarker expression. Moreover, *in vitro* sample preparation procedures do not reproduce the native *in vivo* environment, and thus are not able to provide accurate data regarding native cell-to-cell interactions, cell migration, or control of cell apoptosis and proliferation by the host environment.<sup>15</sup>

We submit that *in vivo* real-time nanotheranostics has the potential to overcome challenges associated with detecting exceedingly rare populations in whole blood and to help elucidate unknown biological mechanisms of disease progression. Regarding the former, an *in vivo* approach allows for

the interrogation of the entire (~5 L) circulation, which is expected to increase detection sensitivity by at least 2 if not 3 order of magnitude over current *ex vivo* approaches. Regarding the mechanisms of disease progression, *in vivo* nanotheranostics can enrich abnormal cells for either *in vivo* analyses of biological function or minimally invasive extraction to perform assessments *ex vivo*. A third advantage of nanotheranostics is the ability to monitor responses to various therapies continuously and in real time. *Ex vivo* approaches offer only snapshots of responses during treatment. A fourth advantage of *in vivo* nanotheranostics is their potential for delivering treatment or destroying pathogenic cells upon recognition. This targeted elimination of pathogenic cells may significantly alter the course of disease.

We note that, even with increased specificity and the capability to do continuous monitoring, the markers and targets allowing us to identify these rare events are still under exploration. As discussed later, few if any validated targets have been identified. Nonetheless, *in vivo* real-time nanotheranostics, with the advent of more reliable detection markers, represent a potentially powerful tool for early detection and management of life-threatening diseases. Subsequent sections of this review will cover recent advances, technical challenges, and strategies for future development.

## ■ IN VIVO NANOTHERANOSTICS OF CIRCULATING DISEASE-ASSOCIATED CELLS AND BIOMOLECULES: RECENT ADVANCES

In this section, we present the current status of *in vivo* nanotheranostic platform development for circulating disease-associated cells and biomolecules. In particular, we focus on *in vivo* PAFC/PTFC nanotheranostic platforms with advanced contrast nanoagents. It is noted that a similar approach using fluorescence-labeled tumor-associated ligands for *in vivo* FC is also under investigation.<sup>22,23,30</sup> However, *in vivo* applications using fluorescent labels are usually hampered by tag-associated problems such as photobleaching, blinking or strong light scattering, and background autofluorescence.<sup>11</sup> On the other hand, contrast nanoagents, such as plasmonic nanoparticles, exhibit much higher optical absorption and photostability. Furthermore, when integrated with PA and PT techniques, nanoagents are capable of multimodal detection and therapy of abnormal cells.

**In Vivo PAFC and PTFC Nanotheranostic Platform.** *In vivo* real-time PAFC/PTFC detection of circulating abnormal cells and biomolecules using NIR NPs as PA and PT contrast agents was first demonstrated in 2004 by Zharov et al.,<sup>31</sup> followed by its further development and extension to various biomedical applications.<sup>2,9,11–16,30–44</sup> In 2009, our group reported a novel multicolor PAFC/PTFC using novel multimodal NPs as nanotheranostic agents and demonstrated, for the first time, *in vivo* real-time imaging and therapy of CTCs and CCSCs.<sup>9,11–15</sup> Other theranostic targets, including bacteria (i.e., CBCs), micro/nanoparticles, and emboli,<sup>9,11</sup> were also explored. In these studies, we demonstrated the potential of *in vivo* multispectral PAFC/PTFC for ultrasensitive noninvasive molecular quantitative detection, intravascular magnetic enrichment, and targeted laser ablation of pathological cells in circulation. The multicolor multiparameter high-speed PAFC/PTFC was capable of clinically relevant molecular detection and enumeration of cells of interest among highly heterogeneous populations of blood cells *in vivo* that has never been possible before. Integration of PA and PT

approaches using the same technical platform allowed robust and relatively inexpensive combination of diagnosis and targeted therapy of rare abnormal cells directly in blood circulation *in vivo*. The potential advantages of PAFC/PTFC in comparison with other *in vitro* approaches include (1) analyzing mobile cells in moving fluids, (2) rapid (a few minutes) testing (up to  $\sim 10^{11}$  cells/s in human jugular vein) of the largest blood volume (up to whole blood volume, i.e.,  $\sim 50-100$  times more than the volume of conventional samples) at unrestricted speeds, and (3) unprecedented sensitivity threshold at one pathological cell, such as a CTC, among a billion normal blood cells and millions of white blood cells (WBCs) in lymph flow.<sup>11,36</sup> The advantages of PAFC over existing *in vivo* technologies also include (1) time-resolved and deep detection of specific acoustic signals from individual metastatic cells (depth up to 7 cm), (2) multicolor detection, (3) use of functionalized NPs as unique NIR-absorbing low toxic supercontrast PA molecular agents, and (4) noninvasiveness for normal tissue due to a relatively low level of laser energy, i.e., well within safety parameters of laser use for humans.

**PAFC/PTFC Schematics.** The nanotheranostic platform integrates *in vivo* PAFC/PTFC and PT therapy of circulating abnormal objects, e.g., CTCs, CBCs, etc. (Figure 1).<sup>9,11-15</sup> PAFC is based on time-resolved detection of laser-induced acoustic waves from targeted objects (referred to as PA signals) with an ultrasound transducer attached to the skin (Figure 1). Laser radiation can be delivered to biological tissue by using either a microscope schematic with a customized condenser to create the desired linear beam shapes ranging from  $5 \times 50 \mu\text{m}$  to  $25 \times 150 \mu\text{m}$  or a fiber with a miniature tip and cylindrical optics. PAFC molecular specificity is provided either by label-free intrinsic absorption spectroscopic contrast (e.g., hemoglobin or melanin) or by strongly absorbing, low-toxicity, biofunctionalized contrast nanoagents, such as NPs. Preclinical feasibility studies of PAFC and PTFC *in vivo* involved nude mouse tumor models of melanoma (Figure 2A) and breast cancer (Figure 2B). The noninvasive

autofluorescence background, respectively. In PAFFC, conventional positive contrast mode was combined with the new negative PA and fluorescent contrast modes especially for PA detection of cells with lower absorption than red blood cells (RBCs) similarly as platelets or WBCs.<sup>42</sup> PAFC was also integrated with PT techniques, i.e., PTFC and PT therapy.<sup>9,11,16,32</sup> In the diagnostic mode with PT thermal lens, a laser-induced refractive heterogeneity causes defocusing of a collinear He–Ne laser probe beam and hence a reduction in the beam's intensity at its center, as detected by a photodiode with a pinhole (referred to as PT signals).<sup>15,16</sup> PT signals from single cells in a linear mode (i.e., without notable cell photodamage) represent a standard positive peak associated with rapid (i.e., pico- to nanosecond scale) cell heating and a slower, microsecond scale tail corresponding to cell cooling. PA and PT methods beneficially supplement each other and, in combination, provide a very powerful theranostic tool. For example, noninvasive PA diagnostics can be combined with PT purging of CTCs and CBCs using more powerful laser pulses.

**Labeling *in Vivo*.** A unique advantage of *in vivo* PAFC/PTFC is the possibility for cell detection without labeling, for example by using the positive and negative PA and PT contrast of RBCs and WBCs vs the negative and positive fluorescent contrast of the same cells.<sup>30,42</sup> PA or PT signals can be generated from intrinsic chromophores and pigments such as hemoglobin, melanin, cytochromes, or carotenoids. Also cells with a low endogenous absorption can be labeled directly in the bloodstream through intravenous injection of strongly absorbing functionalized NPs.<sup>2,9,11,13</sup> Depending upon the properties of cells and NPs, the *in vivo* labeling procedure using mouse models takes from 10–20 min to 1 h. Labeling specificity is provided through the selection of molecular markers that are highly expressed in targeted cells (e.g., CTCs and CBCs), but almost absent in normal blood and endothelial cells (e.g., folates in CTCs).<sup>13,22</sup> High labeling efficiency is associated with frequent collisions between NPs and abnormal cells (e.g., CTCs) in partly turbulent blood flow. The PA/PT signals from targeted cells with a typical NP number, for example ranging from 500 to 5000 NPs per CTC cell, are much higher than the PA/PT signal background from RBCs, unbound NPs with typical numbers of 1–10 in the detected volume, or NPs nonspecifically bound to normal blood cells. NP clustering around naturally densely packed cell markers would lead to a significant linear (5–50-fold) and nonlinear (100–300-fold) nanobubble-based enhancement in PA/PT signal amplitude and a red-shift effect in the absorption of coupled NPs in clusters,<sup>16</sup> both of which serve as indicators of successful cell targeting.

**Detection Threshold.** Two types of NPs were used to estimate the detection threshold sensitivity of PAFC *ex vivo*, including GNTs<sup>12</sup> and magnetic NPs (MNPs).<sup>13</sup> GNTs consist of hollow shortened CNTs surrounded by thin gold layers, averaging  $11 \text{ nm} \times 98 \text{ nm}$  in diameter and length, respectively. They exhibit high water solubility and biocompatibility, low cytotoxicity (due to the protective layer of gold), and spectrally tunable high plasmon absorption in the NIR range of 700–1000 nm. The minimal number of NPs in the detected (i.e., irradiated) volume that produced readable PA signals in the background of mouse blood in the  $120 \mu\text{m}$  microscopic slide was estimated to be  $120 \pm 14$  for MNPs at 639 nm, and  $7 \pm 2$  for GNTs at 900 nm under laser fluence of  $100 \text{ mJ/cm}^2$  in nonlinear mode at both wavelengths, and 35

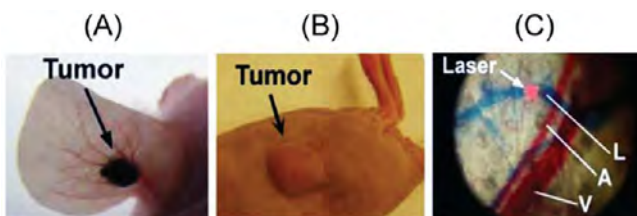


**Figure 2.** Animal models. (A) Mouse ear melanoma model. (B) Mouse breast cancer model. (C) Ear fragment (A, arteriole; V, vein; and L, lymph) visualized with Evans Blue staining *in vivo*.

PA detection of cells in blood and lymphatic systems was carried out using (1) the mouse ear (Figure 2C) and (2) the skinfold chamber.

The use of a single technique limits the range of detectable cells with different optical properties.<sup>11</sup> Recently, we demonstrated real-time integration of PAFC and fluorescent flow cytometry (FFC), termed PAFFC,<sup>30</sup> using pulsed and continuous wave (CW) lasers as traditional sources for the generation of PA and fluorescent signals, respectively. Conventional PA and fluorescence techniques use preferential positive imaging contrasts when signals from strongly absorbing or fluorescent cells are above absorption or

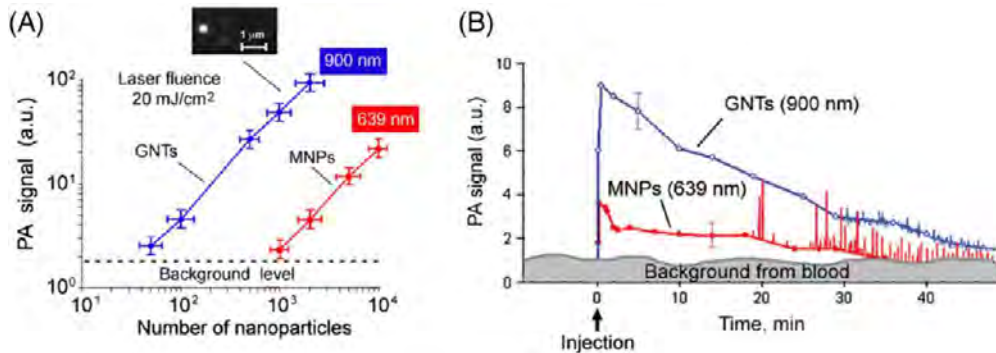


**Figure 3.** Optimization of NP parameters *in vitro* and *in vivo*. (A) *In vitro* PA signals from NPs at different concentrations in a slide. Callout represents fluorescent images of individual GNTs conjugated with FITC and Abs specific to CD44. (B) *In vivo* measurements of NPs and cells mimicking CTCs. Kinetics of clearance of 30 nm MNPs (red curve with filled circles) and GNTs (blue curve with open circles) at a concentration of  $1 \times 10^{11}$  NPs/mL in a  $70 \mu\text{m}$  mouse ear vein. The error bars represent standard error ( $n = 3$ ). Adapted with permission from ref 13. Copyright 2009 Nature Publishing Group.

for GNTs and 600 for MNPs at laser fluence of  $20 \text{ mJ/cm}^2$  (Figure 3A).<sup>13</sup>

The detection threshold sensitivity of PAFC *in vivo* was estimated as follows using GNTs.<sup>12</sup> The  $10 \mu\text{L}$  GNT suspension ( $\sim 10^{11}/\text{mL}$ ) was injected intravenously into mice with total blood volume of  $\sim 2 \text{ mL}$ . Assuming ideal conditions with no loss of GNTs during injection and in circulation, the average GNT concentration in the blood pool should have been  $5 \times 10^8 \text{ GNTs/mL}$ . The irradiated (detected) volume in blood vessel of mouse ear was limited by laser beam size and the diameter of the vessels. Assuming a linear beam shape with a width of  $15 \mu\text{m}$  and a vessel diameter of  $60 \mu\text{m}$  in mouse ear, the detected volume was estimated as  $4.2 \times 10^{-8} \text{ cm}^3$ . These parameters correspond to the estimated maximum number of GNTs (around 21) in the detected volume. Taking into account the threshold sensitivity as 7 GNTs at laser fluence  $100 \text{ mJ/cm}^2$ , it is expected that the signal-to-noise ratio (SNR) *in vivo* in blood vessel is  $\sim 3$  (i.e., 21/7). However, it was experimentally determined that the SNR is  $\sim 7$ . This discrepancy can be explained by uncontrollable formation of small GNT aggregates in flow, which provided a stronger PA signal as compared to suspensions of single GNTs. Injection of high concentrations of each unconjugated NP alone (iv,  $\sim 10^{11}$  NPs/ $50 \mu\text{L}$ ) in mice revealed their fast clearance during 15–20 min, with no PA detection at low concentrations ( $\sim 10^9$  NPs/ $50 \mu\text{L}$ ) (Figure 3B).

Blood samples collected from mice with tumors at week 1 after cell labeling were put onto a slide with thickness of  $120 \mu\text{m}$  and scanned at a fixed position of focused laser beam ( $10 \mu\text{m}$  in diameter). The rare CTCs in blood samples were detected through a remarkable increase in PA signal amplitudes. The presence of cancer cells in a thin blood sample were further verified with optical imaging using specific morphological features such as observing a size greater than normal blood cells. Comparison of PA data *in vivo* and *in vitro* revealed that the threshold sensitivity of PAFC *in vivo* can be estimated as  $\sim 1 \text{ CTC/mL}$ .<sup>11,32</sup> This threshold sensitivity was primarily limited by the small blood volume ( $2 \text{ mL}$ ) in mice rather than PAFC parameters. In humans, sensitivity should be higher by examining large blood volumes circulating through the peripheral vasculature. According to modeling, there is potential to achieve sensitivity of  $1 \text{ CTC}/10 \text{ mL}$  (i.e., one order better than existing assays) by monitoring  $200\text{--}300 \mu\text{m}$

vessel over  $\sim 1 \text{ h}$  and to achieve a sensitivity of  $1 \text{ CTC}/100 \text{ mL}$  by examining  $1\text{--}2 \text{ mm}$  peripheral blood vessels.

**In Vivo PAFC/PTFC Nanotheranostic Applications.** *In Vivo Label-Free Theranostics of Melanoma CTCs.* Melanin, which is an intrinsic PA/PT contrast agent, is located in melanoma cells and in  $\sim 0.7 \mu\text{m}$  melanosomes as aggregates of melanin NPs with typical size range of 50–150 nm. Hence, melanoma is an optimal target for PAFC that can facilitate routine, label-free, *in vivo* clinical assessment of CTCs for earlier detection of this most aggressive cancer with increasing incidence rates. In our study, the overexpression of melanin was used as an intrinsic high contrast PA/PT NIR agent, which provided PA signals above the blood absorption background. Real-time PA counting of metastatic melanoma CTCs (B16F10) was performed in a  $50 \mu\text{m}$  diameter vessel in the ear of tumor-bearing mice.<sup>32</sup> CTCs could be readily detected with PAFC weeks before any evidence of detectable metastasis appears in the tissue samples with conventional techniques. The PAFC's sensitivity threshold was found around  $1 \text{ CTC/mL}$ . This unprecedented threshold sensitivity on the animal model provides an opportunity to use PAFC as a powerful research tool to study CTC behaviors and their role in the development of metastasis at an early cancer stage. As mentioned previously, the PAFC sensitivity has potential to be further improved 100-fold (i.e.,  $\sim 1 \text{ CTC}/100 \text{ mL}$ ), which is unachievable with existing techniques. Also, we recently developed a portable clinical prototype of PAFC using a high-pulse-repetition rate laser at  $1064 \text{ nm}$  with pulse rates up to  $0.5 \text{ MHz}$ , fiber delivery of laser radiation, and a focused, ultrasound transducer gently attached to the skin near selected blood vessels.

Increasing the laser energy fluence from  $60 \text{ mJ/cm}^2$  to  $600 \text{ J/cm}^2$  at  $820 \text{ nm}$  wavelength, PA contrast of the CTCs increased  $\sim 6$  times above the RBC background.<sup>32</sup> This effect was associated with laser-induced nanobubbles around overheated strongly absorbing melanin nanoclusters in melanoma cells, which served as a nonlinear PA signal amplifier compared to linear PA signals from RBCs with homogeneous hemoglobin distribution (i.e., with no nanobubble formation). Also, the rates of CTCs have been gradually decreased from 12 CTC/min to 1–2 CTC/min over a 1 h monitoring period (Figure 4), demonstrating effective purging of circulating melanoma cells. This was also related to the generation of nanobubbles, which served as melanoma cell killers.<sup>15</sup> Further

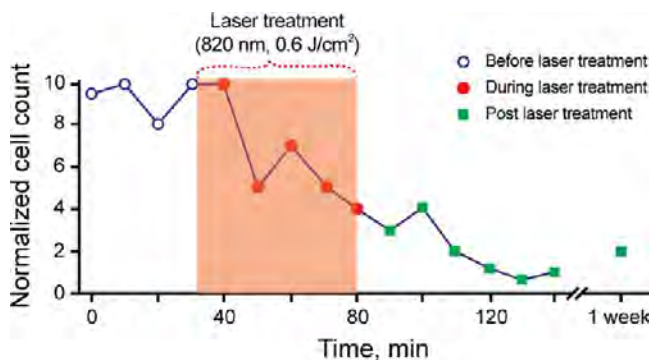


Figure 4. PA guidance of PT therapy of melanoma CTCs. Adapted with permission from ref 11. Copyright 2012 Elsevier.

study could determine whether these new PA/PT theranostics are effective enough to be used alone, or whether it should be used in combination with other therapies such as chemotherapy or radiation therapy.

**In Vivo Multiplex, Multicolor, and Multimodal Nanotheranostics of CTCs and CCSCs.** To overcome the limits of *ex vivo* detection methods (i.e., small blood sample volume)

and increase specificity of *in vivo* CTC detection, we demonstrated, for the first time, the application of magnetic enrichment of CTCs directly in the bloodstream in combination with duplex targeting dual color detection strategy (Figure 5).<sup>13</sup> Highly NIR responsive GNTs (Figure 5C) with an absorption maximum at 900 nm and a minimum at 639 nm (Figure 6D) were coated with polyethylene glycol (PEG) and conjugated with folates. As the second NPs, 10 nm MNPs coated with PEG and amphiphilic triblock polymers were conjugated with the amino-terminal fragment (ATF) of the urokinase plasminogen activator (uPA) (Figure 5B). MNPs have an absorption in a broad NIR range; however, the absorption spectrum is different from that of GNTs (Figure 5D). Injection of cancer cells (iv,  $10^5$ ) previously labeled *in vitro* with conjugated MNPs revealed readable PA signals from mimic CTCs with ~40 to 60 min clearance. Using two-color (639 nm/900 nm) PAFC, cell injection alone followed by iv injection of NP cocktail (20:80 conjugated GNT:conjugated MNP) revealed effective labeling within ~5 min after NP injection. The detectable PA signals from CTCs that were double-labeled *in vivo* had clearance rates similar to cells labeled *in vitro*.<sup>13</sup> To detect CTCs originating from a primary tumor, MDA-MB-231 cells were inoculated subcuta-

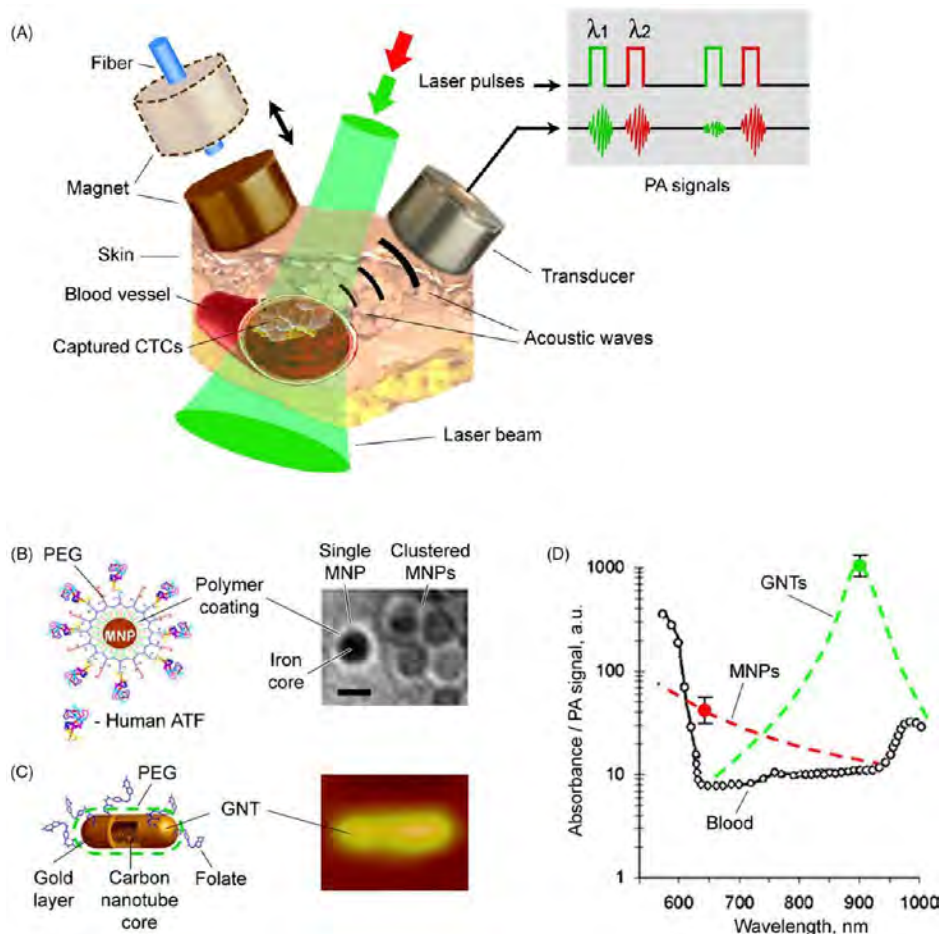
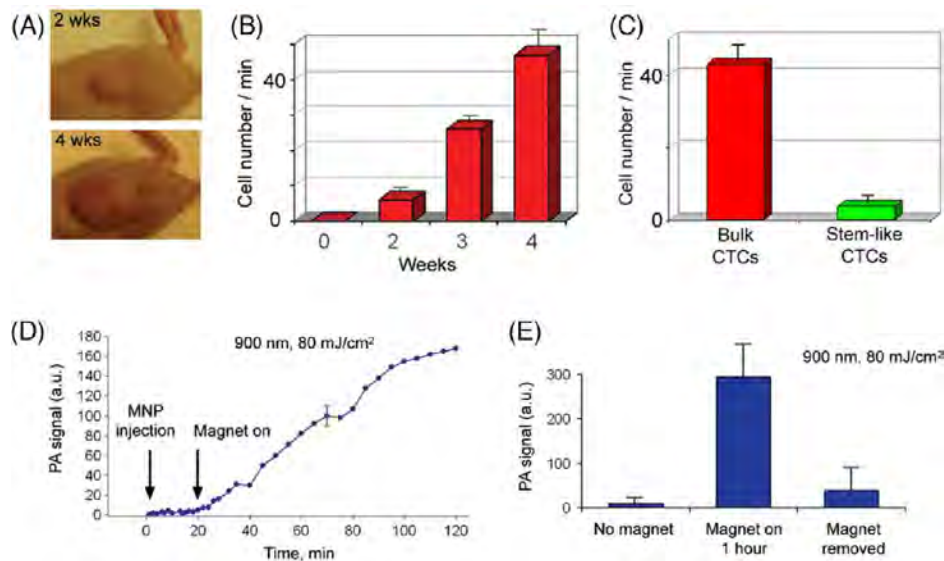


Figure 5. *In vivo* magnetic enrichment and two-color PA detection of CTCs. (A) Schematic with laser beam outside magnet or fiber-based laser delivery through the hole in magnet (dashed lines). (B) The 10 nm MNPs coated with amphiphilic triblock polymers, polyethylene glycol (PEG), and the amino-terminal fragment (ATF). (C) The 12 × 98 nm GNTs coated with PEG and folate. (D) PA spectra of ~70 μm veins in mouse ear (open circles). The average standard deviation for each wavelength is 18%. Absorption spectra of the MNPs and GNTs (dashed curves) normalized to PA signals from CTC labeled with MNPs (red circle) and GNTs (green circle). Adapted with permission from ref 13. Copyright 2009 Nature Publishing Group.



**Figure 6.** PA detection and magnetic enrichment of CTCs in tumor-bearing mice. (A) The size of the primary breast cancer xenografts at different stages of tumor development. (B) The average rate of CTCs in  $200\text{ }\mu\text{m}$  abdominal skin vein over a period of several weeks. (C) Average rate of bulk CTCs and stemlike CTCs in the abdominal skin blood vessels at week 4 of tumor development. (D) PA signals from CTCs in abdominal skin vessels obtained with fiber schematics at week 1 of tumor development before and after magnet action. The average standard deviation for each wavelength is 24%. (E) PA signals from CTCs in abdominal skin vessels before, during (3 min), and after magnetic action at week 2 of tumor development. The error bars in B, C, and E represent standard error ( $n = 3$ ). Figures were adapted with permission from (A, C) ref 15, copyright 2009 Wiley; (B, D, E) ref 13, copyright 2009 Nature Publishing Group.

neously into nude mice. At 2, 3, and 4 weeks of tumor development (Figure 6A), a cocktail of the conjugated nanoparticles (GNT-folate + MNP-ATF) was injected intravenously into the circulation. Two-color PA detection of CTCs at 20 min after injection (to allow clearance of most unbound nanoparticles) showed that the ratio of the numbers of CTCs in mouse ear to those in abdominal vessels (CTCs per min) increased from  $(0.9 \pm 0.3)/(6 \pm 2.1)$  at 2 weeks to  $(15.1 \pm 2.7)/(47 \pm 6.4)$  at 4 weeks (Figure 6B). These data approximately correlated with the stage of the primary tumor progression. Attaching a magnet with a field strength of 0.39 T at week 1 led to immediate increases in both PA signal amplitude and rate, and changed the character of the PA signal from infrequent flashes to a continuous increase of permanent PA signals up to 88-fold within 1.5 h (Figure 6D,E), indicating successful magnetic CTC capturing.<sup>13</sup> Applying this method to clinical use, patients may potentially carry a magnet attached to selected peripheral vessels (e.g., in the wrist area) for trapping of CTCs, followed by a quick PA detection of the trapped CTCs, and, if necessary, local PT treatment or removal of CTCs by using syringe-based systems for further molecular analysis.

Furthermore, *in vivo* targeting and purging of breast CTCs with a stemlike phenotype (i.e., CCSCs), which are naturally shed from the parent tumor, were performed with two color and dual modal strategy using functionalized GNTs and MNPs.<sup>15</sup> GNTs and MNPs conjugated with folic acid and antibodies to CD44 were selected for the detection of bulk and stemlike CTCs. For identification of bulk CTCs, we used markers described above. At week 4 after tumor inoculation (Figure 6A, bottom), when metastatic lesions developed in the distant organs (e.g., liver), GNT-folate and GNT-CD44 were separately injected iv through mouse tail vein at concentrations of  $10^9/\text{mL}$  in  $100\text{ }\mu\text{L}$  of PBS ( $n = 3$ ). PA monitoring of blood vessels began at 20 min after injection to allow

effective labeling of CTCs in bloodstream.<sup>11,13</sup> The average rate of flashing PA signals, which is equivalent to the cell rate (i.e., one PA signal corresponds to one cell or cell cluster crossing laser beam) after introduction of GNT-folate, was  $42.9 \pm 6.5$  cells/min. After subsequent injection of GNT-CD44, the rate of flashing PA signals increased to  $46.7 \pm 6.8$  cells/min (Figure 6C). This means that  $3.8 \pm 0.6$  cells/min or 8.8% of all detectable CTCs can be exclusively associated with stemlike subpopulation of CTCs. This study represents the first demonstration of the potential of the multifunctional PAFC/PTFC nanotheranostic platform for ultrasensitive PA molecular detection of CCSCs *in vivo*. Additional studies are needed to develop a fully validated platform. Ongoing studies in our laboratory include exploring the role of the folate receptor and adding CD24 and CD45 markers to increase detection and specificity of CCSCs and exclude possible false positive signals from leukocytes.

**In Vivo Multicolor and Multimodal Nanotheranostics of Infected Blood.** Bacterial infections are a significant cause of morbidity and mortality worldwide. In particular, multidrug resistant pathogens in the bloodstream are increasingly prevalent problems that complicate the care of many patients. The critical steps in the development of bacterial infections include their penetration into the blood system, interactions with blood cells flowing in the circulatory system or with endothelial cells, and further translocations in the host organisms. Little is known about CBC kinetics in the blood. This includes their clearance and adherence rates, which might be very important for understanding the transition from the bacteremic stage to the tissue invasive stage and for development of an effective therapy. Previously, we demonstrated the capability of the PAFC/PTFC platform to detect and kill, *in vitro*, *Staphylococcus aureus* and *Escherichia coli* labeled with gold NPs and carbon nanotubes (CNTs).<sup>35,38,39</sup> Recently, we extended this platform to include *in vivo*

magnetic enrichment, multiplex PA detection, and PT eradication of circulating *S. aureus* on the basis of the *in vivo* nanotheranostic platform developed for CTCs.<sup>2,13</sup> Bacteria were targeted directly in the bloodstream through intravenous injection of silica-coated MNPs (siMNP) and GNRs functionalized with antibodies specific for *S. aureus* protein A and lipoproteins, respectively. Both antibodies are highly expressed in *S. aureus* and absent in mammalian cells. GNRs had a maximum absorption near 820 nm. After successful two-color PA detection of targeted CBCs at low energy fluence ( $50 \text{ mJ/cm}^2$ ) of lasers at 671 and 820 nm, mice were subjected to PT therapy by 1 h laser exposure of a 300  $\mu\text{m}$  abdominal blood vessel with a laser fluence of  $0.8 \text{ J/cm}^2$  at 820 nm, coinciding with an absorption spectrum of GNRs. PT nanotherapy led to a significant decrease in the PA signal rate (Figure 7, red curve) compared to the control group (Figure

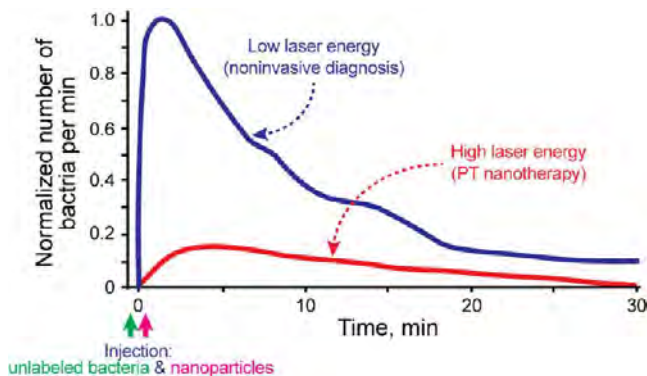


Figure 7. PA molecular diagnosis and PT targeted eradication of circulating *S. aureus* in the blood of the mouse model with real-time PA monitoring of PT nanotherapeutic efficacy. Adapted with permission from ref 2. Copyright 2012 Galanzha et al.

7, blue curve) at a laser fluence shown to be safe for blood cells. To confirm this therapeutic effect, mice were euthanized, and the blood was examined for the presence of viable bacteria. Blood from mice in the control and PA diagnostic groups showed similar bacterial growth, while the number of bacteria from the PT therapeutic group was reduced by 10-fold. This study implied that the PAFC/PTFC nanotheranostic technical platform may offer unique advantages compared to existing diagnostic and therapeutic approaches: (1) ultrahigh sensitivity ( $0.5 \text{ CFU/mL}$ ); (2) physical, PT-based destruction of bacteria, thus retaining its therapeutic efficacy irrespective of antibiotic resistance; (3) integration of multiplex PA molecular detection and PT targeted elimination of CBCs with real-time PA monitoring of therapeutic efficacy; and (4) high spectral specificity based on distinct spectral properties of NPs.<sup>2</sup> Also, the PAFC/PTFC platform has high promise for nanotheranostics of circulating parasites, such as malaria parasites, and other infected cells.

**In Vivo Dynamic Interrelations of Blood and Lymph CTCs in Preclinical Studies.** Blood and lymph vessels are common pathways for cell dissemination from one location to another through numerous anatomical interconnections between lymph vessels, lymph nodes, and blood circulatory system.<sup>41</sup> The close interrelations of blood and lymph systems can be illustrated by a simplified schematic of dissemination of CTCs in cancer (Figure 8). Logically, to understand disease progression, both lymph and blood pathways should be examined simultaneously. Nevertheless, until now, cells (e.g.,

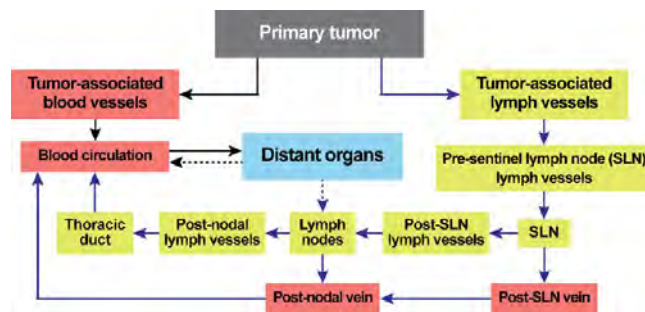


Figure 8. Pathways of CTCs from primary tumor to metastatic sites.

CTCs) in blood and lymph have been studied separately, with a particular focus on the role of blood cells. This skewed perspective cannot provide a comprehensive understanding of the mechanisms of disease development. As a result, we currently do not have the clinical capability to intervene and stop development of many diseases at early stage when well-timed treatment is most effective.

Recently, we integrated blood and lymph PAFC and demonstrated its application in combination with PA lymphography and PA cytometry of sentinel lymph node(s) (SLN; potentially first metastatic site). This platform provided real-time quantitative monitoring of blood and lymph CTCs *in vivo* and defined *in vivo* cross-correlations between lymph CTCs, blood CTCs, size of primary tumor and SLN and distant metastases.<sup>41</sup> The unprecedented sensitivity and specificity allows for the study of CTC pathways at the earliest possible stages of metastatic disease. Specifically, in a preclinical mouse melanoma model, we found that early metastatic cells in latent metastatic disease (1 week after tumor inoculation) can disseminate equally by blood and lymph pathways (Table 1). However, in a few cases, metastatic cells appeared in lymph vessels in week 1 without any cells detected in the blood vessels and vice versa. On average, over the course of two weeks, an increase in the size of a primary tumor by  $\sim 3.5$  times is associated with an increase in the quantity of lymphatic CTCs by  $\sim 10$  times, with only a small increase in blood CTCs. The number of PA signals (i.e., number of micrometastases and/or clusters of metastatic cells)<sup>14</sup> from the SLNs increased by 6.5-fold. These data showed that PAFC could clarify dynamic interrelationships of blood and lymph CTCs *in vivo* and their impact on metastasis development.

**In Vivo Nanotheranostics of Circulating Blood Clots and Other Applications.** When a blood vessel is injured, the normal physiological response of the body is clot (thrombus) formation to prevent blood loss. Alternatively, in the absence of vessel injury, a pathological condition called thromboembolism may lead to formation of circulating blood clots that can block vessels at distant locations, in particular, in peripheral veins (venous thromboembolism), lungs (pulmonary embolism), brain (embolic stroke), heart (myocardial infarction), kidney, or gastrointestinal tract. Thromboembolism is a significant cause of morbidity and mortality, especially in adults. However, little progress has been made in the development of methods for real-time detection and identification of circulating clots. Most emboli are not detected until a vessel obstruction manifests as a serious clinical event.

Commonly used *ex vivo* methods of detecting clots are time-consuming, suffer from poor sensitivity due to the small volumes of blood samples, and are limited by discrete time-

**Table 1. Correlation between Primary Tumor Size, Metastasis in SLN, and Number of Tumor Cells in Lymph and Blood Flow of Melanoma-Bearing Mice**

	tumor size (mm <sup>2</sup> )	rate of CTCs (cell/min)		no. of PA signals associated with metastasis in SLNs	histology
		lymph	CTCs		
1 week	1.0 ± 0.2	0.26 ± 0.05	0.85 ± 0.03	493	no
2 weeks	3.6 ± 0.5	2.13 ± 0.30	1.07 ± 0.05	3188	yes

point sampling with difficult access to clinically relevant sites. Most *in vivo* methods are only able to detect fixed or slowly moving large clots. Pulse Doppler ultrasound is a promising technique for the detection of circulating clots, but this technique cannot detect small clots or assess clot composition and may be affected by artifacts. To overcome these limitations, we proposed an *in vivo* PAFC for real-time detection of clots of different compositions<sup>42,43</sup> using a combination of positive and negative contrast modes. Laser irradiation of blood vessels in normal vessels creates a constant PA background determined by the absorption of RBCs randomly distributed in the irradiated volume. Depending on the size of vessels, hematocrit (Ht), and PAFC spatial resolution, the number of RBCs in the detected volume can vary from one or a few RBCs in a capillary to thousands in larger vessels. When a RBC-rich red clot passes through the irradiated blood volume, a transient increase in the local absorption, which is associated with a high concentration of hemoglobin (Hb), results in a sharp positive PA peak. Red clots can be detected when they have a higher local absorption than the normal RBC background in the detected volume. When a weakly absorbing, platelet rich white clot passes through the laser-irradiated vessel volume, a transient decrease in the local absorption results in a sharp negative PA signal. A mixed clot with both RBC-rich (i.e., high-absorbing) and platelet-rich (i.e., low-absorbing) local zones produces a pattern of positive and negative PA signals.

This phenomenological model was demonstrated in preclinical studies using the mouse model of myocardial infarction created by total ligation of left coronary artery.<sup>42</sup> The readable transient PA signals were observed with different patterns of negative, positive, and combined contrasts associated with white, red, and mixed clots, respectively, compared to no signals in normal control mice. The concentration and size of clots were measured with a threshold of a few clots with diameter of >20 μm in the entire circulation (i.e., 1–3 clots/mL in mice). This PAFC-based diagnostic platform can be used in real time defining risk factors for cardiovascular diseases, as well as for prognosis and potential prevention of stroke by using a well-timed therapy or for a clot count as a marker of therapy efficacy. Besides label-free negative contrast PA detection of clots, they can be potentially targeted by NPs (as CTCs and CBCs) and then destroyed by laser irradiation.

Moreover, NPs with enhanced PA/PT contrast properties were integrated with ultrasound contrast agent (i.e., 0.5–2 μm microbubbles) to enhance the treatment of emboli. Microbubbles were prepared according to standard manufacturer's procedure with modifications by adding absorbing NPs, i.e., CNTs, in various concentrations. PA/PT signals from microbubbles with absorbing agents were significantly higher (10–50-fold) compared to signals from microbubbles or NPs alone. In particular, for intact microbubbles, the threshold for laser-induced evaporation at 850 nm was in the range of 2–8 J/cm<sup>2</sup>, while the presence of CNTs reduced this threshold to

10–30 mJ/cm<sup>2</sup> compared to 100–200 mJ/cm<sup>2</sup> for CNTs in water at the similar concentration. Gradual increase of laser energy above evaporation threshold led to sudden nonlinear (10–30-fold) amplification of both PA and PT signals compared to NP solution alone, accompanied by microbubble degradation at high laser energy. After intravenous injection of 100 μL of microbubble solution in the concentration range of 10<sup>10</sup>–10<sup>11</sup>/mL to the mouse circulatory system, PAFC revealed quick appearance of many microbubbles with typical clearance of 3–6 min. In the developed model of mouse thrombosis, thrombi with microbubbles could be visualized *in vivo* in blood vessels. Laser irradiation of microbubbles and thrombi *in vitro* and *in vivo* using safe-for-human doses (e.g., 50–100 mJ/cm<sup>2</sup> at 1064 nm) led to the disappearance of both microbubbles and thrombi, suggesting effective destruction and clearance of thrombi.

Finally, we introduced a novel concept of a nanodrug, whose mechanism is based on synergy between physical and biological effects that are photothermally activated in NP-drug conjugates.<sup>44</sup> To prove this concept, we utilized tumor necrosis factor-alpha coated gold nanospheres (Au-TNF) heated by nanosecond laser pulses. To enhance PT nanodrug efficiency in the NIR window of tissue transparency, where nanospheres have off-resonance weak plasmonic absorption, we explored slightly ellipsoidal nanospheres and the occurrence of nanosphere clustering in tumor tissues providing red-shift in plasmonic resonances. In addition, laser-induced dynamic nanoparticle modification and nanobubble formation led to amplification and spectral sharpening of the red-shifted PT resonances. Using a murine carcinoma model, we demonstrated higher PT therapeutic efficacy of Au-TNF conjugates compared to laser and Au-TNF alone or laser with TNF-free gold nanospheres. The PT activation of low toxicity Au-TNF conjugates, which are in phase II trials in humans, with a laser approved for medical applications opens new avenues in the development of clinically relevant PT nanodrugs with synergistic antitumor action.

## ■ IN VIVO NANOTHERANOSTICS: TECHNICAL CHALLENGES

The technical challenges facing *in vivo* nanotheranostic platforms fall into one of three categories: (1) the development of suitable contrast nanoagents; (2) the identification of specific and sensitive biomarkers of abnormal circulating features; and (3) the selection of appropriate theranostic modalities. Each category is discussed in detail below.

**Development of Novel Contrast Nanoagents.** Currently, various nanoscale materials with different shapes, sizes, and compositions are available owing to recent advances in nanotechnology (Figure 9). Unique optical, magnetic, or electronic properties enable their application as imaging and therapeutic contrast agents in different theranostic modalities, including optical, PA, PT, X-ray, positron emission computed tomography (PET), computed tomography (CT), magnetic resonance imaging (MRI), ultrasound (US), etc. Particularly,

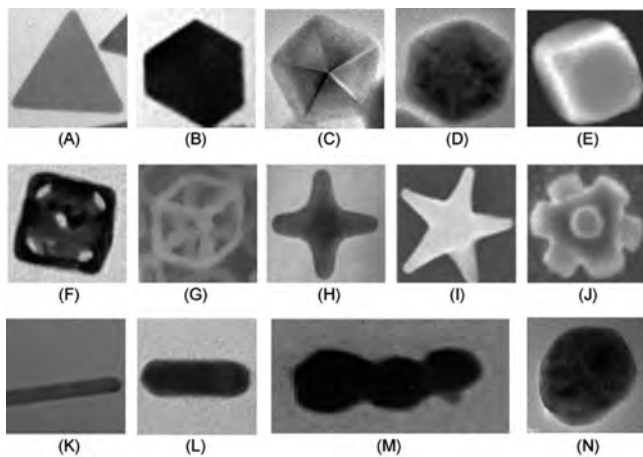


**Figure 9.** Examples of plasmonic NPs with different shapes. (A) 2D triangle.<sup>115</sup> (B) 2D truncated triangle.<sup>115</sup> (C) 3D decahedron.<sup>115</sup> (D) Hexagonal bipyramidal polygon.<sup>115</sup> (E) Cube.<sup>116</sup> (F) Nanocage.<sup>117</sup> (G) Nanoskeleton.<sup>118</sup> (H) Tetrapod.<sup>119</sup> (I) Star shape.<sup>120</sup> (J) Octapod.<sup>121</sup> (K) Nanobelt.<sup>115</sup> (L) Nanorod.<sup>122</sup> (M) Rod-shape GNT.<sup>12</sup> (N) Spherical colloid.<sup>115</sup> Figures were adapted with permission from (A–D, K, N) ref 115, copyright 2010 Royal Society of Chemistry; (E, F, M) refs 116,117,12 respectively, copyright 2007, 2009, 2009 respectively Nature Publishing Group; (G, I) refs 118,120 respectively, copyright 2009, 2008 respectively Wiley; (H, J, K) refs 119,121,122 respectively, copyright 2008, 2002, 2008 respectively American Chemical Society.

inorganic NPs of different shapes and compositions, including GNSs, GNRs, and GNTs that were tuned to desired NIR spectral ranges, have been reported, and their potential for biomedical imaging and therapy has been demonstrated.<sup>9,12,13,16,21</sup> However, there still is much room to improve the realization of NP-based multicolor, multiplex theranostics. Recent studies indicate that the NIR-responsive NPs have broad plasmonic bands, limiting their multicolor capacity.<sup>13,45,46</sup> There exists great demand for tunable plasmonic nanomaterials with narrow plasmonic bands and distinctive plasmonic signatures especially for optical imaging. With finely tuned plasmonic spectra, multispectral, multicolor, multiplex sensing and imaging is possible. Particularly, the optical tunability and responsiveness in the NIR range (i.e., ~650 to ~1,400 nm) offer promising potential for minimally invasive theranostics of diseases, including tumors and bacterial infections.<sup>2,9,12–16,21,35,38</sup> Most biological components are relatively transparent to NIR. Also NIR responsive NPs allow selective and sensitive sensing of targets in the presence of biological background materials, minimizing the sample preparation and purification time.

Other limitations of many currently available NPs are physicochemical instability, e.g., poor dispersibility in biologically relevant solutions and concerns over NPs' potential toxicity, opsonization, and bioaccumulation, which are major obstacles in translation of NPs to clinical practice. Effective targeting of the intended cells and tissues, especially diseased ones such as tumors and infections, through systemic administration of NPs or their complexes is a major challenge. NPs for nanomedicine-related theranostics typically have low clearance rates from the body and accumulate in the liver and the spleen due to their relatively large sizes (i.e., >30 nm). Recent studies showed that NPs with hydrodynamic diameters less than 5.5 nm are rapidly and efficiently excreted.<sup>47</sup> However, in general, such small NPs are not suitable as

imaging contrast agents due to their low responsiveness and poor sensitivity. Thus, there is a need for clever approaches to overcome these limitations. Lastly, for multiplex, quantitative targeting and therapy of circulating tumor cells and biomolecules, NP surfaces should be highly addressable, allowing for the functionalization of different biomarkers, such as antibodies, small RNAs, hormones, or aptamers.

#### Identification of Specific Markers of Abnormal Cells.

The identification of new biomarkers or biomarker signatures that provide both high specificity and high sensitivity for detecting abnormal circulating cells such as CTCs, CBCs, or clots in whole blood is critical to the success of *in vivo* nanotheranostics. Fortunately, bacterial specific markers, such as *S. Aureus* protein A, are well characterized and are not expressed on mammalian cells. In the case of clots, differences in size and absorbance can be used to distinguish normal cells from blood clots.<sup>42</sup> CTCs, on the other hand, are highly heterogeneous, and many CTC biomarkers are also found on normal tissues. As such, the remainder of this section focuses on challenges associated with identifying appropriate CTC markers.

As mentioned previously, our group has explored combinations of folate-conjugated and anti-CD44-conjugated GNTs as well as MNPs conjugated with ATF of uPA to detect CTCs in preclinical models.<sup>13,14</sup> The folate receptor is a promising biomarker as it is highly expressed in 90% of ovarian and endometrial cancers as well as a significant percentage of lung, kidney, breast, and uterine cancers.<sup>48–50</sup> In normal tissues with the exception of kidney, folate receptors are found on luminal surfaces of epithelial tissues and thus are shielded from the circulation.<sup>49,51</sup> Low et al. have demonstrated that intravital multiphoton microscopy can detect CTCs in tumor bearing mice injected with fluorescence-labeled folate.<sup>22</sup> Advantages of folate over tumor-specific antibodies for labeling CTCs include (1) the small size of folate (MW = 441), which allows for rapid clearance ( $t_{1/2} = 3\text{--}5$  min)<sup>22</sup> thus reducing the opportunity for nonspecific binding; and (2) the high density of folate receptors on some tumor cells allowing for more intense labeling than antibodies.<sup>52</sup> Key limitations of folate targeting are that (1) folate receptor expression is cancer- and patient-specific; and (2) folate receptors can be shed into the blood and circulate unattached from CTCs.<sup>53,54</sup>

CD44 is a receptor for hyaluronic acid. It is a commonly used marker to help identify CCSCs,<sup>55</sup> however, CD44 is ubiquitously expressed on both hematopoietic and non-hematopoietic cells. For this reason, additional markers such as CD24 and CD133 are also used in CCSC detection. While the use of multiple markers is expected to increase specificity, sensitivity will decrease.

uPA is a serine protease that regulates matrix degradation, cell invasion, and angiogenesis. The receptor for uPA (uPAR) is highly expressed in 54 to 90% of breast cancers and 86% of pancreatic cancers as well as many other cancer types.<sup>56,57</sup> uPAR is expressed at low levels in normal tissues, however, it is highly expressed on leukocytes during infection, on various tissues in various inflammatory disorders, and in wound response, which may lead to high background levels.<sup>58</sup> Another challenge posed by uPAR is that it can be secreted into the circulation and thus interfere with binding of nanotheranostics to CTCs.

Because of the limited number of studies focusing on *in vivo* CTC detection, it is useful to review some of the cell surface

biomarkers used by the various *in vitro* CTC detection schemes. The same or related markers can be adapted for *in vivo* CTC detection.

**Epithelial Markers.** Cancers of epithelial origin account for approximately 80% of all cancer diagnoses. It follows that epithelial markers have become the most common class of markers for CTC detection *in vitro*. EpCAM (CD326) is expressed by the majority of epithelial cancers and is not believed to be expressed by leukocytes or erythrocytes. However, a subset of B cells has been found to bind EpCAM-specific antibodies.<sup>59</sup> Fortunately, the use of lineage specific markers, such as CD45, can be used to exclude leukocytes. Antibodies are susceptible to nonspecific binding by Fc receptors that are expressed by monocytes and granulocytes. EpCAM-specific antibodies are used to label and enrich CTCs in the CellSearch and other *ex vivo/in vitro* assays. Interpatient and intrapatient variability of EpCAM expression is a major limitation. Comprehensive analyses of EpCAM expression in primary tumors demonstrate a high level of variability. For example, 32% of bladder cancers, 32–42% of ductal carcinomas, 41% of squamous cell carcinomas of the cervix, vagina, and vulva, 71% of hormone refractory prostate cancers, 73% of ovarian cancers, 78% of pancreatic adenocarcinomas, and 81% of colon adenocarcinomas were positive for EpCAM.<sup>60,61</sup>

Cytokeratins (CKs), intermediate cytoskeletal filaments found in the cytoplasm of epithelial cells, are another epithelium marker frequently used to identify CTCs. In particular, expression of CK 8, CD 18, and/or CK 19 has been linked with various epithelial cancers. CK expression is highly variable and less specific than EpCAM expression. In fact, the percentage of CK positive cells in healthy individuals ranges from 0% to 20%.<sup>62,63</sup> Furthermore, because CKs are primarily located in the cytoplasm, CTC detection using CKs requires cell permeabilization and fixation that are impractical for *in vivo* studies. Current CTC detection methods that utilize EpCAM for enrichment and CK markers for identification fail to detect CTCs in 43–80% of patients with metastatic disease.<sup>64</sup>

Disadvantages of using epithelial markers to detect CTCs are 3-fold. First and foremost, epithelial-mesenchymal transition (EMT) is cited as a likely, if not common, mechanism of metastasis.<sup>1,65</sup> Cells undergoing EMT downregulate epithelial markers such as EpCAM and CK while upregulating mesenchymal markers such as vimentin, N-cadherin, and fibronectin. In fact, micrometastatic deposits isolated from the bone marrow of breast cancer patients were found to completely lose epithelial CK expression in favor of vimentin. Cells that have lost epithelial characteristics in favor of a more invasive mesenchymal phenotype are thought to have a better chance of surviving in circulation and extravasating to form a metastatic lesion. These cells which have a higher metastatic potential are excluded by CTC detection methods considering only epithelial markers.<sup>66</sup>

Second, epithelial cells that lose cell-to-cell contact typically undergo apoptosis: a process called anoikis. As such, the vast majority of epithelial CTCs may be destined for apoptosis and clearance. This assumption seems to agree with Fidler's estimate that only about 0.01% of CTCs result in a metastatic lesion. Since each gram of tumor sheds about  $1 \times 10^6$  cells into the circulation per day,<sup>67,68</sup> detection of CTCs by epithelial markers may be better suited to assess overall tumor burden than metastatic potential.

The third disadvantage of epithelial markers is that peripheral blood is routinely contaminated with normal epithelial cells that have entered the circulation due to tissue trauma, noncancerous inflammation, or iatrogenic procedures.<sup>6,69</sup> The use of epithelial markers alone, therefore, may overestimate the prevalence of CTCs.

**Tumor-Associated Markers.** Human Epidermal Growth Factor Receptor 2 (HER2) is a biomarker for breast cancer where it is overexpressed in approximately 30% of patients and associated with a more aggressive phenotype. HER2 is also overexpressed in ovarian, uterine, and gastrointestinal malignancies. While HER2 has been used to detect CTCs, several studies have shown differences in HER2 expression between a primary tumor and CTCs. Specifically, HER2<sup>+</sup> CTCs have been found in patients with HER2<sup>+</sup> breast cancer<sup>70</sup> and HER2<sup>+</sup> CTC in patients with HER2<sup>-</sup> primary tumors.<sup>71–73</sup>

While prostate specific antigen (PSA) is the standard biomarker for prostate cancer, anti-PSA antibodies have been found to bind to monocytes.<sup>63</sup> Fortunately, prostate specific membrane antigen (PSMA) has proven to be a more useful marker for the detection of CTCs *in vitro*.<sup>74</sup>

Carcinoembryonic antigen (CEA) and mucin 1 (MUC1) are glycoproteins that are overexpressed in a wide range of malignancies. Both CEA<sup>75,76</sup> and MUC1<sup>77</sup> have been used to detect CTCs in cancer patients. The shedding of both glycoproteins into the circulation complicates their use for *in vivo* detection.

**Stem Cell Markers.** Regardless of whether or not CCSCs are truly "stem" cells or simply more aggressive, tumor initiating cells, the identification of this population is important for both cancer prognosis and treatment. A number of studies have isolated cancer stem or stemlike cells from clinical samples. A single definitive marker for cancer stem cells has yet to be identified for any cancer type. As such, recent studies have focused on the discovery of rare subsets expressing multiple markers. Human breast carcinoma cells that were CD44<sup>+</sup>CD24<sup>-/low</sup> Lineage<sup>-</sup> exhibited enhanced tumorigenicity consistent with a stemlike cancer cell.<sup>25</sup> CD44<sup>-</sup>CD24<sup>-</sup>CD326<sup>+</sup> cells were recently identified as a novel subpopulation of pancreatic cancer tumor initiating cells.<sup>78</sup> CD133<sup>+</sup> colon adenocarcinoma cells were found to be responsible for tumor initiation,<sup>79</sup> whereas CD44<sup>+</sup>CD24<sup>+</sup>CD133<sup>+</sup> breast cancer cells were found to be highly tumorigenic and drug resistant.<sup>80</sup>

**Mesenchymal Markers.** EMT is cited as a likely, if not common, mechanism of metastasis. As mentioned previously, epithelial markers, e.g., EpCAM, CK, and E-cadherin, are downregulated during EMT while mesenchymal markers, e.g., N-cadherin, vimentin, and fibronectin, are upregulated. However, relatively few studies have investigated mesenchymal markers on the surfaces of CTCs compared to the wealth of studies using epithelial markers. A recent study has identified a subset of CTCs expressing a mesenchymal phenotype, i.e., vimentin<sup>+</sup> N-cadherin<sup>+</sup>, in patients with squamous cell carcinoma of the head and neck.<sup>81</sup> In lung cancer patients, vimentin was expressed on a fraction of CTCs but the majority of cells in circulating tumor microemboli (CTM).<sup>82</sup> CTM are multicellular aggregates of tumor cells that likely have survival and proliferative advantages in establishing metastases.<sup>82,83</sup>

**Endothelial Markers.** There are also known progenitor cells of the endothelial lineage circulating to different extents in

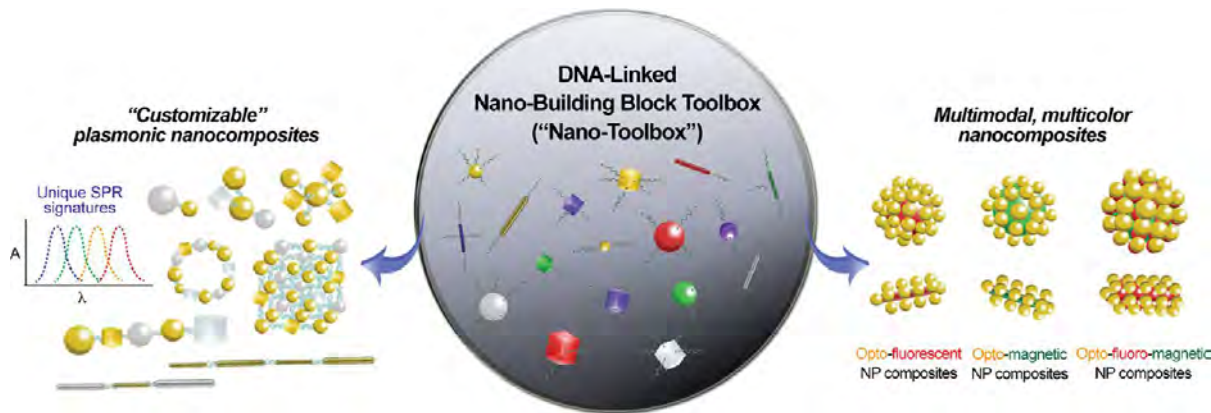


**Figure 10.** Schematic of a nano-building block toolbox (nanotoolbox) for programmable self-assembly of multifunctional nanostructures with arbitrary shapes and functions, and examples of applications of self-assembled multifunctional nanocomposites with shapes, sizes, and functions that are “programmable/customizable” on the basis of the target applications.<sup>98</sup> Customizable plasmonic nanomaterials with distinct plasmonic signatures using metallic NP building blocks of various sizes and shapes (left). Multimodal, multicolor contrasting nanoagents through controlled integration of heterogeneous multiple discrete NP building blocks with various sizes and shapes into single multifunctional nanoscale architectures with predefined characteristics (right). The nanocomposite’s surface is addressable, allowing for the multiplex functionalization of different biomolecules, including antibodies, small RNAs, aptamers, hormones, etc. Figures were adapted with permission from refs 98,104, copyright 2012 and 2011 respectively Wiley.

normal and cancer-bearing patients. There has been an increasing implication of progenitor cell contribution to neovascularization processes in the body, including tumor growth.<sup>84–90</sup> Further evidence has suggested that endostatin or other inhibitors of angiogenesis perturbs mobilization of these cells.<sup>89,91–93</sup> We have been investigating the proangiogenic activity and radiation biology of circulating endothelial progenitors using blood outgrowth endothelial cells (BOEC). BOEC, which are endothelial cell precursors, are isolated from human peripheral blood and grown in culture. After multifold expansion these cells express several endothelial protein markers: VE Cadherin (VEC), von Willebrand factor (vWF), PECAM (CD31), and P1H12.<sup>87</sup> Our preliminary results show that injection of these cells can augment the rate of tumor growth, improve tumor oxygenation, and modify radiation response (manuscript in submission). This indicates that existing endothelial progenitors in the circulation may be a significant factor in tumor vascularization, growth, environment, and treatment response. These novel discoveries point to the possibility that progenitor cells are a target for antiangiogenesis strategies and are involved in the response of tissue to treatment related damage (radiation or chemotherapy).<sup>94</sup> Therefore, attempts to determine the degree to which theranostic nanomedicine approaches can control or inhibit populations of circulating endothelial cells are warranted.

**Selection of Appropriate Theranostic Modalities.** MRI, PET, CT, US, X-ray, Raman scattering, fluorescence optical imaging, and laser-induced PA and PT imaging are among the theranostic modalities available in the clinic. The selection of the proper modality for accurate and reliable diagnostic imaging is a considerable task that clinicians confront. Each modality has pros and cons in terms of sensitivity, spatial and temporal resolution, and imaging depth.<sup>95–98</sup> For example, modalities with high sensitivity, such as optical imaging and PET, have comparatively inadequate resolution; however, those with high resolution, such as CT and MRI, possess relatively low sensitivity. The integration of multiple imaging modalities has gained interest to realize more accurate and reliable diagnostics. Although

there are clear merits of combining multiple modalities in tandem, they should be selected rationally through careful considerations of characteristics of each modality, so that they may compensate for the deficits of each individual modality to maximize their synergistic effects.<sup>96</sup> One such example would be the integration of PET or optical imaging with high sensitivity with MRI or CT with high spatial resolution. Furthermore, most of the modalities require exogenous contrast agents to improve the signal-to-noise ratio. The amount of different contrast agents required for multiple modalities with different resolutions and sensitivities can be a problem. Nanoagents that contain multiple functionalities, such as optical plasmon resonance, photoluminescence, magnetism, etc., would offer distinct advantages.<sup>96–98</sup> Such multifunctional nanoagents could be detected by multiple imaging modalities, significantly improving their performance in theranostics and facilitating the early detection of tumors. Also the use of a single contrast agent warrants consistent and reproducible pharmacokinetics and targeting specificity for each diagnostic modality. Moreover, the single multimodal probe could reduce the problems related to sequestration in the liver as well as toxicity issues by minimizing the total amount of contrast agent administered for the multiple imaging modalities.<sup>96,98</sup> Despite the promises, the controlled synthesis of rationally designed multifunctional contrast nanoagents remains very challenging.

## ■ STRATEGIES AND FUTURE PERSPECTIVES

Here we outline strategies to overcome existing challenges and facilitate further development of *in vivo* nanotheranostics. A vision for future clinical application of these technologies is also presented.

**Multifunctional Theranostic Contrast Nanoagents.** There has been considerable interest in development of multifunctional nanocomposites with defined shapes and sizes that incorporate diverse nanocomponents.<sup>95–98</sup> The use of various types of NPs with unique physicochemical properties would enable us to develop multimodal nanoagents, with which multiple tasks and functionalities could be performed sequentially or simultaneously.<sup>98</sup> This strategy

would allow us to obtain more comprehensive, accurate, and reliable information by coupling the complementary abilities of different imaging and therapeutic modalities.

The assembly of these nanocomposites can be driven by DNA, owing to its unique molecular recognition properties, structural features, and ease of manipulation. In fact, DNA-driven self-assembly has demonstrated the potential to program matter at a molecular scale for the generation of new material properties.<sup>98–101</sup> Like DNA, RNA could self-assemble to synthesize various nanostructures that could assemble into NPs with desirable functionalities.<sup>102,103</sup> However, the accurate, scalable, and high-rate assembly of heterogeneous nanocomponents into multifunctional nanostructures with specifically designed shapes and sizes remains difficult to achieve.

The site-specific functionalization of multiple strands of DNA or RNA to the NP surface in a well-defined and stoichiometric manner is a prerequisite to control the spatial arrangement of NPs in the nanostructures.<sup>98</sup> NP building blocks with control over DNA or RNA number and geometric configuration on their surface would realize enhanced control over the shape and function of final self-assembled structures. Recently, Kim et al.<sup>104,105</sup> reported a novel anisotropic monofunctionalization strategy to place different number of DNA linkers on a NP at specific angles to each other and to synthesize NP building blocks with well-defined arrangements of DNA in all three dimensions (Figure 10).<sup>98,104</sup> Also this technology could incorporate NPs of different composition. Such well-defined and controlled functionality and directionality of various NP building blocks promise precisely controlled manufacture of structures with greater complexity for “customized” size, shape, and functionality. Engineering the sizes and structural configurations of nanocomposites offers exciting possibility to customize plasmonic nanomaterials (Figure 10).<sup>98</sup> Geometric factors, such as shape and size, and material compositions influence the optical properties, such as extinction and scattering spectra, of nanomaterials.<sup>98</sup> Hence, the self-organization of metallic NPs of various sizes and shapes into desired patterns and geometries could realize enhanced optical response over several wavelength bands. With multiple nanocomposites of finely tuned plasmonic spectra, multispectral, multicolor imaging is possible. In addition, the length of the DNA linkers could control the spacing between NPs, leading to dramatic increases in the sensitivity by controlling the plasmonic interactions between adjacent NPs.<sup>98</sup> This would realize highly selective and sensitive theranostics by matching the nanocomposites’ plasmonic spectra and resonant laser wavelengths. Furthermore, the controlled integration of various types of NPs would open another significant possibility of multimodal theranostics. Combining the useful functionalities of different NPs in a single nanostructure would allow new multiple complementary imaging modes for faster, more efficient, more accurate prognosis. Nonetheless, to realize such promising applications, we should be able to control the interactions among NPs with different functionalities, such as electronic, magnetic, and optical. With the DNA-programmable building blocks of different NPs, the NP spacing could be accurately tuned by modulating the DNA lengths to minimize their negative interactions, such as the long-standing problems of the fluorescence quenching of fluorophores and quantum dots by metallic NP surface,<sup>106,107</sup> promote enhanced new properties, and achieve desired multifunctionalities. The

functionality of self-assembled nanocomposites can also be tuned by controlling their shape and size as well as thickness of each NP layer. Moreover, the nanocomposite’s surface is addressable. DNA sequences on the outer layer of the nanocomposite can serve as specific anchor points for incorporating multiple biorecognition units. This enables highly selective and controllable attachment of various recognition units, such as antibodies, small RNAs, hormones, and aptamers, allowing multiplex quantitative targeting and therapy to be possible. The successful merger of desirable functionalities of various NPs in a controlled manner should enable us to realize highly sensitive, multiplex, multicolor nanotheranostics for circulating tumor cells and pathological biomolecules with multiple complementary modalities beyond the inherent limitations of individual existing technologies.<sup>98</sup> Of note is that RNA could provide similar attributes of DNA in the nanostructure self-assembly with a distinctive advantage. RNA could be designed and manipulated with a similar level of simplicity as DNA to produce a variety of different nanostructures. RNA possess catalytic functions similar to proteins and their nanostructures, such as small interfering RNA (siRNA), microRNA (miRNA), RNA aptamers and ribozymes, demonstrating promise for theranostics of cancers and infections.<sup>102</sup> Hence, the polyvalent nature of RNA nanostructures and their incorporation in the NP-building block technology not only could provide a new tool for the theranostics of metastatic cells but also could lead to developing noble strategies for *in vivo* multifunctional nanotheranostics.

In addition, Zharov et al. recently discovered ultrasharp PA/PT resonances in plasmonic NPs with a spectral width down to 0.8 nm (i.e., 100-fold narrower than linear absorption spectra).<sup>44,45</sup> This would offer another promising way to overcome the challenges related to the relatively broad absorption bands of PA/PT contrast agents (e.g., 60–150 nm for GNRs or GNSs), which limit their multicolor capacity (i.e., restrict them to only two simultaneous colors).<sup>9,13,45,46</sup> The physical mechanism underlying these phenomena is based on multistage signal behaviors as energy fluence ( $E$ ) increases: (1) a linear increase at low fluence,  $E^n$  ( $n \approx 1$ ), (2) strong nonlinear nanobubble-associated 10–100-fold signal amplification ( $n \approx 2–5$ ), (3) signal saturation ( $n \approx 0–0.5$ ), and (4) further enhanced or inhibited signal depending on NP type. Thus, a shift of the laser wavelength toward the absorption center leads to increased energy absorption, raising the temperature above the well-defined nanobubble-formation threshold and accompanied by a significant (10–100-fold) signal amplification. As a result, spectrally dependent signal amplification led to the sharpening of PT resonances only near the centers of absorption peaks. Higher laser energy above the nanobubble threshold nonlinear spectral resonances can be red-shifted from the linear absorption spectra. This approach made it possible to easily identify each GNR in a mixture of 7 GNRs with nearly overlapping longitudinal plasmon resonances, which were hardly distinguishable by conventional absorption spectra. Thus, up to 6–8 multicolor functionalized NPs whose nonlinear spectra do not overlap in the window of tissue transparency (650–1,100 nm) can be used to simultaneously target 6–8, and potentially more, biomarkers.

Furthermore, self-assembled nanocomposites could alleviate concerns regarding bioaccumulation and potential toxicity of NPs. The NP building blocks could be very small, on the order of  $\sim 3$  nm.<sup>104</sup> The assembly is driven by DNA, a

biodegradable biopolymer. When structures are together, the self-assembled nanocomposites can be large enough to be effective theranostic contrast nanoagents; however, the structural building blocks are small enough to be effectively cleared from the body when disassembled by, for example, DNA denaturation through localized laser-induced heating or eventual nuclease-driven DNA digestion/biodegradation.<sup>98</sup>

Also, the addressable nanocomposite surface could offer ways to avoid clearance to the liver and spleen by macrophages after intravenous injection. The fates of foreign NPs and their composites in blood depend upon their physicochemical properties, including size, shape, and surface chemistry.<sup>108,109</sup> Modulating the geometric configurations and surface characteristics suggests opportunities to overcome the hurdle and considerably prolong blood circulation times, which is particularly important for effective theranostics of circulating tumor-associated cells and biomolecules. Biocompatible and opsonin resistant moieties, such as biological and chemical ligands like dextran sulfate and polyethylene glycol,<sup>110–112</sup> can be site-specifically attached to the self-assembled nanocomposite surface to shield them from opsonization and ensure their prolonged circulation. In addition, there exist many biological particles, such as blood cells and pathogenic bacteria, that have evolved to evade opsonins. Using lessons from nature, the design and construction of nanocomposites with particular shapes and surface characteristics may permit us to similarly avoid opsonization and premature clearance of nanotheranostics.<sup>98</sup> Taken together, the ability to engineer nanocomposites through self-assembly with DNA-linked NP building blocks promises to enable realization of *in vivo* nanotheranostic platforms with multicolor and multimodal capability and their translation into clinical practice.

**CTC Markers and the Biology of Metastasis.** The success of *in vivo* CTC nanotheranostics will hinge upon the specificity of CTC markers. Given the heterogeneous expression of CTC markers in different types and stages of cancer as well as inter- and intrapatient variability, it is clear that a single CTC marker or even a single class of markers will be insufficient to provide a complete account of CTCs. Furthermore, current *in vivo* and *in vitro* CTC detection technologies are susceptible to high false-positive rates due to nonspecific binding and high false-negative rates due to loss of marker expression.

Multimodal *in vivo* nanotheranostics can be developed to overcome these challenges by developing a set of CTC markers that can be imaged simultaneously. For example, folate, anti-vimentin, anti-CD44, anti-EpCAM and anti-CEA can be conjugated to unique contrast agents (e.g., self-assembled multifunctional nanocomposites) and imaged at different wavelengths. Such an approach would provide more information about the heterogeneity of CTCs and may help identify CTC subsets with higher metastatic potential.

Fidler's estimate that only 0.01% of CTCs result in a metastatic lesion<sup>28</sup> indicates that the vast majority of CTCs have no role in metastasis. A key question to be addressed is whether the 0.01% represents a unique phenotype. It has been postulated that metastasis is a rare event because it demands a cell endowed with many capabilities: a "decathlon champion".<sup>29</sup> One expects such a cell to have a unique phenotype and that the standard EpCAM<sup>+</sup>CK<sup>+</sup> signature of a CTC will not fit. The use of different classes of markers, e.g., tumor-

associated, mesenchymal, stem cell etc., would be better suited for the detection of a "decathlete" cell.

Multifunctional *in vivo* nanotheranostics will also allow us to study rare CTC subsets in greater detail. For example, MNPs can be used to capture CTCs *in vivo*<sup>13</sup> prior to extraction via minimally invasive surgery or fine-needle aspiration. Extracted CTCs can then be characterized *in vitro* through gene expression analyses or functional assays.

**Opportunity for Synergy with Targeted Therapeutics Delivery.** The programmable self-assembly of nanocomposites with DNA- or RNA-NP building blocks may offer a clever way to achieve highly targeted drug delivery that maximizes therapeutic efficacy while minimizing side effects. The NP nanostructure could be designed and assembled to be drug-delivery vesicles, for example, with 3D shapes with hollow cores to carry pharmacologically active agents. These nanovesicles can be programmed to be responsive to specific stimuli for the controlled release of drugs. For instance, if a part of the nanostructure were composed of a particular type of NPs that uniquely responded to a particular resonant laser wavelength yet the other NPs in the rest of the structure did not, localized laser-induced heating could selectively denature DNA linkages and cause a specific release of drug. Also DNA sequences of a specific part of the structure could be designed so that it may open by strand displacement with particular DNA oligonucleotide inputs.<sup>113</sup> This would enable delivery of toxic agents in a highly programmable manner, alleviating the limitations of conventional drug therapy by substantially reducing the drug doses as well as drug toxicity, yet maximizing its therapeutic efficacy. Since these drug carriers are constructed on the basis of the same assembly technology as the aforementioned multifunctional nanocomposites, they should seamlessly integrate into the *in vivo* multimodal nanotheranostic platform.

Recently, we have found that an antiangiogenic peptide (named anginex) increases tumor sensitivity to radiation in animal models due to its antiangiogenic properties by binding to galectin-1 on the cell surface.<sup>114,123</sup> In addition, we observed that anginex treatment iv blunts the angiogenic effects of CECs injected into mice early in tumor growth, resulting in smaller tumors. After introducing exogenous CECs, we have found that tumors consistently grow to larger sizes. When the growth rates of tumors exposed to exogenous CECs were compared to those treated with both CECs and the antiangiogenic peptide, we observed that the antiangiogenic effects are exerted through a pathway that includes blocking at least part of the activity/viability of CECs. *In vitro* studies have shown that peptide alone decreases the number of surviving CEC colonies after a 4 h exposure by about 20%. Importantly, we also noted an increased sensitivity to ionizing radiation in CECs pretreated with the peptide, with a decrease of CEC viability of nearly 90% in the combination treatment group. These results suggest that targeting the CECs with a peptide conjugated to a nanoprobe may allow efficient targeting and destruction by our *in vivo* PAFC and PTFC strategies. In addition, we may be able to sensitize these CECs or other malignant cells to other therapies by administering multifunctional nanoprobes, such as NP nanoarchitectures "customized" with desired size, shape and functionality using our "enabling" DNA-programmable NP building block technology.

## CONCLUSION

Early detection increases the probability of successful treatment of all diseases: from cancers to cardiovascular disorders to bacterial infections. Recent technological advances have sparked interest in the early detection of harbingers of disease, such as CTCs, CECs, CCSCs, CBCs and circulating blood clots, in the cardiovascular and lymphatic circulations. As outlined in this review, *in vivo* nanotheranostic platforms have a number of key advantages in this regard. *In vivo* detection techniques allow for interrogation of the entire blood volume of the patient, thus increasing the probability of detecting rare events. The use of nanotheranostics *in vivo* also permits continuous monitoring of physiology. Lastly, the development of multifunctional contrast nanoagents provides opportunities for simultaneous detection and purging of circulating features via multiple modalities. In particular, substantial progress has been made with *in vivo* real-time PAFC/PTFC nanotheranostics. These platforms are capable of integrating magnetic enrichment, multispectral PA detection and PT therapy with a potential for multiplex targeting of diverse biomarkers. These platforms are also clinically relevant given that (1) low toxicity NPs are used as contrast agents and (2) diagnostic lasers for PAFC/PTFC not only are used at safe fluence levels but also penetrate deeply in biological tissues.

Despite recent progress, several challenges must be overcome before *in vivo* nanotheranostics reach their full clinical potential. Continued exploration of contrast nanoagents must find spectrally distinct NPs that avoid opsonization and liver/spleen accumulation. Unique complexes of NPs, e.g., “customizable” NP nanocomposites self-assembled by our programmable DNA/RNA-NP building block toolbox technology, which respond to multiple modalities as well as deliver therapeutic agents or local hyperthermia, are a particularly fertile area of exploration. Separately, more specific biomarkers are needed to overcome high background noise in highly complex whole blood as well as inter- and intrapatient heterogeneity. Finally, the appropriate selection or development of multiple imaging modalities must coincide with multifunctional features of contrast nanoagents.

If these challenges are met, the presented innovative PA and PT technological platforms with “programmable/customizable” multifunctional nanoagents may catalyze a paradigm shift in medicine from the treatment of symptomatic disease to the application of therapeutic interventions before symptoms appear to preserve normal function and decrease morbidity.

## AUTHOR INFORMATION

### Corresponding Author

\*J.-W.K.: Tel: +1-479-575-2351. Fax: +1-479-575-2846. E-mail: jwkim@uark.edu. V.P.Z.: E-mail: ZharovVladimirP@umas.edu.

### Notes

The authors declare no competing financial interest.

## ACKNOWLEDGMENTS

This work was supported in part by National Science Foundation grants (CMMI 1235100, ECCS 1137948 and 11228660, and DBI 0852737), National Institutes of Health grants (R01EB000873, R01CA131164, R01EB009230, R01CA44114, R21CA139373 and K22CA131567), Department of Defense grants (W88XWH-10-2-0130, W81XWH-11-

1-0123 and W81XWH-11-1-0129), and the Arkansas Biosciences Institute. The authors thank Min Kim and Jeong-Min Lim for their assistance in image processing.

## REFERENCES

- (1) Chaffer, C. L.; Weinberg, R. A. A perspective on cancer cell metastasis. *Science* **2011**, *331*, 1559–64.
- (2) Galanzha, E. I.; Shashkov, E.; Sarimollaoglu, M.; Beenken, K. E.; Basnakian, A. G.; Shirliff, M. E.; Kim, J.-W.; Smeltzer, M. S.; Zharov, V. P. *In vivo* magnetic enrichment, photoacoustic diagnosis, and photothermal purging of infected blood using multifunctional gold and magnetic nanoparticles. *PLoS One* **2012**, *7*, e45557.
- (3) Pantel, K.; Alix-Panabieres, C. Circulating tumour cells in cancer patients: challenges and perspectives. *Trends Mol. Med.* **2010**, *16*, 398–406.
- (4) Yu, M.; Stott, S.; Toner, M.; Maheswaran, S.; Haber, D. A. Circulating tumor cells: approaches to isolation and characterization. *J. Cell Biol.* **2011**, *192*, 373–82.
- (5) Alix-Panabieres, C.; Schwarzenbach, H.; Pantel, K. Circulating tumor cells and circulating tumor DNA. *Annu. Rev. Med.* **2012**, *63*, 199–215.
- (6) Paterlini-Brechot, P.; Benali, N. L. Circulating tumor cells (CTC) detection: clinical impact and future directions. *Cancer Lett.* **2007**, *253*, 180–204.
- (7) Maheswaran, S.; Haber, D. A. Circulating tumor cells: a window into cancer biology and metastasis. *Curr. Opin. Genet. Dev.* **2010**, *20*, 96–9.
- (8) Zhe, X.; Cher, M. L.; Bonfil, R. D. Circulating tumor cells: finding the needle in the haystack. *Am. J. Cancer Res.* **2011**, *1*, 740–51.
- (9) de la Zerda, A.; Kim, J.-W.; Galanzha, E. I.; Gambhir, S. S.; Zharov, V. P. Advanced contrast nanoagents for photoacoustic molecular imaging, cytometry, blood test and photothermal theranostics. *Contrast Media Mol. Imaging* **2011**, *6*, 346–69.
- (10) Hughes, A. D.; King, M. R. Nanobiotechnology for the capture and manipulation of circulating tumor cells. *WIREs Nanomed. Nanobiotechnol.* **2012**, *4*, 291–309.
- (11) Galanzha, E. I.; Zharov, V. P. Photoacoustic flow cytometry. *Methods* **2012**, *57*, 280–96.
- (12) Kim, J.-W.; Galanzha, E. I.; Shashkov, E. V.; Moon, H.-M.; Zharov, V. P. Golden carbon nanotubes as multimodal photoacoustic and photothermal high-contrast molecular agents. *Nat. Nanotechnol.* **2009**, *4*, 688–94.
- (13) Galanzha, E. I.; Shashkov, E. V.; Kelly, T.; Kim, J.-W.; Yang, L.; Zharov, V. P. *In vivo* magnetic enrichment and multiplex photoacoustic detection of circulating tumour cells. *Nat. Nanotechnol.* **2009**, *4*, 855–60.
- (14) Galanzha, E. I.; Kokoska, M. S.; Shashkov, E. V.; Kim, J.-W.; Tuchin, V. V.; Zharov, V. P. *In vivo* fiber-based multicolor photoacoustic detection and photothermal purging of metastasis in sentinel lymph nodes targeted by nanoparticles. *J. Biophotonics* **2009**, *2*, 528–39.
- (15) Galanzha, E. I.; Kim, J.-W.; Zharov, V. P. Nanotechnology-based molecular photoacoustic and photothermal flow cytometry platform for in-vivo detection and killing of circulating cancer stem cells. *J. Biophotonics* **2009**, *2*, 725–35.
- (16) Zharov, V. P.; Kim, J.-W.; Curiel, D. T.; Everts, M. Self-assembling nanoclusters in living systems: application for integrated photothermal nanodiagnosis and nanotherapy. *Nanomedicine* **2005**, *1*, 326–45.
- (17) Nie, S.; Xing, Y.; Kim, G. J.; Simons, J. W. Nanotechnology applications in cancer. *Annu. Rev. Biomed. Eng.* **2007**, *9*, 257–88.
- (18) De, M.; Ghosh, P. S.; Rotello, V. M. Applications of Nanoparticles in Biology. *Adv. Mater.* **2008**, *20*, 4225–41.
- (19) Lee, S. E.; Lee, L. P. Biomolecular plasmonics for quantitative biology and nanomedicine. *Curr. Opin. Biotechnol.* **2010**, *21*, 489–97.

- (20) Giljohann, D. A.; Seferos, D. S.; Daniel, W. L.; Massich, M. D.; Patel, P. C.; Mirkin, C. A. Gold nanoparticles for biology and medicine. *Angew. Chem., Int. Ed.* **2010**, *49*, 3280–94.
- (21) Lal, S.; Clare, S. E.; Halas, N. J. Nanoshell-enabled photothermal cancer therapy: impending clinical impact. *Acc. Chem. Res.* **2008**, *41*, 1842–51.
- (22) He, W.; Wang, H.; Hartmann, L. C.; Cheng, J. X.; Low, P. S. In vivo quantitation of rare circulating tumor cells by multiphoton intravital flow cytometry. *Proc. Natl. Acad. Sci. U.S.A.* **2007**, *104*, 11760–5.
- (23) Georgakoudi, I.; Solban, N.; Novak, J.; Rice, W. L.; Wei, X.; Hasan, T.; Lin, C. P. In vivo flow cytometry: a new method for enumerating circulating cancer cells. *Cancer Res.* **2004**, *64*, 5044–5047.
- (24) Bonnet, D.; Dick, J. E. Human acute myeloid leukemia is organized as a hierarchy that originates from a primitive hematopoietic cell. *Nat. Med.* **1997**, *3*, 730–7.
- (25) Al-Hajj, M.; Wicha, M. S.; Benito-Hernandez, A.; Morrison, S. J.; Clarke, M. F. Prospective identification of tumorigenic breast cancer cells. *Proc. Natl. Acad. Sci. U.S.A.* **2003**, *100*, 3983–8.
- (26) Chiang, A. C.; Massague, J. Molecular basis of metastasis. *N. Engl. J. Med.* **2008**, *359*, 2814–23.
- (27) Ailles, L. E.; Weissman, I. L. Cancer stem cells in solid tumors. *Curr. Opin. Biotechnol.* **2007**, *18*, 460–6.
- (28) Fidler, I. J. Metastasis: quantitative analysis of distribution and fate of tumor embolilabeled with 125 I-5-iodo-2'-deoxyuridine. *J. Natl. Cancer Inst.* **1970**, *45*, 773–82.
- (29) Fidler, I. J. The pathogenesis of cancer metastasis: the ‘seed and soil’ hypothesis revisited. *Nat. Rev. Cancer* **2003**, *3*, 453–8.
- (30) Nedosekin, D. A.; Sarimollaoglu, M.; Galanzha, E. I.; Sawant, R.; Torchilin, V. P.; Verkhusha, V. V.; Ma, J.; Frank, M. H.; Biris, A. S.; Zharov, V. P. Synergy of photoacoustic and fluorescence flow cytometry of circulating cells with negative and positive contrasts. *J. Biophotonics* **2013**, DOI: 10.1002/jbio.201200047(in press).
- (31) Zharov, V. P.; Galanzha, E. I.; Tuchin, V. V. Photothermal imaging of moving cells in lymph and blood flow in vivo. *Proc. SPIE* **2004**, *5320*, 185. DOI: 10.1117/12.532107.
- (32) Galanzha, E. I.; Shashkov, E. V.; Spring, P. M.; Suen, J. Y.; Zharov, V. P. In vivo, noninvasive, label-free detection and eradication of circulating metastatic melanoma cells using two-color photoacoustic flow cytometry with a diode laser. *Cancer Res.* **2009**, *69*, 7926–34.
- (33) Nedosekin, D. A.; Sarimollaoglu, M.; Ye, J. H.; Galanzha, E. I.; Zharov, V. P. In vivo ultra-fast photoacoustic flow cytometry of circulating human melanoma cells using near-infrared high-pulse rate lasers. *Cytometry, Part A* **2011**, *79*, 825–33.
- (34) Sarimollaoglu, M.; Nedosekin, D. A.; Simanovsky, Y.; Galanzha, E. I.; Zharov, V. P. In vivo photoacoustic time-of-flight velocity measurement of single cells and nanoparticles. *Opt. Lett.* **2011**, *36*, 4086–8.
- (35) Zharov, V. P.; Galanzha, E. I.; Shashkov, E. V.; Kim, J.-W.; Khlebtsov, N. G.; Tuchin, V. V. Photoacoustic flow cytometry: principle and application for real-time detection of circulating single nanoparticles, pathogens, and contrast dyes *in vivo*. *J. Biomed. Opt.* **2007**, *12*, 051503.
- (36) Galanzha, E. I.; Shashkov, E. V.; Tuchin, V. V.; Zharov, V. P. In vivo multispectral, multiparameter, photoacoustic lymph flow cytometry with natural cell focusing, label-free detection and multicolor nanoparticle probes. *Cytometry, Part A* **2008**, *73*, 884–94.
- (37) Nedosekin, D. A.; Sarimollaoglu, M.; Shashkov, E. V.; Galanzha, E. I.; Zharov, V. P. Ultra-fast photoacoustic flow cytometry with a 0.5 MHz pulse repetition rate nanosecond laser. *Optics Express* **2010**, *18*, 8605–20.
- (38) Kim, J.-W.; Shashkov, E. V.; Galanzha, E. I.; Kotagiri, N.; Zharov, V. P. Photothermal antimicrobial nanotherapy and nanodiagnosis with self-assembling carbon nanotube clusters. *Lasers Surg. Med.* **2007**, *39*, 622–34.
- (39) Zharov, V. P.; Mercer, K. E.; Galitovskaya, E. N.; Smeltzer, M. S. Photothermal nanotherapeutics and nanodiagnosis for selective killing of bacteria targeted with gold nanoparticles. *Biophys. J.* **2006**, *90*, 619–27.
- (40) Zharov, V. P.; Galanzha, E. I.; Shashkov, E. V.; Khlebtsov, N. G.; Tuchin, V. V. In vivo photoacoustic flow cytometry for monitoring of circulating single cancer cells and contrast agents. *Opt. Lett.* **2006**, *31*, 3623–25.
- (41) Galanzha, E. I. Blood and lymph circulating cells: well-known systems, well-forgotten interdependence. *J. Blood Lymph* **2011**, *1*, 1–2.
- (42) Galanzha, E. I.; Sarimollaoglu, M.; Nedosekin, D. A.; Keyrouz, S. G.; Mehta, J. L.; Zharov, V. P. In vivo flow cytometry of circulating clots using negative photothermal and photoacoustic contrasts. *Cytometry, Part A* **2011**, *79*, 814–24.
- (43) Galanzha, E. I.; Zharov, V. P. In vivo photoacoustic and photothermal cytometry for monitoring multiple blood rheology parameters. *Cytometry, Part A* **2011**, *79*, 746–57.
- (44) Shao, J.; Griffin, R. J.; Galanzha, E. I.; Kim, J.-W.; Koonce, N.; Webber, J.; Mustafa, T.; Biris, A.; Nedosekin, D. A.; Zharov, V. P. Photothermal nanodrugs: potential of TNF-fold nanospheres for cancer theranostics. *Sci. Rep.* **2013**, *10.038/srep 01293* (in press).
- (45) Zharov, V. P. Ultrasharp nonlinear photothermal and photoacoustic resonances and holes beyond the spectral limit. *Nat. Photonics* **2011**, *5*, 110–6.
- (46) Li, P. C.; Wei, C. W.; Liao, C. K.; Chen, C. D.; Pao, K. C.; Wang, C. R.; Wu, Y. N.; Shieh, D. B. Photoacoustic imaging of multiple targets using gold nanorods. *IEEE Trans Ultrason. Ferroelectr. Freq. Control* **2007**, *54*, 1642–7.
- (47) Choi, H. S.; Liu, W.; Misra, P.; Tanaka, E.; Zimmer, J. P.; Itty Ipe, B.; Bawendi, M. G.; Frangioni, J. V. Renal clearance of quantum dots. *Nat. Biotechnol.* **2007**, *25*, 1165–70.
- (48) Allard, J. E.; Risinger, J. I.; Morrison, C.; Young, G.; Rose, G. S.; Fowler, J.; Berchuck, A.; Maxwell, G. L. Overexpression of folate binding protein is associated with shortened progression-free survival in uterine adenocarcinomas. *Gynecol. Oncol.* **2007**, *107*, 52–7.
- (49) Clifton, G. T.; Sears, A. K.; Clive, K. S.; Holmes, J. P.; Mittendorf, E. A.; Ioannides, C. G.; Ponniah, S.; Peoples, G. E. Folate receptor alpha: a storied past and promising future in immunotherapy. *Hum. Vaccines* **2011**, *7*, 183–90.
- (50) Hartmann, L. C.; Keeney, G. L.; Lingle, W. L.; Christianson, T. J.; Varghese, B.; Hillman, D.; Oberg, A. L.; Low, P. S. Folate receptor overexpression is associated with poor outcome in breast cancer. *Int. J. Cancer* **2007**, *121*, 938–42.
- (51) Segal, E. I.; Low, P. S. Tumor detection using folate receptor-targeted imaging agents. *Cancer Metastasis Rev.* **2008**, *27*, 655–64.
- (52) He, W.; Kularatne, S. A.; Kalli, K. R.; Prendergast, F. G.; Amato, R. J.; Klee, G. G.; Hartmann, L. C.; Low, P. S. Quantitation of circulating tumor cells in blood samples from ovarian and prostate cancer patients using tumor-specific fluorescent ligands. *Int. J. Cancer* **2008**, *123*, 1968–73.
- (53) Basal, E.; Eghbali-Fatourechi, G. Z.; Kalli, K. R.; Hartmann, L. C.; Goodman, K. M.; Goode, E. L.; Kamen, B. A.; Low, P. S.; Knutson, K. L. Functional folate receptor alpha is elevated in the blood of ovarian cancer patients. *PLoS One* **2009**, *4*, e6292.
- (54) Kamen, B. A.; Caston, J. D. Direct radiochemical assay for serum folate: competition between 3H-folic acid and 5-methyltetrahydrofolic acid for a folate binder. *J. Lab. Clin. Med.* **1974**, *83*, 164–74.
- (55) Woodward, W. A.; Sulman, E. P. Cancer stem cells: markers or biomarkers? *Cancer Metastasis Rev.* **2008**, *27*, 459–70.
- (56) Yang, L.; Mao, H.; Cao, Z.; Wang, Y. A.; Peng, X.; Wang, X.; Sajja, H. K.; Wang, L.; Duan, H.; Ni, C.; Staley, C. A.; Wood, W. C.; Gao, X.; Nie, S. Molecular imaging of pancreatic cancer in an animal model using targeted multifunctional nanoparticles. *Gastroenterology* **2009**, *136*, 1514–25.e2.
- (57) Yang, L.; Peng, X. H.; Wang, Y. A.; Wang, X.; Cao, Z.; Ni, C.; Karna, P.; Zhang, X.; Wood, W. C.; Gao, X.; Nie, S.; Mao, H. Receptor-targeted nanoparticles for *in vivo* imaging of breast cancer. *Clin. Cancer Res.* **2009**, *15*, 4722–32.

- (58) Blasi, F.; Carmeliet, P. uPAR: a versatile signalling orchestrator. *Nat. Rev. Mol. Cell Biol.* **2002**, *3*, 932–43.
- (59) Eifler, R. L.; Lind, J.; Falkenhagen, D.; Weber, V.; Fischer, M. B.; Zeillinger, R. Enrichment of circulating tumor cells from a large blood volume using leukapheresis and elutriation: proof of concept. *Cytometry, Part B* **2011**, *80*, 100–11.
- (60) Spizzo, G.; Fong, D.; Wurm, M.; Ensinger, C.; Obrist, P.; Hofer, C.; Mazzoleni, G.; Gastl, G.; Went, P. EpCAM expression in primary tumour tissues and metastases: an immunohistochemical analysis. *J. Clin. Pathol.* **2011**, *64*, 415–20.
- (61) Went, P. T.; Lugli, A.; Meier, S.; Bundi, M.; Mirlacher, M.; Sauter, G.; Dirnhofer, S. Frequent EpCam protein expression in human carcinomas. *Hum. Pathol.* **2004**, *35*, 122–8.
- (62) Fehm, T.; Solomayer, E. F.; Meng, S.; Tucker, T.; Lane, N.; Wang, J.; Gebauer, G. Methods for isolating circulating epithelial cells and criteria for their classification as carcinoma cells. *Cytotherapy* **2005**, *7*, 171–85.
- (63) Wang, Z. P.; Eisenberger, M. A.; Carducci, M. A.; Partin, A. W.; Scher, H. I.; Ts'o, P. O. Identification and characterization of circulating prostate carcinoma cells. *Cancer* **2000**, *88*, 2787–95.
- (64) Allard, W. J.; Matera, J.; Miller, M. C.; Repollet, M.; Connelly, M. C.; Rao, C.; Tibbe, A. G.; Uhr, J. W.; Terstappen, L. W. Tumor cells circulate in the peripheral blood of all major carcinomas but not in healthy subjects or patients with nonmalignant diseases. *Clin. Cancer Res.* **2004**, *10*, 6897–904.
- (65) Mego, M.; Mani, S. A.; Cristofanilli, M. Molecular mechanisms of metastasis in breast cancer—clinical applications. *Nat. Rev. Clin. Oncol.* **2010**, *7*, 693–701.
- (66) Gorges, T. M.; Tinnofer, I.; Drosch, M.; Roese, L.; Zollner, T. M.; Krahn, T.; von Ahsen, O. Circulating tumour cells escape from EpCAM-based detection due to epithelial-to-mesenchymal transition. *BMC Cancer* **2012**, *12*, 178.
- (67) Butler, T. P.; Gullino, P. M. Quantitation of cell shedding into efferent blood of mammary adenocarcinoma. *Cancer Res.* **1975**, *35*, 512–6.
- (68) Liotta, L. A.; Kleinerman, J.; Saidel, G. M. Quantitative relationships of intravascular tumor cells, tumor vessels, and pulmonary metastases following tumor implantation. *Cancer Res.* **1974**, *34*, 997–1004.
- (69) Crisan, D.; Ruark, D. S.; Decker, D. A.; Drevon, A. M.; Dicarlo, R. G. Detection of circulating epithelial cells after surgery for benign breast disease. *Mol. Diagn.* **2000**, *5*, 33–8.
- (70) Powell, A. A.; Talasaz, A. H.; Zhang, H.; Coram, M. A.; Reddy, A.; Deng, G.; Telli, M. L.; Advani, R. H.; Carlson, R. W.; Mollick, J. A.; Sheth, S.; Kurian, A. W.; Ford, J. M.; Stockdale, F. E.; Quake, S. R.; Pease, R. F.; Mindrinos, M. N.; Bhanot, G.; Dairkee, S. H.; Davis, R. W.; Jeffrey, S. S. Single cell profiling of circulating tumor cells: transcriptional heterogeneity and diversity from breast cancer cell lines. *PLoS One* **2012**, *7*, e33788.
- (71) Meng, S.; Tripathy, D.; Frenkel, E. P.; Shete, S.; Naftalis, E. Z.; Huth, J. F.; Beitsch, P. D.; Leitch, M.; Hoover, S.; Euhus, D.; Haley, B.; Morrison, L.; Fleming, T. P.; Herlyn, D.; Terstappen, L. W.; Fehm, T.; Tucker, T. F.; Lane, N.; Wang, J.; Uhr, J. W. Circulating tumor cells in patients with breast cancer dormancy. *Clin. Cancer Res.* **2004**, *10*, 8152–62.
- (72) Tewes, M.; Aktas, B.; Welt, A.; Mueller, S.; Hauch, S.; Kimmig, R.; Kasimir-Bauer, S. Molecular profiling and predictive value of circulating tumor cells in patients with metastatic breast cancer: an option for monitoring response to breast cancer related therapies. *Breast Cancer Res Treat.* **2009**, *115*, 581–90.
- (73) Wulfing, P.; Borchard, J.; Buerger, H.; Heidl, S.; Zanker, K. S.; Kiesel, L.; Brandt, B. HER2-positive circulating tumor cells indicate poor clinical outcome in stage I to III breast cancer patients. *Clin. Cancer Res.* **2006**, *12*, 1715–20.
- (74) Kirby, B. J.; Jodari, M.; Loftus, M. S.; Gakhar, G.; Pratt, E. D.; Chanel-Vos, C.; Gleghorn, J. P.; Santana, S. M.; Liu, H.; Smith, J. P.; Navarro, V. N.; Tagawa, S. T.; Bander, N. H.; Nanus, D. M.; Giannakakou, P. Functional characterization of circulating tumor cells with a prostate-cancer-specific microfluidic device. *PLoS One* **2012**, *7*, e35976.
- (75) Iinuma, H.; Watanabe, T.; Mimori, K.; Adachi, M.; Hayashi, N.; Tamura, J.; Matsuda, K.; Fukushima, R.; Okinaga, K.; Sasako, M.; Mori, M. Clinical significance of circulating tumor cells, including cancer stem-like cells, in peripheral blood for recurrence and prognosis in patients with Dukes' stage B and C colorectal cancer. *J. Clin. Oncol.* **2011**, *29*, 1547–55.
- (76) Shimada, R.; Iinuma, H.; Akahane, T.; Horiuchi, A.; Watanabe, T. Prognostic significance of CTCs and CSCs of tumor drainage vein blood in Dukes' stage B and C colorectal cancer patients. *Oncol. Rep.* **2012**, *27*, 947–53.
- (77) de Cremoux, P.; Extra, J. M.; Denis, M. G.; Pierga, J. Y.; Bourstyn, E.; Nos, C.; Clough, K. B.; Boudou, E.; Martin, E. C.; Muller, A.; Pouillart, P.; Magdelenat, H. Detection of MUC1-expressing mammary carcinoma cells in the peripheral blood of breast cancer patients by real-time polymerase chain reaction. *Clin. Cancer Res.* **2000**, *6*, 3117–22.
- (78) Jaiswal, K. R.; Xin, H. W.; Anderson, A.; Wiegand, G.; Kim, B.; Miller, T.; Hari, D.; Ray, S.; Koizumi, T.; Rudloff, U.; Thorgerisson, S. S.; Avital, I. Comparative testing of various pancreatic cancer stem cells results in a novel class of pancreatic-cancer-initiating cells. *Stem Cell Res.* **2012**, *9*, 249–60.
- (79) O'Brien, C. A.; Pollett, A.; Gallinger, S.; Dick, J. E. A human colon cancer cell capable of initiating tumour growth in immunodeficient mice. *Nature* **2007**, *445*, 106–10.
- (80) Wright, M. H.; Calcagno, A. M.; Salcido, C. D.; Carlson, M. D.; Ambudkar, S. V.; Varticovski, L. Brca1 breast tumors contain distinct CD44+/CD24- and CD133+ cells with cancer stem cell characteristics. *Breast Cancer Res.* **2008**, *10*, R10.
- (81) Balasubramanian, P.; Lang, J. C.; Jatana, K. R.; Miller, B.; Ozer, E.; Old, M.; Schuller, D. E.; Agrawal, A.; Teknos, T. N.; Summers, T. A., Jr.; Lustberg, M. B.; Zborowski, M.; Chalmers, J. J. Multi-parameter Analysis, including EMT Markers, on Negatively Enriched Blood Samples from Patients with Squamous Cell Carcinoma of the Head and Neck. *PLoS One* **2012**, *7*, e42048.
- (82) Hou, J. M.; Krebs, M.; Ward, T.; Sloane, R.; Priest, L.; Hughes, A.; Clack, G.; Ranson, M.; Blackhall, F.; Dive, C. Circulating tumor cells as a window on metastasis biology in lung cancer. *Am. J. Pathol.* **2011**, *178*, 989–96.
- (83) Christiansen, J. J.; Rajasekaran, A. K. Reassessing epithelial to mesenchymal transition as a prerequisite for carcinoma invasion and metastasis. *Cancer Res.* **2006**, *66*, 8319–26.
- (84) Jiang, Y.; Jahagirdar, B. N.; Reinhardt, R. L.; Schwartz, R. E.; Keene, C. D.; Ortiz-Gonzalez, X. R.; Reyes, M.; Lenvik, T.; Lund, T.; Blackstad, M.; Du, J.; Aldrich, S.; Lisberg, A.; Low, W. C.; Largaespada, D. A.; Verfaillie, C. M. Pluripotency of mesenchymal stem cells derived from adult marrow. *Nature* **2002**, *418*, 41–9.
- (85) Reyes, M.; Dudek, A.; Jahagirdar, B.; Koodie, L.; Marker, P. H.; Verfaillie, C. M. Origin of endothelial progenitors in human postnatal bone marrow. *J. Clin. Invest.* **2002**, *109*, 337–46.
- (86) Kalka, C.; Masuda, H.; Takahashi, T.; Kalka-Moll, W. M.; Silver, M.; Kearney, M.; Li, T.; Isner, J. M.; Asahara, T. Transplantation of ex vivo expanded endothelial progenitor cells for therapeutic neovascularization. *Proc. Natl. Acad. Sci. U.S.A.* **2000**, *97*, 3422–7.
- (87) Lin, Y.; Weisdorf, D. J.; Solovey, A.; Hebbel, R. P. Origins of circulating endothelial cells and endothelial outgrowth from blood. *J. Clin. Invest.* **2000**, *105*, 71–7.
- (88) Takahashi, T.; Kalka, C.; Masuda, H.; Chen, D.; Silver, M.; Kearney, M.; Magner, M.; Isner, J. M.; Asahara, T. Ischemia- and cytokine-induced mobilization of bone marrow-derived endothelial progenitor cells for neovascularization. *Nat. Med.* **1999**, *5*, 434–8.
- (89) Mancuso, P.; Calleri, A.; Cassi, C.; Gobbi, A.; Capillo, M.; Pruneri, G.; Martinelli, G.; Bertolini, F. Circulating endothelial cells as a novel marker of angiogenesis. *Adv. Exp. Med. Biol.* **2003**, *522*, 83–97.
- (90) Rehman, J.; Li, J. L.; Orschell, C. M.; March, K. L. Peripheral blood “endothelial progenitor cells” are derived from monocyte/

- macrophages and secrete angiogenic growth factors. *Circulation* **2003**, *107*, 1164–9.
- (91) Jain, R. K.; Duda, D. G. Role of bone marrow-derived cells in tumor angiogenesis and treatment. *Cancer Cell* **2003**, *3*, 515–6.
- (92) Ruzinova, M. B.; Schoer, R. A.; Gerald, W.; Egan, J. E.; Pandolfi, P. P.; Rafii, S.; Manova, K.; Mittal, V.; Benezra, R. Effect of angiogenesis inhibition by Id loss and the contribution of bone-marrow-derived endothelial cells in spontaneous murine tumors. *Cancer Cell* **2003**, *4*, 277–89.
- (93) Schuch, G.; Heymach, J. V.; Nomi, M.; Machluf, M.; Force, J.; Atala, A.; Eder, J. P., Jr.; Folkman, J.; Soker, S. Endostatin inhibits the vascular endothelial growth factor-induced mobilization of endothelial progenitor cells. *Cancer Res.* **2003**, *63*, 8345–50.
- (94) Brower, V. Evidence of efficacy: researchers investigating markers for angiogenesis inhibitors. *J. Natl. Cancer Inst.* **2003**, *95*, 1425–7.
- (95) Nie, Z.; Petukhova, A.; Kumacheva, E. Properties and emerging applications of self-assembled structures made from inorganic nanoparticles. *Nat. Nanotechnol.* **2010**, *5*, 15–25.
- (96) Louie, A. Y. Multimodality Imaging Probes: Design and Challenges. *Chem. Rev.* **2010**, *110*, 3146–95.
- (97) Jin, Y.; Jia, C.; Huang, S. W.; O'Donnell, M.; Gao, X. Multifunctional nanoparticles as coupled contrast agents. *Nat. Commun.* **2010**, *1*, 41.
- (98) Kim, J.-W.; Deaton, R. Molecular self-assembly of multifunctional nanoparticle composites with arbitrary shapes and functions: challenges and strategies. *Part. Part. Syst. Charact.* **2013**, doi: 10.1002/ppsc.201200129 (in press).
- (99) Jones, M. R.; Osberg, K. D.; Macfarlane, R. J.; Langille, M. R.; Mirkin, C. A. Tempted Techniques for the Synthesis and Assembly of Plasmonic Nanostructures. *Chem. Rev.* **2011**, *111*, 3736–827.
- (100) Pinheiro, A. V.; Han, D.; Shih, W. M.; Yan, H. Challenges and opportunities for structural DNA nanotechnology. *Nat. Nanotechnol.* **2011**, *6*, 763–72.
- (101) Tan, S. J.; Campolongo, M. J.; Luo, D.; Cheng, W. Building plasmonic nanostructures with DNA. *Nat. Nanotechnol.* **2011**, *6*, 268–76.
- (102) Guo, P. X. The emerging field of RNA nanotechnology. *Nat. Nanotechnol.* **2010**, *5*, 833–42.
- (103) Shu, D.; Shu, Y.; Haque, F.; Abdelmawla, S.; Guo, P. X. Thermodynamically stable RNA three-way junction for constructing multifunctional nanoparticles for delivery of therapeutics. *Nat. Nanotechnol.* **2011**, *6*, 658–67.
- (104) Kim, J.-W.; Kim, J.-H.; Deaton, R. DNA-linked nanoparticle building blocks for programmable matter. *Angew. Chem., Int. Ed.* **2011**, *50*, 9185–90.
- (105) Kim, J.-W.; Kim, J.-H.; Deaton, R. Programmable construction of nanostructures: assembly of nanostructures with various nanocomponents. *IEEE Nanotechnol.* **2012**, *6* (1), 19–23.
- (106) Dubertret, B.; Calame, M.; Libchaber, A. J. Single-mismatch detection using gold-quenched fluorescent oligonucleotides. *Nat. Biotechnol.* **2001**, *19*, 365–70.
- (107) Pons, T.; Medintz, I. L.; Sapsford, K. E.; Higashiyama, S.; Grimes, A. F.; English, D. S.; Mattoussi, H. On the quenching of semiconductor quantum dot photoluminescence by proximal gold nanoparticles. *Nano Lett.* **2007**, *7*, 3157–64.
- (108) Champion, J. A.; Mitragotri, S. Role of target geometry in phagocytosis. *Proc. Natl. Acad. Sci. U.S.A.* **2006**, *103*, 4930–4.
- (109) Alexis, F.; Pridgen, E.; Molnar, L. K.; Farokhzad, O. C. Factors affecting the clearance and biodistribution of polymeric nanoparticles. *Mol. Pharmaceutics* **2008**, *5*, 505–15.
- (110) Otsuka, H.; Nagasaki, Y.; Kataoka, K. PEGylated nanoparticles for biological and pharmaceutical applications. *Adv. Drug Delivery Rev.* **2003**, *55*, 403–19.
- (111) Kotagiri, N.; Kim, J.-W. Carbon Nanotubes Fed on “Carbs”: Coating of Single-Walled Carbon Nanotubes by Dextran Sulfate. *Macromol. Biosci.* **2010**, *10*, 231–8.
- (112) Kotagiri, N.; Lee, J. S.; Kim, J.-W. Selective pathogen targeting and macrophage evading carbon nanotubes through dextran sulfate coating and PEGylation for photothermal theranostics. *J. Biomed. Nanotechnol.* **2013**, doi: 10.1166/jbn.2013.1531 (in press).
- (113) Andersen, E. S.; Dong, M.; Nielsen, M. M.; Jahn, K.; Subramani, R.; Mamdouh, W.; Golas, M. M.; Sander, B.; Stark, H.; Oliveira, C. L. P.; Pedersen, J. S.; Birkedal, V.; Besenbacher, F.; Gothelf, K. V.; Kjems, J. Self-assembly of a nanoscale DNA box with a controllable lid. *Nature* **2009**, *459*, 73–6.
- (114) Dings, R. P. M.; Williams, B. W.; Song, C. W.; Griffioen, A. W.; Mayo, K. H.; Griffin, R. J. Anginex synergizes with radiation therapy to inhibit tumor growth by radiosensitizing endothelial cells. *Int. J. Cancer* **2005**, *115*, 312–9.
- (115) Kim, J.-W.; Moon, H.-M.; Benamara, M.; Sakon, J.; Salamo, G. J.; Zharov, V. P. Aqueous-phase synthesis of monodisperse plasmonic gold nanocrystals using shortened single-walled carbon nanotubes. *Chem. Commun.* **2010**, *46*, 7142–4.
- (116) Tao, A.; Sinsermsuksakul, P.; Yang, P. Tunable plasmonic lattices of silver nanocrystals. *Nat. Nanotechnol.* **2007**, *2*, 435–40.
- (117) Yavuz, M. S.; Cheng, Y. Y.; Chen, J. Y.; Cobley, C. M.; Zhang, Q.; Rycenga, M.; Xie, J. W.; Kim, C.; Song, K. H.; Schwartz, A. G.; Wang, L. H. V.; Xia, Y. N. Gold nanocages covered by smart polymers for controlled release with near-infrared light. *Nat. Mater.* **2009**, *8*, 935–9.
- (118) Wang, X.; Fu, H. B.; Peng, A. D.; Zhai, T. Y.; Ma, Y.; Yuan, F. L.; Yao, J. N. One-Pot Solution Synthesis of Cubic Cobalt Nanoskeletons. *Adv. Mater.* **2009**, *21*, (16) doi: 10.1002/adma.200990051.
- (119) Seo, D.; Il Yoo, C.; Chung, I. S.; Park, S. M.; Ryu, S.; Song, H. Shape adjustment between multiply twinned and single-crystalline polyhedral gold nanocrystals: Decahedra, icosahedra, and truncated tetrahedra. *J. Phys. Chem. C* **2008**, *112*, 2469–75.
- (120) Liao, H. G.; Jiang, Y. X.; Zhou, Z. Y.; Chen, S. P.; Sun, S. G. Shape-Controlled Synthesis of Gold Nanoparticles in Deep Eutectic Solvents for Studies of Structure-Functionality Relationships in Electrocatalysis. *Angew. Chem., Int. Ed.* **2008**, *47*, 9100–3.
- (121) Sun, Y. G.; Mayers, B. T.; Xia, Y. N. Template-engaged replacement reaction: A one-step approach to the large-scale synthesis of metal nanostructures with hollow interiors. *Nano Lett.* **2002**, *2*, 481–5.
- (122) Ni, W. H.; Yang, Z.; Chen, H. J.; Li, L.; Wang, J. F. Coupling between molecular and plasmonic resonances in freestanding dye-gold nanorod hybrid nanostructures. *J. Am. Chem. Soc.* **2008**, *130*, 6692–3.
- (123) Pagan, J.; Przybyla, B.; Jamshidi-Parsian, A.; Gupta, K.; Griffin, R. J. Blood outgrowth endothelial cells increase tumor growth rates and modify tumor physiology: relevance for therapeutic targeting. *Cancers* **2013**, *5*, 205–17.

#### ■ NOTE ADDED AFTER ASAP PUBLICATION

This paper was published on the Web on February 25, 2013. Citations have been corrected in the first two paragraphs of the IN VIVO NANOTHERANOSTICS OF CIRCULATING DISEASE-ASSOCIATED CELLS AND BIOMOLECULES: RECENT ADVANCES section. The corrected version was reposted on March 4, 2013.